UNIVERSITY OF SOUTHAMPTON

FACULTY OF ENGINEERING, SCIENCE AND MATHEMATICS

SCHOOL OF ELECTRONICS AND COMPUTER SCIENCE

IMAGE SEGMENTATION BASED ON WATER FLOW ANALOGY

by

Xin Liu

Thesis for the degree of Doctor of Philosophy

May 2009

UNIVERSITY OF SOUTHAMPTON

ABSTRACT

FACULTY OF ENGINEERING, SCIENCE AND MATHEMATICS

SCHOOL OF ELECTRONICS AND COMPUTER SCIENCE

Doctor of Philosophy

IMAGE SEGMENTATION BASED ON WATER FLOW ANALOGY

by Xin Liu

Segmenting objects with complex shapes, like segmenting vessels in iridology and detecting roads in remote sensing, is of practical significance in image analysis. Region growing and snakes are the main methods used in the field, but the former cannot yield an exact result whilst the latter has difficulties with topological changes.

This thesis presents a new method, based on the paradigm of water flow. The mechanism embodies the fluidity of water and thus can deal with complicated objects. A snake-like force functional is utilized, including edge-based and region-based forces, guiding extraction to select the target feature. Water characteristics such as surface tension and adhesion are also implemented so that the smoothness of extracted contour and ability of flow to narrow branches are obtained.

Furthermore, force field theories are incorporated for an alternative definition of the water flow forces so that the water flow framework becomes more generalised and flexible and the underlying theoretical basis is more consistent. Because of the 3-D nature of the physical water flow process, the extension of the model to higher dimensions is straightforward and has been implemented in this research. The higher dimensionality, however, increases the computational cost. To improve the efficiency,

a water cooling system is proposed. This system identifies water elements that are inactive in previous flow iterations and removes them from the subsequent computations to reduce the total computational burden. The water cooling system provides an adjustable efficiency-controlling-facility and is also useful in 2-D applications.

The new technique has been assessed on both synthetic and natural images. The topological adaptability and the geometrical flexibility of the model are assessed. In addition, the approach is shown to be able to segment shapes with weak contrast to their background. The good ability to handle noise, consistent with properties included in its formulation, has been justified both qualitatively and quantitatively. The effectiveness of the water cooling system is also proved graphically and quantitatively. Further, the method is applied to medical imaging problems such as MRI image segmentation, vessel detection and medical volume segmentation. The results justify the great potential of the new technique in the real-world applications.

Table of Contents

List of Figures

Declaration of Authorship

I, Xin Liu, declare that the thesis entitled Image Segmentation Based on Water Flow Analogy and the work presented in it are my own, I confirm that:

- this work was done wholly or mainly while in candidature for a research degree at this University;
- where any part of this thesis has previously been submitted for a degree or any other qualification at this University or any other institution, this has been clearly stated;
- where I have consulted the published work of others, this is always clearly attributed;
- where I have quoted from the work of others, the source is always given. With the exception of such quotations, this thesis is entirely my own work;
- I have acknowledged all main sources of help;
- where the thesis is based on work done by myself jointly with others, I have made clear exactly what was done by others and what I have contributed myself;
- parts of this work have been published as listed in Section 1.5 of the thesis.

Signed: ……..

Date:…….

Acknowledgement

I would like to thank my research advisor, Prof. Mark S. Nixon, for his friendship, encouragement, and guidance during the course of my PhD research. He has been a very valuable source of ideas and stimulating discussions/comments both on technical and on non-technical topics. It has been my great fortune and honor to earn my degree under his supervision.

I would like to thank all of my colleagues and friends whose friendship and encouragement have made my experience at the University of Southampton memorable and valuable. In particular, I would like to thank Imed Bouchrika for his patience and help on various programming issues.

Finally I would like to thank my parents Pei Liu and Dongxia Zhao for all that they have done for me. This dissertation is dedicated to them.

Chapter 1

Introduction

1.1 Motivation

Automatic image segmentation is a fundamental task of early computer vision and it has been studied extensively. It aims to isolate one or more objects from the other objects or background, and hence provide useful information for higher level image processing tasks.

Segmenting objects from images is a difficult task because of the variability of object shapes and topologies and the limitation of the quality of source images. For example, one useful application of image segmentation in medical imaging is the detection of vessels in digital fundus photos. Figure 1.1 shows a typical example, where we can see that the image quality is limited and more importantly, the vessels have quite complex shapes and topologies. Here a satisfactory image segmentation technique thus should be geometrically flexible and topologically adaptable. The image quality issues including weak contrast and noise may cause over- or under-segmentation, edge leakage and discontinuity, and contour smoothness problems. Properties such as

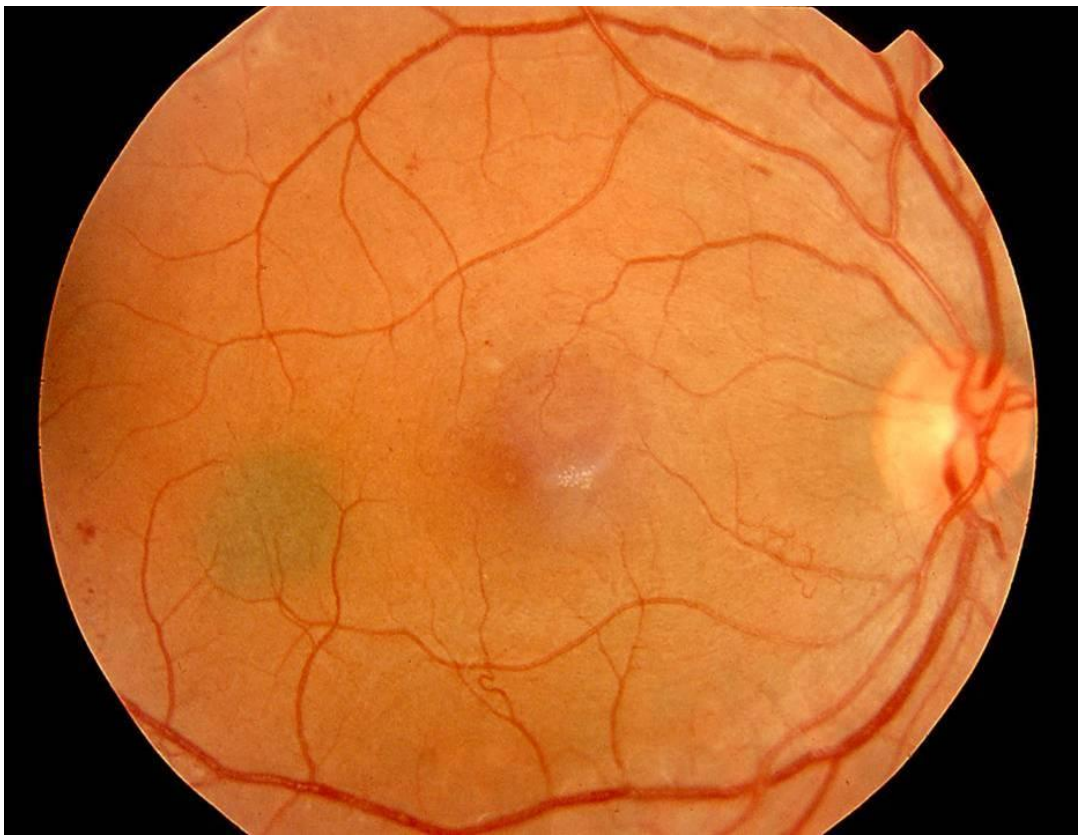

Figure 1.1: Example digital fundus photo

continuous contours, smoothness control, and noise robustness hence are also highly desirable. In addition, for many applications, high-level knowledge about images from users or experts may give very useful guidance and/or improvement to the detection results. For example, we may know the topology of the object of interest in advance and hence want to impose a constraint on the topology on the result. Thus a framework that is able to embed such high-level control facilities is potentially applicable to a wider range of applications.

Many image segmentation techniques have been developed, aiming to overcome the problems discussed above. One of the successful and popular techniques is the family of active contour based methods / snakes. Essentially, the techniques deform contours towards features of interest like boundaries based on the minimisation of an energy functional. As the functional is defined by image features and constraints on

the contours, solving the minimisation problem leads to two forces: the internal force regulating the deforming contour and the external force guiding the deformation. One drawback of the techniques is the use of numerical algorithms such as the steepest descent methods used to solve the energy minimisation problem. Another example is the level set method commonly used by geometric active contour models to represent the contours and thus handle the topological changes. Those numerical methods lead to high computational cost and increased degree of complexity. The former issue can be resolved by introducing more efficient numerical methods or sophisticated efficiency improvement procedures. However, this often makes the system even more complex, which may lead to difficulties in understanding the algorithms, choosing the most appropriate input parameters and interpreting the outputs. This is another common challenge faced by image segmentation, to understand the techniques themselves. One solution to this problem is the use of physical analogy. By mimicking physical processes/forces, we can avoid basing the technique solely on complex and abstract mathematical concepts. Now the inputs and outputs of the model can be mapped to the corresponding physical phenomenon or forces, and thus are more natural and intuitive to understand and interpret.

In this work, we aim to develop an image segmentation technique that can overcome most of the problems discussed above. The method is based on analogy to water flow process to achieve smoothness control, geometrical flexibility and topological adaptability. Numerical methods like finite element analysis that are often used in water flow modelling in computer graphics are avoided here to retain a low level of complexity and relatively high computational efficiency. In addition, the framework of the technique is quite flexible. For instance, topology control can be easily added to the water flow model. The model has used snake-like image force terms to guide the flow towards the image boundaries. Therefore, it can be naturally integrated with other application-dependent snake forces and absorb the strengths of the application-specific techniques. This gives the method strong potential in a wider range of practical applications.

1.2 Related work

There have been a lot of image segmentation techniques proposed. Edge detection and linking, region growing and merging, relaxation labelling, statistical approaches, mathematical morphology based algorithms, and active contours are among the most widely used techniques. In this section, a brief overview of their general principles, advantages and limitations is provided.

Edge detection and linking is a two step approach. First, an edge detector that detects intensity discontinuities is applied to an image to identify edge elements. Image smoothing techniques like Gaussian filter are often applied in this step to eliminate noises. Then, an edge linking algorithm is used to link the edge elements together to obtain a parameterized curve representation. Further information about the common edge detection and linking techniques can be found in most computer vision and image processing textbooks (e.g. [1, 2]). A common problem for edge detection and linking techniques is that they cannot guarantee closed and smooth boundaries. In addition, those methods only consider local information so that incorrect assumptions may be made during the boundary integration process which may cause generation of infeasible object boundaries.

Region growing and merging techniques [3]-[7] rely on the assumption that adjacent pixels in the same region have similar intensity, texture or colour. Region merging techniques test the statistics inside adjacent regions to decide whether they can be merged or not, according to specified metrics. Region growing can be considered to be a special case of merging where there is only one evolving region and the adjacent regions are individual points. The techniques are free of the topological changes since they are pixel-wise methods without smoothness constraints, and the performance depends mainly on the selected homogeneity criterion. Relaxation labelling [8, 9] segments images using a class of locally cooperative and parallel processes based on the intensity difference among neighbouring pixels. It starts by

calculating the probabilities of pixels to be associated with a given label. Compatibility coefficients which encourages neighbouring pixels to have same label are then weighted to the probabilities. For a particular pixel and a given label, the weighted average of the probabilities of its local neighbouring pixels is added to its own probability. Consequently, a pixel identified as having a high probability to be associated with a given label will increase the probability that its neighbour's pixels are associated with the same label. This process is iterated for all the labels and all the pixels until the probabilities converge. The technique aims to assign each object in the image one label. There are some common limitations for the above two segmentation techniques. The lack of smoothness constraints of the detected boundaries can lead to irregular boundaries and small holes, especially when dealing with real or noisy images. The techniques are normally based on region statistics, which cannot provide so accurate boundary detection results as edge-based techniques.

Statistical approaches for image segmentation include feature space clustering methods. A feature space is a mapping of the input obtained through the processing of the data in small subsets. For each subset, a parametric representation of the considered feature such as intensity or colour is calculated and the result is mapped into a point in the multi-dimensional parameter space. Applying the process to the entire input data, the significant features will correspond to denser regions in the feature space (i.e. clusters). The objective is then to delineate the clusters. One example of the clustering methods is the k−means algorithm [10]. It seeks k points in feature space that explain the data as the means of disjoint populations. These points are then used to label pixels in the image domain by their means in the feature space. Some other feature space clustering methods consider the feature space as the empirical probability density function (pdf) of the represented parameters. Here dense regions correspond to local maxima of the pdf, i.e., to the modes of the pdf. The next step is then modes detection using some mode seeking algorithms, one such technique is the mean-shift algorithm [11]. For a given distribution in feature space,

the local maxima of a density are located through repeated restarting and hill climbing. These detected modes are then used to assign labels to pixels in the image domain. The clustering methods have a main short-coming: there is no constraint that guarantees contiguous segments because the feature spaces may not preserve the geometry of the image plane.

Mathematical morphology methods like open and close operators and morphological edge detectors [2, 12] have also been used to segment images, and the prime tool of mathematical morphology-based image segmentation is the watershed transform. The theorem has a very long history [13]. It is based on the fact that smooth surfaces can be decomposed into hills and valleys by studying critical points and surface gradient. Considering pixel properties, like intensity or gradient, as elevation and then simulating rainfall on the landscape, rain water will flow from the areas of high altitude along lines of steepest descent to arrive at some regional minimal height. The watersheds or catchment basins are defined as the drainage areas of its regional minima and their boundaries (some authors have named it "water partings") can then be used for object extraction. An alternative physical analogy often used is "immersion" [14]. The image is still considered as a topographic surface and holes are supposed to be pierced in each regional minimum. Then the surface is immersed into a lake. Beginning from the lowest evaluation (minima), the water is assumed to progressively fill up all the catchment basins. At each pixel where the water coming from different minima would merge, a "dam" is built. The set of dams at the end of immersion is then defined as water partings. It is worth noting that though assuming water collection or immersion, watershed methods do not use the properties of the water itself and concentrate on the "geographical" characteristics of the images. One drawback of the watershed method is the high complexity and computational cost arising from the non-linearity due to tasks like finding lines of steepest descent between two points. Some efficient methods [15]–[19] have been proposed to provide a much quicker computation. However, the application of the fast watershed methods to images may give disappointing results because of the over-segmentation

problem. The image can be segmented into a number of "tiny, shallow watersheds" [14] and other techniques like region merging are often needed to improve the result. Similar to region growing, the detected boundaries using watershed approaches also suffers the smoothness problem.

Since Kass et al. [20] proposed the parametric snake, active contour based methods have received much attention on image segmentation. The technique deforms initial contour(s) towards the boundary of the object to be detected. The deformation is formulated by minimising an energy functional whose (local) minimum is achieved when contours are smooth and reside on object boundaries. The energy functional is generally expressed as

$$E = E_{int} + E_{ext} \tag{1.1}$$

where E_{int} is the internal deformation energy of the contour that prescribes *a priori* knowledge of the deforming contour such as its shape properties (elasticity and rigidity), and E_{ext} is the external image energy that depends on the image features like intensity/colour along the contour. The minimisation of this energy functional can be achieved by constructing a dynamic system that is governed by the energy functional and then evolving the system to equilibrium using numerical algorithms like steepest descent method.

The combination of the internal and external energy terms makes the active contour model capable of locating the object boundaries whilst retaining smoothness of the segmentation. It can also be extended by adding constraint related energy terms so that user-interaction can be obtained. Based on the same principle of deforming contours by minimising an energy functional, there have been many active contour based methods developed to overcome various problems in image segmentation areas. The technique is considered most relevant to the proposed water flow based approach and has been used in results assessments/comparisons. Thus a more detailed review is considered necessary and is given in Chapter 2.

1.3 Thesis contributions

This thesis proposes a new image segmentation technique. Compared to watershed based methods, the new approach is also based on analogy to water or fluid flow but the focus is on the "water" itself rather than the "landscape" of images. It is because the properties of water, like fluidity and surface tension, are well suited to complex image feature extraction. The proposed technique is a physical analogy approach, so its principles, parameters and outputs are relatively explicit to interpret, which is a fundamental advantage of physical models as discussed in section 1.1. This also makes the model easier to be combined with other image segmentation techniques and thus absorb their advantages.

The new model first imitates the physical water flow process in the 2D image domain. To achieve this, image pixels are separated as water or non-water elements and interactive forces between them are assumed to exist. The image "landscape" is used to generate image forces which stop the flow at feature contours. A snake-like force functional is utilized, including edge-based and region-based forces. After defining the flow resistance according to edge strength, the flow velocity is determined. Then we can apply those parameters to dynamical formulae so as to determine the flow movement. In this thesis, an operator based on energy conversion / transformation is used for simplicity.

In the analogy, only main water properties including fluidity, surface tension and adhesion are modelled to reduce the imitation complexity, because those main attributes should be sufficient for image segmentation purposes. The fluidity equips the model with geometrical flexibility and topological adaptability. Aided by the surface tension and adhesion, the analogical water can retain relatively smooth contours and is able to flow into narrow branches.

One of the key questions in designing the physical analogy model is how to define

the attractive or repulsive forces between pixels, so the force field analogy [21] is considered to be naturally linked with this new method. The water pressure, surface tension and adhesion can be defined in such a way that each pixel is thought to generate a spherical Gaussian force field, and then all the forces are calculated jointly through a convolution with one single template. The force field based definitions make the water flow model more flexible and understandable and the underlying physical basis more consistent. Furthermore, the extension of the convolution mask size, which gives more information to determine the forces, is easy to implement.

Besides 2D analogy, the 3D version water flow model is also presented. Because all the physical concepts behind this analogical technique are originally defined in 3D space in physics, the extension of the water flow model to higher dimension is straightforward and natural which can be considered as another advantage of physical analogy models.

The experimental results both for synthetic and for natural images indicate the water flow technique can overcome problems like boundary concavities, geometrical and topological changes. The new method also appears to have good noise robustness, especially to impulsive noise, which is difficult for other popular segmentation algorithms based on contour evolution. Besides, by selecting different parameters, the technique can focus on structure and detail, respectively. In total, the new method is shown to have great potential in many practical image segmentation applications where the objects of interest are geometrically and/or topologically complex and the images are often noisy and of low quality (e.g. medical image processing).

1.4 Thesis overview

The thesis is divided into seven chapters. The remaining chapters are arranged as follows.

- Chapter 2: ***Active contour based methods***

The new technique can be viewed as a model based on contour evolutions. Further, snake-like image force terms have been used to guide the flow process. Therefore, the active contour based methods are considered the most relevant techniques and are reviewed in more detail. This chapter starts with the review of the parametric active contour method, and then introduces the geometric active contours. At the end, various image force terms which are designed for different problems / applications are presented and discussed.

- Chapter 3: ***Water flow analogy***

In this chapter, the proposed approach for segmenting objects from images by analogy to water flow is described. The method uses a simplified physical analogy structure where the whole water flow process is separated into two distinct phases. In the first phase, the initial flow rate/velocity of a water element is derived by considering the forces from other water elements (water pressure) and adjacent edge elements (adhesion). This leads to the initial kinetic energy of the water element. The next phase then examines whether or not the kinetic energy is sufficient to overcome the image resistant forces and hence the water element can flow to the position targeted. The whole framework of the technique is first presented, followed by the detailed definition of the terms and parameters in the model.

- Chapter 4: ***Refining the water flow model: force field, 3D & efficiency***

This chapter is devoted to the procedures and extensions used to refine the basic water flow model. Related works based on physical force field analogy are first reviewed. The water flow forces are then re-defined with respect to the force field theories so that the modified water flow model becomes more flexible and the underlying theoretical basis is more consistent. In addition, we show that the force field based water flow model is equivalent to the original model with an additional force field smoothing process and thus should exhibit better noise

robustness. The extension to a 3D water flow model is then presented. Lastly, the computational efficiency problem is considered and a water freezing system that "freezes" inactive water elements is introduced to address this issue.

- Chapter 5: ***Complex shape segmentation***

In this chapter, the experimental results of the proposed technique for segmenting complex shapes are presented and discussed. Both qualitative and quantitative performance evaluation are conducted on synthetic and natural images. The water flow based technique is shown to be geometrically flexible and topologically adaptive. We also show that by adopting an explicit constraint on the flowing contour, the model can retain its original topology. The immunity to noise of the model is then assessed, where both edge-based (gradient vector flow) [22] and region-based [23] active contour models have been used for comparison. The better immunity to noise of the force field based water flow to the original convolution based water flow model is also verified. At the end of this chapter, the efficiency improvement and the higher dimension extension are discussed.

- Chapter 6: ***Medical image and volume segmentation***

This chapter is devoted to the discussion of the experimental results of applying the water flow model to medical 2D and 3D images. The results of MR image segmentation is first evaluated qualitatively. This is followed by a quantitative assessment of the water flow technique on vessel segmentation in retinal images. At last, the medical volume image segmentation results are presented.

- Chapter 7: ***Conclusions and future work***

A summary of the thesis is outlined in this chapter, followed by a list of main contributions. At the end, future work and research thrusts are also discussed.

1.5 List of publications

So far, the following papers have published.

[A] X. U. Liu and M. S. Nixon, "Water flow based complex feature extraction," *Advanced Concept for Intelligence Vision Systems 2006 (Acivs'06)*, Lecture Notes in Computer Science, Volume 4179, Page 833–845, September 2006.

[B] X. U. Liu and M. S. Nixon, "Water flow based vessel detection in retinal images," *International Conference on Visual Information Engineering (VIE'06)*, Page 345–350, September 2006.

[C] X. U. Liu and M. S. Nixon, "Medical image segmentation by water flow," in *Proceedings of Medical Image Understanding and Analysis (MIUA'07)*, Page 161–165, July 2007.

[D] X. U. Liu and M. S. Nixon, "Image and volume segmentation by water flow," *International Symposium on Visual Computing (ISVC'07)*, Lecture Notes in Computer Science, Volume 4842, Page 62–74, November 2007

Chapter 2

Active Contour Based Methods

Active contour based methods (also known as deformable models or snakes) have received much attention in image segmentation areas because of some of its desirable characteristics. The technique can guarantee continuous contours and control the smoothness and geometry of the results. High-level knowledge and user-interactions can be easily integrated as well. Further, the methods are flexible to combine with other image processing techniques, leading to broad application in computer vision.

The proposed water flow model has quite similar properties to active contours such as the smoothness control and contour evolution. In particular, the image forces guiding the water flow process (see section 3.6) are derived in a similar way to those used in active contour based methods. Furthermore, two well-known active contour based methods have been chosen to compare with the proposed new technique. Therefore, a detailed review of some of the classic/popular active contour models is considered very necessary.

Active contours can be classified as parametric active contours and geometric active

contours (GAC) according to their contour representation. The parametric snakes represent deforming contours as parameterised curves, whereas in GAC models the deforming contours are intrinsic (non-parametric). This chapter will thus start with introducing the two active contour families.

2.1 Parametric active contours

We first introduce the classical active contour method/snake first presented by Kass et al in [20], where the deforming contours are represented explicitly as parameterised curves in a Lagrangian formulation.

Define a given image plane $I : \Omega \subset \mathbb{R}^2 \rightarrow \mathbb{R}^+$ in which we want to detect the objects boundaries, and a parameterised curve $\mathcal{C}$: $\{c(q) : [a, b] \rightarrow \Omega\}$, q being an arbitrary parameterisation factor. A closed curve can be specified by the periodic boundary condition $c(0) = c(1)$. The model associates the curve $\mathcal{C}$ with an energy functional given by [1, 20]:

$$E(\mathcal{C}) = \underbrace{\int_a^b (\alpha \mid c'(q) \mid^2 + \beta \mid c''(q) \mid^2) dq}_{E_{int}} + \lambda \underbrace{\int_a^b g^2(\mid \nabla I(c(q)) \mid) dq}_{E_{ext}} \qquad (2.1)$$

In equation (2.1), α and β control the elasticity and rigidity of the curve $\mathcal{C}$, and λ determines the contribution of the external energy E_{ext} which is based on a monotonic decreasing function $g(x)$ with $g(0) = 1$ and $\lim_{x \rightarrow +\infty} g(x) = 0$. A common choice of $g(x)$ is $g(x) = 1 / (1 + x^2)$. In summary, the internal energy E_{int} controls the smoothness behaviour of the curve, whereas the external one E_{ext} helps attract the curve toward the boundaries of the object of interest.

As Ω is bounded, the energy $E(\mathcal{C})$ admits at least a global minimum. Based on the calculus of variations, the curve $\mathcal{C}$ that minimises $E(\mathcal{C})$ must satisfy the associated Euler-Lagrange equation:

$$\alpha c''(q) - \beta c''''(q) - \lambda \nabla (g^2(\mid \nabla I(c(q)) \mid)) = 0 \qquad (2.2)$$

The first two terms in the RHS of equation (2.3) can be regarded as the internal force

F_{int} controlling the stretching and bending of the curve. The third term is deemed as the external force F_{ext} pulling the curve towards the image edges.

Gradient descent methods are often adopted to solve equation (2.2). The problem is embedded to a dynamical scheme by treating $c(q)$ as a function of time t as well as q -- i.e., $c(q,t)$. We define the initial curve as $c(q,0) = \mathcal{C}_0(q)$. The partial derivative of c with respect to t is then set to equal the sum of internal force F_{int} and external force F_{ext}, leading to the equation below:

$$c_t = \alpha c''(q,t) - \beta c''''(q,t) - \lambda \nabla(g^2(|\nabla I(c(q))|)) \qquad (2.3)$$

When $c(q,t)$ stabilises, the partial derivative c_t vanishes and a solution of equation (2.6) is achieved. The implementation of the model generally needs to approximate the curve as a set of nodes connected in series (often denoted as snaxels). Numerical methods such as finite difference methods are then adopted to approximate the derivatives and solve equation (2.3) iteratively.

Note that because the energy functional E is non-convex, the Euler-Lagrange equation (2.2) has many solutions corresponding to the local minima of E rather than the global minimum [24]-[26]. Because the gradient descent algorithm is a local minimisation technique, a good initialisation is generally required to achieve satisfactory solutions [20]. To overcome the problem, some researchers proposed to use a global optimisation techniques like genetic computations [27, 28]. However, global optimisation techniques generally lead to much more intense computational cost compared to the local minimisation methods like the gradient descent algorithm. Therefore, many methods aiming to enlarge the capture range of the external force F_{ext} have been proposed to improve the detection results, like the balloon model [25, 26] and the gradient vector flow [22, 29, 30]. Those techniques, together with other active contour models based on different external forces, are discussed in detail in section 2.3.

In addition to the sensitivity to initialisation conditions, the classical parametric active contour is also subject to the problems related to geometrical and topological changes. The regularity constraints defined in the internal energy in conjunction with the fixed parameterisation of the snake can limit the model's geometrical flexibility (e.g., preventing the contours from conforming to shapes with significant branches and protrusions or long tubular shapes), as well its topological adaptability (merging and splitting) [31]. One solution to those problems is the T-snake model (topologically adaptive snake) [31, 32].

In T-snake framework, the image plane is decomposed into a grid of discrete cells defined using affine cell decomposition (ACD), which subdivides the plane into a set of disjoint connected triangle subsets. The T-snake is then defined in terms of the edges of the ACD grid cells (i.e., the intersecting points of the contour with the ACD grid). The contour is then deformed in the same way as a classical snake. At the end of a deformation step, the snake nodes may have moved relative to the grid edges and a new set of intersection points is detected. Based on some decision rules such as only one snake node on one grid edge line, the new intersection points can form the new set of snake nodes. Then the disconnecting and reconnecting process is applied to those nodes to join them together to approximate a new active contour. This is effectively a re-parameterisation process of the snake model. Figure 2.1a and b taken from [20] give an graphical example of this process. When disconnecting and reconnecting the snake nodes, consistent decisions have been made so that one triangle grid can only contain one line segment joined by two snake nodes and the line segment also must intersect the triangle grid on two distinct edges. Those rules help the T-snake automatically handle topological changes. For example, when two or more snakes collide, there will be some triangle grids containing two or more line segments. Based on the decision rules described above, two line segment end-points on different edges of those triangles will then be chosen so that they are the closest points to the triangle vertices that are outside the active contour when expanding (and inside when shrinking) and the line segment joining them separates the inside and the

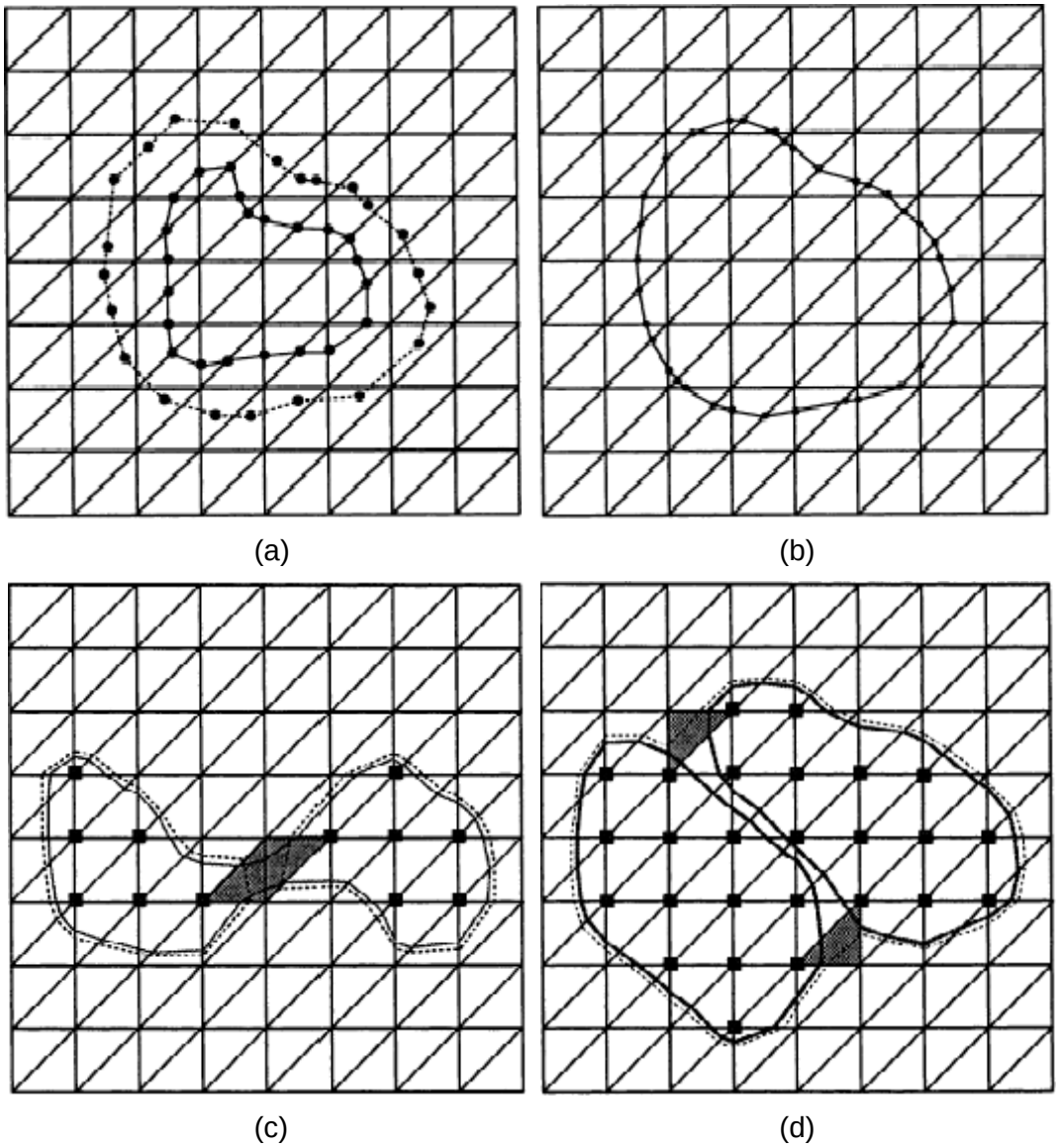

Figure 2.1: Examples of the T-snake deformation process. (a)-(b) the snake nodes moves relative to the triangle grids and new intersection points are defined and joined to form the new contour and nodes. (c) the snake is shrinking and splitting, at the splitting grids (shadowed triangles), there are four intersection points and two line segments. Based on the decision rules, the original two line segments are disconnected and the two points closest to the inside vertex (the black vertices) are chosen and connected to form the new contours (the dash lines). (d) two contours is merging with each other.

outside grid vertices. Figure 3.1c and 3.1d [20] give two examples showing how this re-parameterisation/re-sampling process performed on the triangle grids can lead to automatic topological transformations.

T-snake is an improved model to classic parametric active contour models as it can

handle topological changes. However, because of the iterative re-sampling process, it is also more computationally intense. Further, it is does not overcome the other drawbacks of the parametric explicit active contour models. The energy functional is also given by equation (2.1) and thus is still dependent on the parameterisation of the curve. As outlined above, the curves are still deformed using equation (2.3), where the 4th derivative term might bring numerical instabilities. This can be solved by setting β=0, which will lead to the loss of rigidity control [1].

Active contour models based on implicit contours are just designed to solve those problems. First presented by Caselles et al. in [33] and Malladi et al. in [34], the geometric active contour model is generally considered as a significant improvement to parametric snake models and has become more and more popular in recent years.

2.2 Geometric active contours

The geometric active contour can be considered as being derived from the parametric one as shown by Figure 2.2. In this chapter, we will present a brief review of the structure and principles of geodesic active contours (GAC).

The geodesic active contour essentially imposes a geometric flow to the curve whose deformation is controlled by the partial differential equation (2.3). The derivation starts from setting the rigidity parameter β=0 so that possible numerical instabilities problems can be avoided and second-order discontinuities of the contour like corners

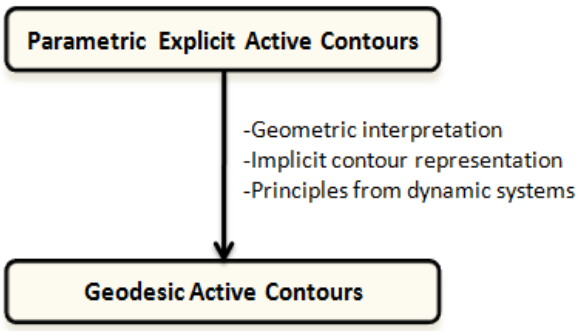

Figure 2.2: From parametric snakes to geodesic active contours [35]

are now allowed [36, 37]. The energy functional given by equation (2.1) is now written as

$$E(\mathcal{C}) = \int_a^b \alpha \,|\, c'(q) \,|^2 \, dq + \lambda \int_a^b g^2(|\, \nabla I(c(q)) \,|) dq \qquad (2.4)$$

This equation remains non-intrinsic as it is still dependent on the parameterisation of the curve $\mathcal{C}$, which leads to undesirable properties. For example, by changing the parameterisation of the curve, the energies can change in an arbitrary form [37].

A geometric interpretation of the energy function is thus desirable. Let's first define $J(\mathcal{C}) := -\lambda g^2(|\nabla I(c(q)|)$ and $m=\alpha/2$, then equation (2.4) can be rewritten as $E(\mathcal{C}) = \int_a^b L(c(q))\, dq$ where L is the Lagrangian defined as $L(\mathcal{C}) := \frac{m}{2}|c'(q)|^2 - J(\mathcal{C})$. The Hamiltonian is then given by $H = \frac{p^2}{2m} + J(\mathcal{C})$ where $p := mc'(q)$. Minimising the energy function $E(\mathcal{C})$ given by equation (2.4) constraining the Hamiltonian to zero energy level is then proved to be equivalent to minimising the new energy functional $E_G(\mathcal{C})$ given by equation below (see [36, 37]).

$$E_G(\mathcal{C}) = 2\sqrt{\lambda} \int_a^b g(|\, \nabla I(c(q)) \,|) \,|\, c'(q) \,|\, dq \qquad (2.5)$$

As $2\sqrt{\lambda}$ is a constant, the minimisation of $E_G(\mathcal{C})$ will not lose generality by setting it to 1. Further, setting $a=0$ and $b=1$ as in [36,37], we can defined a closed curve $\mathcal{C}$: $\{c(q) : [0, 1] \rightarrow \Omega, c(0)= c(1)\}$, and thus now $E_G(\mathcal{C})$ can be written as

$$E_G(\mathcal{C}) = \int_0^1 g(|\, \nabla I(c(q)) \,|) \,|\, c'(q) \,|\, dq \qquad (2.6)$$

A geometric interpretation of the energy function given by (2.6) can now be obtained by considering $E_G(\mathcal{C})$ as a new length definition, as $E_G(\mathcal{C})$ can be explained as adding a weight g to the Euclidean length $\mathcal{L}(\mathcal{C}) = \int_0^1 |c'(q)| dq$. It is equivalent to measuring the length of a path in a Riemannian space with respect to metric g. Define $ds=|c'(q)|dq$, the Euclidean arc length, and substitute it to equation (2.6), we have

$$E_G(\mathcal{C}) = \int_0^{\mathcal{L}(\mathcal{C})} g(|\, \nabla I(c(q)) \,|) ds \qquad (2.7)$$

Therefore, the minimisation of the energy functional $E_G(\mathcal{C})$ is equivalent to the

problem of determining the path of minimal length between two points in a Riemannian space [38]. The global minimum can also be found by solving the Euler-Lagrange equation using a steepest descent method. For an initial curve $c(s, t=0)= \mathcal{C}_0$, the deformation is governed by

$$c_t(s,t) = g\left(\left|\nabla I\left(c(s)\right)\right|\right)\kappa\mathcal{N} - \left(\nabla g\left(\left|\nabla I\left(c(s)\right)\right|\right)\cdot\mathcal{N}\right)\mathcal{N} \tag{2.8}$$

where $\mathcal{N}$ is the unit inward normal vector to the curve $\mathcal{C}$, and κ is the Euclidean curvature defined by

$$\kappa = \frac{x_{ss}y_s - y_{ss}x_s}{(x_s^2+y_s^2)^{\frac{3}{2}}} \tag{2.9}$$

The first term in equation (2.8), often named as curvature flow, is the contour regularisation term controlling the smoothness as well as driving the contour towards the boundary. It becomes zero when $g\left(\left|\nabla I\left(c(s)\right)\right|\right) = 0$, i.e., the curvature flow will stop at the object boundary. The second term in (2.8) can be regarded as a refinement force [39] which pulls back the contour if it passes the object boundary and thus prevent the boundary leaking problems.

So far an intrinsic formulation has been derived for the contour deformation / energy minimisation problem. However, this formulation itself does not solve the discrete implementation problems that occurs when a Lagrangian method is used in particular when topological changes present. Furthermore, such implementation may result in numerical instabilities at discontinuities [40,41]. To solve those problems, a new numerical method, the level set method, has been proposed. It can handle topological changes through a novel Eulerian framework. The central idea behind the method is to define the deforming curve as the zero-level (or other constant level) of a smooth (or at least Lipschitz continuous) function in a higher dimension. In this way, the topology of the implicitly represented curve can change even if the topology of the level set itself does not change, and hence the topological adaptability is achieved.

Assume $\phi(x, y, t) : \mathbb{R}^2 \rightarrow \mathbb{R}$ is an implicit representation of the curve $c(s,t)$, then we should have $c(s,t) = \{(x,y): \phi(x,y,t) = u\}$ where u is a constant often set to 0. It

is proved that if the planar curve $\mathcal{C}$ deforms according to $c_t = \beta \boldsymbol{N}$ for a given function β, then the embedding function ϕ should deform according to $\phi_t = \beta|\nabla\phi|$ where β is now computed on the level sets [37, 42]. Equation (2.8) can be written as the $c_t = \beta \boldsymbol{N}$ form

$$c_t = \left(g(|\nabla I|)\,\kappa - (\nabla g(|\nabla I|)\cdot \boldsymbol{N})\right)\boldsymbol{N} \tag{2.9}$$

Note that for simplicity, the geometric parameter s and time parameter t are skipped in equation (2.9). Now we can obtain a Hamilton-Jacobi type of equation for the geodesic active contour model:

$$\phi_t = \left(g(|\nabla I|)\kappa - \left(\nabla g(|\nabla I|)\cdot \frac{\nabla\phi}{|\nabla\phi|}\right)\right)|\nabla\phi| \tag{2.10}$$

This is based on the fact that $\boldsymbol{N} = \nabla\phi/|\nabla\phi|$. This equation is sometimes written as $\phi_t = F|\nabla\phi|$ where F is denoted as the speed function. Also note that now the curvature κ is computed from the level set ϕ directly [43]:

$$\kappa = \frac{\phi_{xx}\phi_y^2 - 2\phi_{xy}\phi_x\phi_y + \phi_{yy}\phi_x^2}{(\phi_x^2+\phi_y^2)^{\frac{3}{2}}} \tag{2.11}$$

Usually the signed distance functions are used as the level set function ϕ because of their desirable properties like the unit gradient magnitudes at all points. The function is defined as the distance between a point **X** and the curve described by the zero level set $\phi_0(x,y,t)$, and the sign of the function is determined by the relevant position of **X** with respect to $\phi_0(x,y,t)$. For example, positive if **X** is inside zero level set and negative if outside if we define $\boldsymbol{N}$ as the unit inward normal vector to the curve.

The geometric active contour models have many advantages over the parametric active contours. The energy minimisation problem is now interpreted in the context of the intrinsic geometric properties of the evolving curve such as curvature κ and normal vector $\boldsymbol{N}$, which can be directly computed from the level set function ϕ (e.g., $\boldsymbol{N} = \nabla\phi/|\nabla\phi|$ and κ has been given by equation 2.11). The methods are relatively easy to be extended to higher dimensional segmentation problem as the main idea of

representing the evolving contour/surface using a zero-level set of a function in a higher dimension remains unchanged. For example, for 3D segmentation problems, level set approaches can be applied by embedding the deforming surface into volumes [41].

The level set implementations, however, are subject to more intense computational cost. They accomplish the topological adaptability at the cost of increased dimensionality and hence additional computational burden (e.g., for the 2D case, a surface rather than a curve is evolved). In addition, as discussed above, the signed distance functions are generally used as the level set function ϕ. However, when ϕ evolves, it cannot remain as a signed distance function and re-initialisations of ϕ to a signed distance function from its zero-level periodically during the iterative evolution process is necessary [42]. This also adds to the computational expense. At last, the methods are also implemented using numerical approximation schemes like finite element or finite difference methods. The numerical stability and convergence of level set methods are subject to certain convergence criteria like the CFL condition (Courant-Friedrichs-Levy condition) that imposes limitations of the time-step size used to solve the level set equations, leading to further slow-down in the convergence speed [44].

Various approaches have been proposed to improve the computational efficiency of the level set based geometric active contour models. The "Narrow Band" method is among the most commonly used approaches, which only performs the iterative level set evolution and the re-initialisation in the areas near the zero-level curve [45, 46]. A fast marching level set method in which the speed function F never changes sign was introduced by Sethian in [47,48]. The evolving contour/front of the fast marching methods is always moving forward or backward so that the evolution problem can be converted to a stationary formulation because the contour will cross an image grid point only once. The conversion of the evolution to a stationary formulation has made the computation much more efficient. The two methods have also been

combined to achieve better improvement as in [49]. However, as discussed above, the time-step used in the evolution can be limited to small values to ensure the convergence of the level set method. This can make the computational time very long even with the aid of the narrow band and fast marching methods [50]. To solve this problem, the semi-implicit time discretisation schemes are used [50]-[52]. For example, the use of the unconditionally stable numerical algorithm, AOS (additive operator splitting) scheme, can enable rather large time step size while keeping the convergence of the iterative process [53].

Those methods can improve the computational efficiency significantly. However, the already-high complexity of modelling the level set based geometrical active contours will also be significantly increased when those numerical algorithms are embedded. Another main drawback of the level set based active contours is that the contours are now represented implicitly. Thus the user-interactions or other user-defined constraints are much more difficult/complex to be implemented compared to the explicit active contours. In this work, we have aimed to avoid those problems by not using numerical methods/schemes and retaining an explicit water flow front, whilst achieving the advantages of the geometric active contours such as the topological adaptability and geometrical flexibility. In summary, the work aims to construct a contour evolution based method with comparable performance to geometrical active contours at a significantly lower level of modelling complexity.

2.3 Design of external image forces

We have now introduced the frameworks of the two main families of active contour models, and briefly discussed the numerical stability and convergence issues. There is, however, another important area to which enormous effort from many researchers has been made, the design of the image forces guiding the contour evolution process.

The stopping function used in the previous examples, $g(|\nabla I|)$, is simply a

monotonic function of the image gradient. The image forces derived from this, $-\nabla g(|\nabla I|)$, are generally named as potential forces. As discussed in [22, 29, 30], the potential forces have limited capture range and weaken drastically and quickly away from the object boundary. The limited capture range, together with the non-convex nature of the energy functional being minimised, often lead to convergence to local rather than global minimisations. Thus a good initialisation close to the object boundary of interest is needed for active contours based on the traditional potential forces. Furthermore, the potential forces are normal to the object boundary lines, so at boundary concavities, the potential forces may not be helpful in pulling the contour into the concavities. This is further discussed and illustrated in chapter 3.

One method proposed to increase the capture range of snakes is the multi-resolution based techniques [54], which solve iteratively the minimisation/contour deformation problem at successive scales. The multi-resolution methods addressed the capture range issue, but determining how the snake should move across different resolutions remains problematic.

Cohen and Cohen [26] proposed an external force model that significantly increases the capture range of active contours based on potential forces, the distance potential force. The force is defined as the negative gradient of a potential function which is computed using a Euclidean / Chamfer distance map. The distance potential forces also point towards the object boundary but have much larger magnitudes at positions far away from the object, and thus increased the capture range and reduced the sensitivity of the active contour models to initialisations.

However, the distance potential force also fails to converge to boundary concavities as its direction has same properties to the traditional potential force. Balloon/pressure forces are then introduced to "push" or "pull" the active contours into boundary concavities. This is essentially a constant force normal to the evolving contours. For

example, adding pressure force to the geodesic active contour model discussed in section 2.2 is equivalent to adding a constant p to the curvature κ so that the first term in the RHS of equation (2.8) becomes $g(|\nabla I|)\,(\kappa + p)\,\boldsymbol{N}$. The pressure forces always have the same direction as the normal vector N and hence can help the active contour keep progressing into the boundary concavities. However, the force cannot be set too strong because otherwise weak edges would be overwhelmed, which makes the application of the balloon force difficult.

Xu and Prince [22,29] developed a well-known force term, the gradient vector flow (GVF) force to increase the capture range as well we overcome the boundary concavities problem. The gradient vector flow force gradient vector flow field $\boldsymbol{v}(x,y) = [u(x,y), v(x,y)]$ is obtained by minimising an energy functional given by

$$E = \iint [\mu(u_x^2 + u_y^2 + v_x^2 + v_y^2) + |\nabla f|^2 |\boldsymbol{v} - \nabla f|^2] dxdy \qquad (2.12)$$

where f is the edge map of the image and has various definitions (e.g., $|\nabla I|^2$ or $-I$), and μ is a regularisation parameter. From equation (2.12), we see that when $|\nabla f|$ is small, the energy functional is dominated by the sum of the squares of the partial derivatives of the vector field itself, yielding a slowly-varying force field. When $|\nabla f|$ is large, the second term in the RHS dominates the energy, and is minimized by setting $\boldsymbol{v} = \nabla f$. Therefore, the derived $\boldsymbol{v}$ would be nearly equal to the gradient of the edge map when it is large, and would be slowly-varying in homogeneous regions. Thus the capture range of active contours based on this GVF field can be increased. The GVF force still has difficulties to conform to long and thin boundary indentations. This is considered to be because of the excessive smoothing of the GVF field near the boundaries, governed by the first term in the RHS of equation (2.12). A GGVF (generalised gradient vector flow) field is thus introduced by Xu and Prince in [30], where a spatially-varying weighting function is used to substitute the constant regularisation parameter μ, and the smoothing effect is designed to reduce near

strong gradients. This field has been shown to have superior performance in detecting thin and long boundary indentations. The GVF and GGVF fields are initially introduced with the parametric snake models. Paragios et al. [55] has integrated the GVF field with the geodesic active contour, which has combined the advantages of geodesic active contours and the GVF force.

One common drawback of the GVF and GGVF is that the *calculus of variations* and numerical methods have to be used to solve the minimisation problem which introduce further complexity and computational cost. Furthermore, the GVF and GGVF based active contours cannot converge where the vector flows are tangent to the deforming contour or diverge within the neighbourhood (i.e., vectors form saddle or stationary points). In the GVF based geodesic active contour model, an adaptive balloon force has been introduced to overcome the problem when vector flows being tangent to the contour, but the saddle or stationary points problems remain unsolved. Various researchers have conducted works to overcome the problems, like the CVF (curvature vector flow) method which evolve the object boundaries according to the mean curvature flow until they are no longer concave. This method makes sure the active contour converge to very highly concave shapes which cannot be handled by GVF methods. It also reduces the number of saddle and stationary points formed but cannot completely eliminate them. One solution to this problem is to use dynamic rather than static vector fields so that the vector field can update itself when contours evolve and hence those critical points would change as active contours moves. For example, the charged active contour [56] defines a boundary attraction force and a boundary competition force in analogy to the electrostatic force field. The boundary attraction force pulls the active contours towards the object boundaries, whilst the boundary competition force is the repelling forces exerted by the part of contours reaching boundaries - it repels the contours not yet residing at boundaries from reaching the already occupied/detected boundaries. Both forces are updated as the contours evolve, and thus can change the saddle and stationary points when contours approaching. Another example is the Magnetostatic Field based active contours [57].

The method is based on the magnetostatic theory, where a hypothesised magnetic interaction forces between the active contours and image gradients are used to drive the contour deformation. This method is further discussed and reviewed in chapter 4 when integrating the force field theories to the proposed water flow model.

The forces discussed above are all boundary (or image gradient) based forces. The other important class of image forces used in active contour models, is the region-based forces. Those techniques use regional statistics and/or probabilistic likelihood information instead of image boundaries to define the energy functional being minimised and thus obtain the region-based forces. Here we review two main classes of the region-based active contour models.

Many of the region-based methods have been inspired by the Mumford and Shah model [58], where a curve $\mathcal{C}$ splits the domain Ω in foreground R and background R' and the image I is a degraded version of an ideal image F that is assumed to be smooth inside the segments R and R' but not on the curve/boundary $\mathcal{C}$. The concept of this model has been used to derive a new force term governing the active contour deformation, and the evolution equation of the corresponding geometric active contour model is given below [59] (written in the same manner as equation (2.9)).

$$c_t(s,t) = \mathcal{N}\{\kappa + (\beta_1(F_R - I)^2 - \beta_2(F_{R'} - I)^2) + (\gamma_1(\nabla F_R)^2 - \gamma_2(\nabla F_{R'})^2)\} \quad (2.13)$$

where β_1, β_2, γ_1, γ_2 are positive constants. Note that the ideal image F is unknown and should be re-estimated as the curve deforms [60]. Chan and Vese [23, 61] introduced a reduced version of the Mumford-Shah model, where F is reduced to a piecewise constant function. That is, $F = \mu_1$ for component R (inside the contour) and $F = \mu_2$ for R' (outside the contour), where μ_1 and μ_2 are constants respectively computed as the averages of the inside and outside regions. The corresponding geometric active contour evolves according to the equation (2.14).

$$c_t(s,t) = \mathcal{N}\{\kappa + (\beta_1(\mu_1 - I)^2 - \beta_2(\mu_2 - I)^2\} \quad (2.14)$$

The other important class of region-based active contours does not assume piecewise smooth intensities and aims to segment the image into statistically homogeneous regions. One of the first such models is the region competition method proposed in [62]. The method was first introduced in the context of the parametric snake model but can be easily combined with the geometric active contour models. The algorithm combines the region merging techniques and the active contours. The image plane is divided by the active contours into different regions. Some assumptions regarding the probability distributions of the regions are then made, so that the key parameters specifying a particular probability distribution can be estimated using the maximum likelihood estimation (MLE) technique. For example, for Gaussian distributions, the mean and variance of the region should be estimated using the pdf of Gaussian distributions. Then the probability of a contour point x belonging to a particular region R_i conditional on the estimated parameters can be computed. Denoting this probability as $Pr(x|R_i)$ and combing the region competition force with the geodesic active contour model, we have

$$c_t = g(|\nabla I|)\,\kappa \mathcal{N} - (\nabla g(|\nabla I|)\cdot \mathcal{N})\mathcal{N} + \alpha \log \frac{Pr(x|R_{\text{int}})}{Pr(x|R_{\text{ext}})}\,\mathcal{N} \qquad (2.15)$$

where α is a constant weight, R_{int} and R_{ext} are the internal and external regions respectively. Note that here we have assumed only two regions (so one closed deforming contour). The boundary-based potential force have also been used in (2.15). This can be eliminated by setting function $g \equiv u$ where u is a constant.

The structure discussed above have been applied to solve various practical problems like the bimodal image segmentation [63], and the texture detection [64,65,66]. The main difference between those applications is that the statistics used to derive the region-based forces are computed on different image features that provide optimum discriminatory power for the considered applications. For example, texture-based region statistics have been used in [64,65,66].

Region-based energy can give a large basin of attraction and can converge even when

explicit edges do not exist. However, purely region based forces often cannot yield as good localization of the contour near the boundaries as the boundary-based methods. This can be resolved by combing the boundary- and region-based forces, as shown in equation (2.15).

In this work, we mainly concentrate on the framework of the proposed water flow based contour evolution method rather than the design of the forces, and we have used an image force that combines a boundary-based force and a region-based one. The two forces are similar to those given in equations (2.10) and (2.14), respectively. This could be considered as an example showing how the image forces proposed for and used by active contour models can be easily adopted in our new framework.

Chapter 3

Water Flow Analogy

3.1 Introduction

The new technique aims to detect objects with closed shape easily and accurately whilst retaining smoothness. We use an analogy to water flow, which is a compromise between several factors: the position of the leading front of a water flow depends on

a) water pressure;
b) flow resistance / viscosity;
c) surface tension; and
d) adhesion / capillary action.

There are some other properties, like turbulence, which are ignored here as these are not desirable attributes for the sake of shape detection.

The fluidity of water makes flow possible into all branches and bifurcations of a watercourse. The edges and some other characteristics that can be used to distinguish objects of interest and background may be treated as the walls terminating the flow.

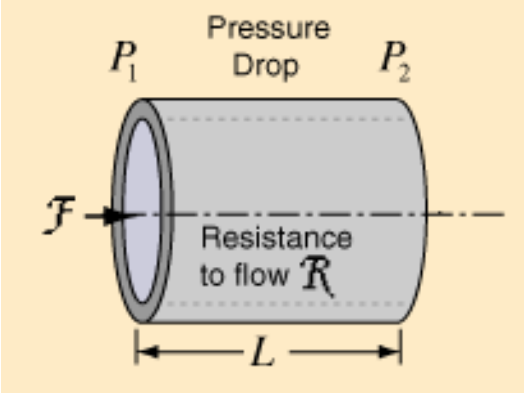

Figure 3.1: A simple flow model

The final static shape of the water will describe the corresponding object's contour. Intuitively, this method is able to overcome the problems brought by complex topology and can be applied without prior knowledge of the target's shape. Besides this, the new technique has the fundamental advantage of physical models - their working principles and input variables and parameters are explicit, compared to mathematical models like level sets and snakes whose principles and parameters are generally implicit and abstract. Further, there is physical understanding to guide selection of parameters that control the flow of water.

Essentially, flow is determined by flow driving force and resistance. A simple smooth flow model is presented in figure 3.1 where only pressure difference is considered. The relationship between the flow rate $\mathcal{F}$, the flow resistance R and the pressure difference, is given by equation (3.1).

$$\mathcal{F} = \frac{P_1 - P_2}{R} \tag{3.1}$$

where P_1, P_2 are pressure of inflow and outflow, respectively. The difference between pressures drives the flow, and the flow rate can also be described by

$$\mathcal{F} = AV_{effective} \tag{3.2}$$

where A is the cross-sectional area and $V_{effective}$ is the effective flow velocity. Combining equations (3.1) and (3.2), we can relate the flow velocity with the pressure difference, the flow resistance and the area:

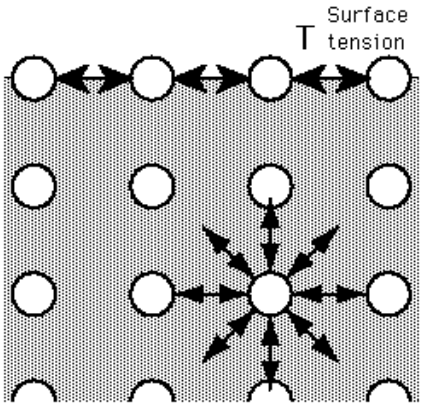

Figure 3.2: Repulsive forces and surface tension

$$V_{effective} = \frac{P_1 - P_2}{AR} \tag{3.3}$$

In the image analogy, we can assume that each pixel is a water element with unit volume. Then by defining the water forces giving rise to the pressure difference and the resistance to flow, the flow velocity of each mobile water element can be calculated through equation (3.3).

In real-world images, however, there are often small discontinuities or weakly contrasted regions in the object boundaries. These can lead to corresponding gaps and weak/blurred walls of the "watercourse". As a consequence, the "water" may leak from the object into the background. It is also a significant problem for many other image segmentation operators like region growing and snakes. The detected shape may be significantly anamorphic due to the blurred boundaries or edge gaps. Another important property of water, a cohesive force, is then introduced to solve the problem. The forces exist between water molecules, as shown in figure 3.2. We can see that the forces between internal water elements are shared with all neighbouring elements, whereas those on the surface have no neighbouring points above and exhibit stronger attractive forces upon their nearest *surface* neighbours. This attraction force is defined as the surface tension which can help water form a surface "film" to bridge some gaps. A good example in real life is the use of water for cleaning. Water with lower temperature will have higher surface tension. Cold water therefore is not a good cleaning agent. The relatively high surface tension would

make it "bridge" surface pores and fissures of the object being cleaned rather than getting into them. Analogically, building the concept of surface tension into the water flow model can be expected to make the new technique overcome the problem of boundary gaps or weak edges. In addition, the surface tension in effect imposes a constraint to the flowing fronts and hence can help to maintain the smoothness of the flowing water contours.

There is another kind of force often incorporated with the surface tension. It can assist surface tension to allow flow inside narrow branches and leads to a phenomenon called Capillary Action. An example is shown by figure 3.3. In physics, Capillary Action refers to the process of water moving up a narrow tube against the force of gravity. It occurs because water adheres to the sides of the tube, and then surface tension tends to straighten the surface making the surface rise. This is a desirable property for the analogy because narrow branch-like feature detection is often needed in practical image processing applications. To imitate the action, this additional force, named as the adhesive force, is also embodied in the new technique. In physical models, adhesion is the attractive forces existing between water surface elements and the walls of watercourses. Accordingly, in image processing analogy, it is naturally defined as the attractive force to water contours from the object edges. It helps to overcome small discontinuities in edges and to avoid bridging the "entrance"

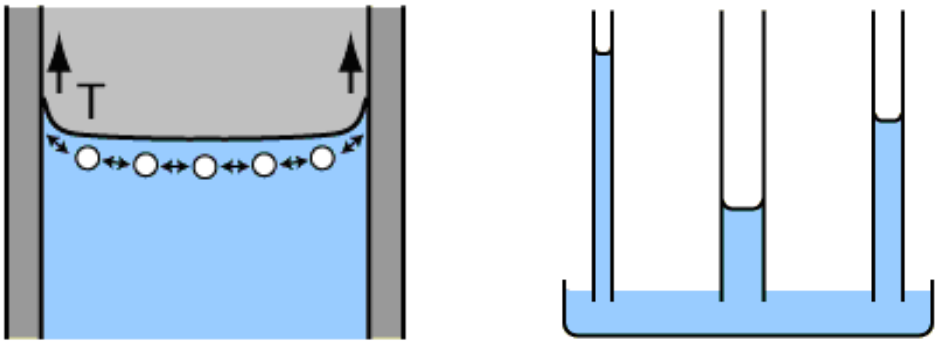

Figure 3.3: Capillary action: adhesion of water to the walls gives an upward force on the water at the edges and leads to a meniscus moving upward. The surface tension acts to hold the surface intact, so instead of just the edges adjacent to the walls moving upward, the whole water surface is dragged upward.

of very narrow branches. The latter objective is achieved by capillary action which should be similar to figure 3.3.

3.2 Framework

The framework of the method is first introduced. Rather than using Finite Difference approaches or Partial Differential Equations that are commonly used in computer simulations of water flows, a simplified physical analogy structure is considered sufficient for digital image analysis purpose and thus is used here. The water flow is dictated using dynamical formulae and laws such as equation (3.3) and conservation of energy. The general ideas underlying the water flow model is given by figure 3.4.

As shown by figure 3.4, for a given water element, the flow driving force arising from the water pressure and the adhesion, balanced with the smoothing force (the surface tension), can produce an initial flow velocity, which makes the element start moving/flowing. On the other hand, the region- and boundary-based image forces would be imposed on the moving element to accelerate / decelerate the flow process.

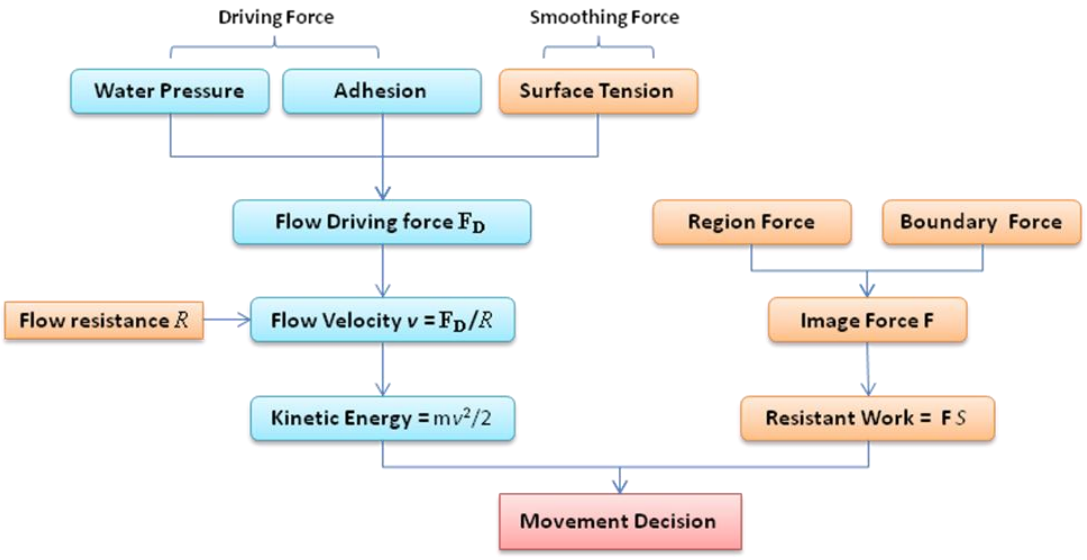

Figure 3.4: The general structure of the water flow method, where *m* is the mass value of a synthetic water element and *S* is the distance of one single movement step. The two parameters can all be set as constants.

To decide whether or not the image force can prevent the water element finishing the movement (i.e., velocity is decelerated to 0 before arriving at the destination), the kinetic energy that is a function of velocity and the work that is a function of the image force are computed respectively and then compared with each other. Only if the kinetic energy exceeds the image resistant work, can the element reach the destination of the flow.

Having introduced the general principles, the detailed implementation of the model is then presented. First, we need to make some assumptions so that the digital image processing can be coupled with the physical phenomenon. The images used are digitized and thus the elements are discrete. One pixel in the image is considered to be one basic element of the water. An inexhaustible and adaptive water source is assumed so that the water flows until stasis, where flow ceases. The water is divided into two components: interior points and contour points. The pixel-based characteristic of the new method implies that topological changes such as region merging can be easily achieved. We use figure 3.5 as an example, where two water sections collide and merge together. The elements on the flow fronts collided will be totally surrounded by adjacent water elements and thus should be treated as internal elements. The two parts will then merge as shown in figure 3.5b and the topology is now changed.

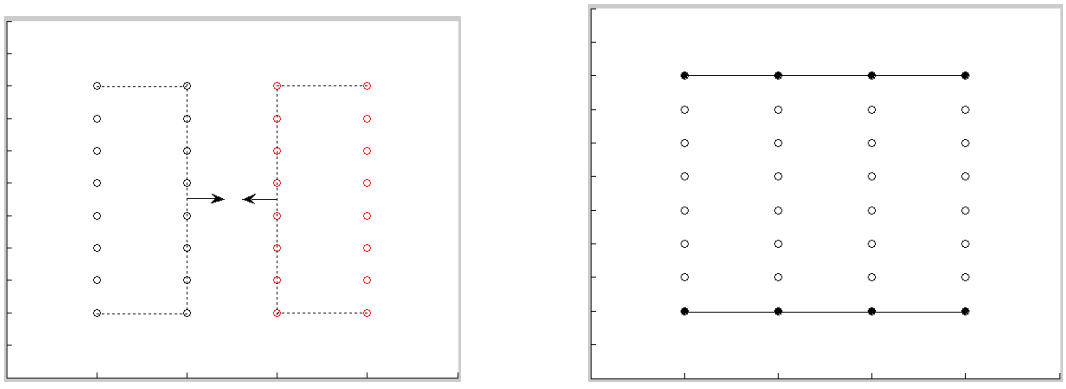

(a) (b)

Figure 3.5: An example of the dynamics of the water flow. (a) Two water components are colliding, where contours are represented by dotted lines; (b) the merging result, where boundaries are lines connecting black points.

Further assumptions include the magnitude of the water pressure and of the surface tension. The pressure between an interior water element and each of its neighbours is set to be the same. Surface tension, which in physics should be a little bigger than the internal water pressure, is defined to be adjustable by users.

The first step of the analogy is initialization. As the method has little dependence on the starting contour shape, either a point or a geometrical shape, can be defined as an initial location of the water source. The pressure acting on an interior element sums to zero due to the symmetrical distribution of neighbours; and thus it has a flow velocity of zero according to equation (3.3). A water contour element, however, has asymmetrically distributed neighbours together with the surface tension and the adhesive force (if any). Therefore, it has non-zero pressure difference ΔP which leads to a non-zero flow velocity, and it is possible to move outwards. Consequently, only water elements on the contour are of interest in the implementation. Because of the assumption of inexhaustible water source(s), after the contour element moves out, the empty left behind will be replaced by new water elements. Therefore, one contour element, in effect, is able to flow to multiple adjacent positions.

The flowchart in figure 3.6 shows the operation steps of the water flow process for a single contour element in one iteration. The whole framework of the new technique is then introduced with reference to this flowchart.

It should be noted that there are two loops in one time step. The first loop denoted as the *external* loop examines the flow situation of current contour elements one by one. Then for each contour element, all of its possible flow directions are examined during the second loop, as shown by the flow chart below. Denoting the latter loop as *internal* loop, one iteration of which is considered as one *basic iteration* of the flow process.

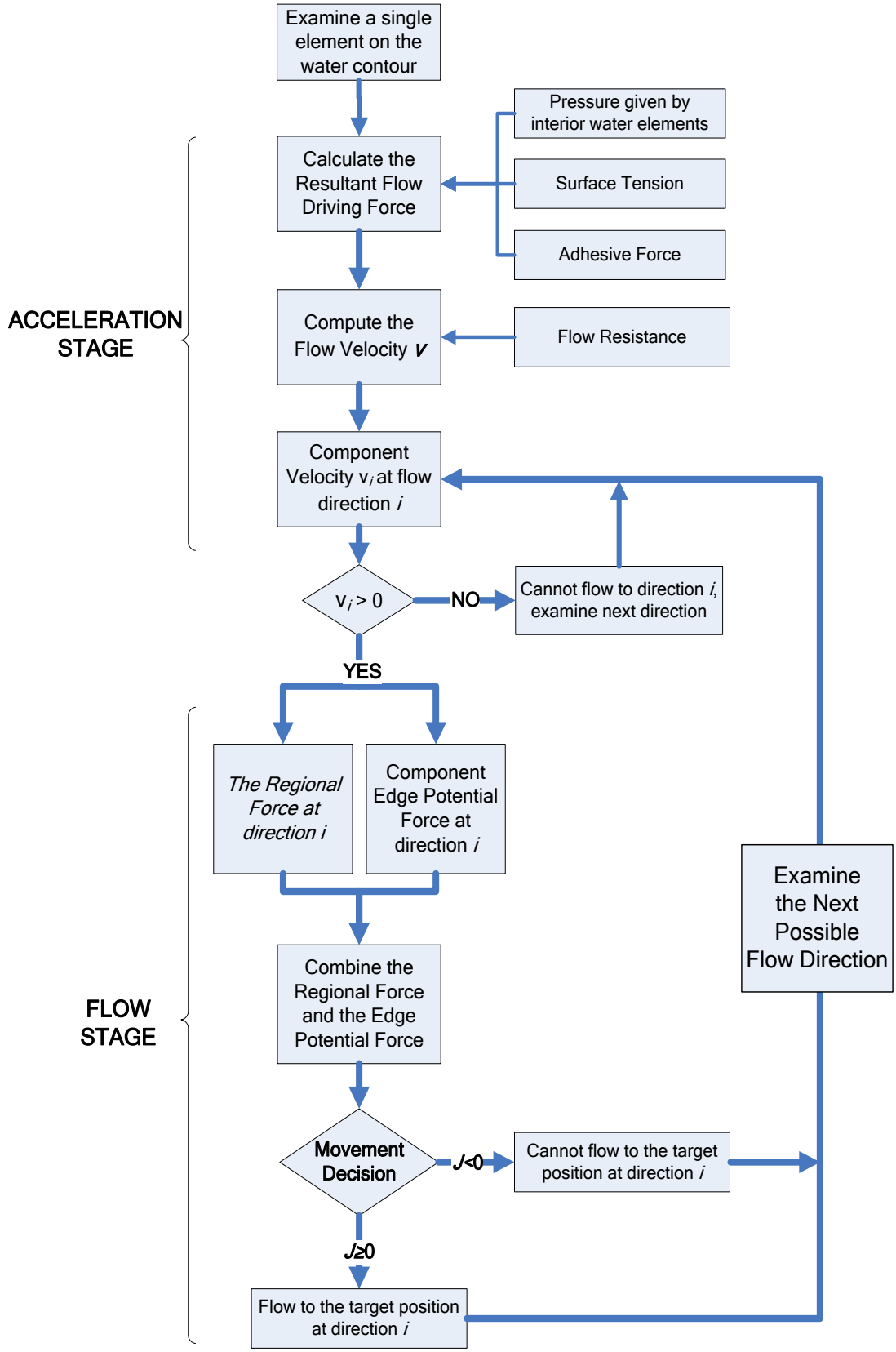

Figure 3.6: Flow Chart of the water flow operation for a single contour element. The Movement Decision *J* is explained later. A complete flow iteration of the whole water will be achieved by applying the same process to all the current contour elements.

The flow process is assumed to be a unification of two separate stages. The first stage is an "acceleration" process: the contour element achieves a velocity due to the presence of pressure difference, surface tension, and any adhesive force that might exist, and the ultimate value is given by equation (3.3). Figure 3.7 indicates simple examples of the mechanics of this step. From figure 3.7a, we can see that water contour element **A** now achieves a positive initial velocity pointing upwards. The resultant velocity can be decomposed into three directions and thus the considered contour element can move to the three adjacent positions. Furthermore, figure 3.7b presents a situation where surface tension holds contour element **B** and hence prevents the flow.

If the contour element has a velocity pointing outwards, it is then assumed to depart from the whole water body and flow outwards. This is the "Flow Stage", during which the flowing element is assumed to be acted on by some image forces only. That is, it now suffers no influence from other water elements. This is not consistent with the real physical operation but is sufficient for the digital image analogy and greatly simplifies the algorithm.

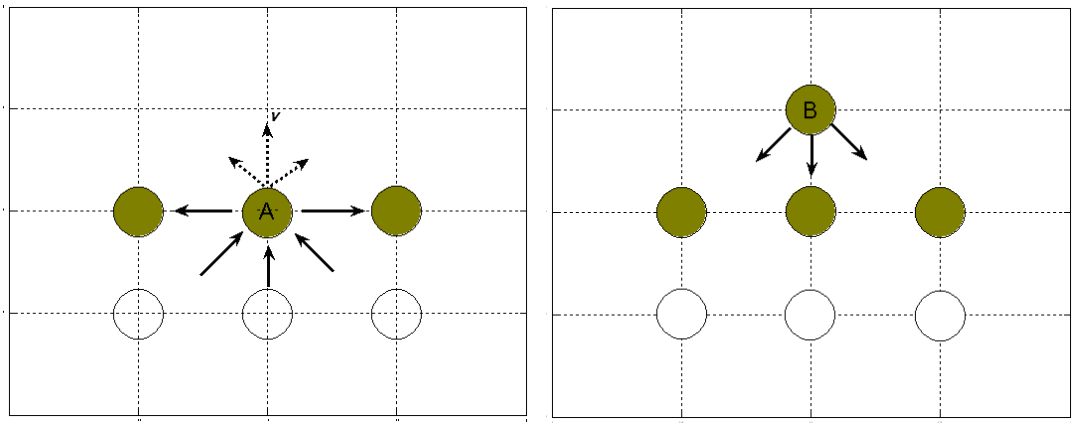

(a) (b)

Figure 3.7: Examples of the mechanics of the acceleration step, where the contour element considered is positioned a) at a flat contour and, b) at the peak of a hump (high curvature) on the water contour. Grey points represent contour elements and white ones are internal water elements. Plain arrows stand for repulsive (water pressure) and attractive (surface tension) forces, while the dashed ones in (a) are velocity components resulting from the forces.

The contour element can move to any possible direction for which the relevant velocity component is positive. Therefore we first need to find all the possible flow directions. Under eight-way connectivity, the directions pointing outwards from the whole water body among the total eight possible ones are the initial possible flow directions. Then the component of flow velocity in each of the directions is examined: all the directions with non-positive-valued velocity component values are rejected and the others are considered to be the final possible flow directions. The implementation process then comes into the "Flow Stage" where the movements of the contour element in each of the possible flow directions are examined, respectively.

Only contour elements with sufficient initial flow velocity component can reach the target position at the direction of interest. To reconcile the flow velocity with the forces, dynamical formulae can be used. We can compute the displacement of a contour element in each possible direction within a fixed time interval, which should be similar to classical snake techniques. Alternatively, to avoid the interpolation problem, a framework similar to region growing can be used: the water element will flow to adjacent positions if it can satisfy certain conditions (e.g., formulae such as the theorem of momentum). The latter framework is used here for simplicity.

First, the definitions of kinetic energy and resistant work are employed. Assuming that the contour element of interest has a scalar velocity component v_i in a possible flow direction i (hence $v_i > 0$) and is acted on by related image force F_i during moving a distance D, then the initial kinetic energy of the element $E_{Kinetic,i}$ is given by

$$E_{Kinetic,i} = \frac{1}{2} m v_i^2 \tag{3.4}$$

where m is the assumed element mass. The *resistant* work $W_{R,i}$ given by F_i is

$$W_{R,i} = -F_i D \tag{3.5}$$

Note that F_i is a scalar which is positive when the corresponding component of the image force is consistent with the direction i, and negative otherwise. Because $W_{R,i}$ is

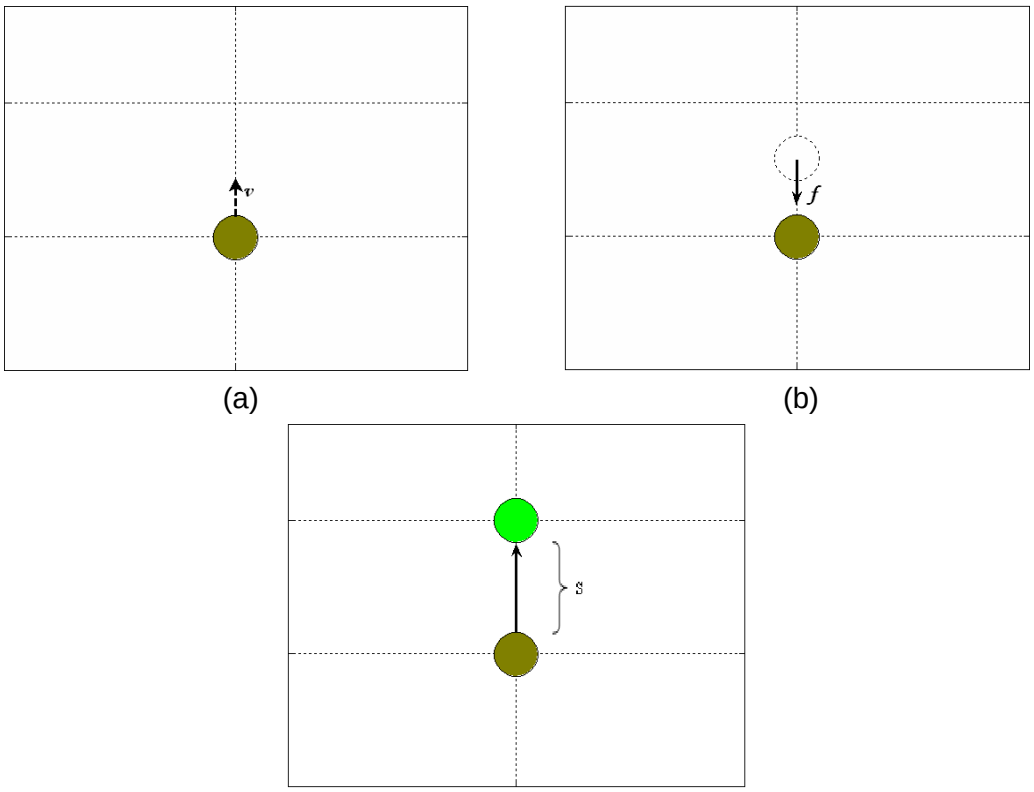

Figure 3.8: An example of the Flow Stage of a contour element. (a) The contour element gains an initial velocity v at the direction of interest after the Acceleration Stage; (b) during the Flow Stage, the component of the image resistant force at this direction, f, acted on the element (dotted circle); (c) the initial kinetic energy is sufficient for the element moving a distance of S and ultimately reach the target at this direction. If the initial kinetic energy is not big enough, the element is assumed to be 'pulled' back to the origin and the target position from this origin is considered as inaccessible.

defined as the Resistant work, it is positive when F_i is resistant to the flow toward direction i ($F_i < 0$). Here we assume that the flow distance in a single iteration is fixed, denoted as S. Since there is only an image force F_i acting on the element during the Flow Stage, to examine whether or not the contour element can ultimately move to the targeted position at direction i, we just need to compare the initial kinetic energy arising from the Acceleration Stage and the resistant work during the displacement of S. A Movement Decision function can be defined accordingly:

$$J = E_{Kinetic,i} - W_{R,i} \tag{3.6}$$

If $J \geq 0$, the initial kinetic energy is large enough to overcome the resistant force in the Flow Stage and reach the target position at direction i. If $J < 0$, $E_{Kinetic,i}$ is not

sufficient to overcome the resistant force and the target position at direction *i* will not be flooded. Figure 3.8 gives an example of the Flow Stage where the contour element overcomes the component of resistant image force and reaches the target position. As shown by figure 3.6, the flow processes toward the other possible directions are then examined, respectively. Applying the same procedures to all the current contour elements gives rise to a complete flow iteration of the whole.

Figure 3.9 shows an example of the analogical flow process. The water is flowing inside a cube whose edges are assumed to be strong enough to prevent the flow. Furthermore, there is a gap on the lower edge line. The water flow analogy process has shown two distinctive properties: a) a flow front is preserved during the flow; b) the gap is bridged as a result of the surface tension as shown by figure 3.9d.

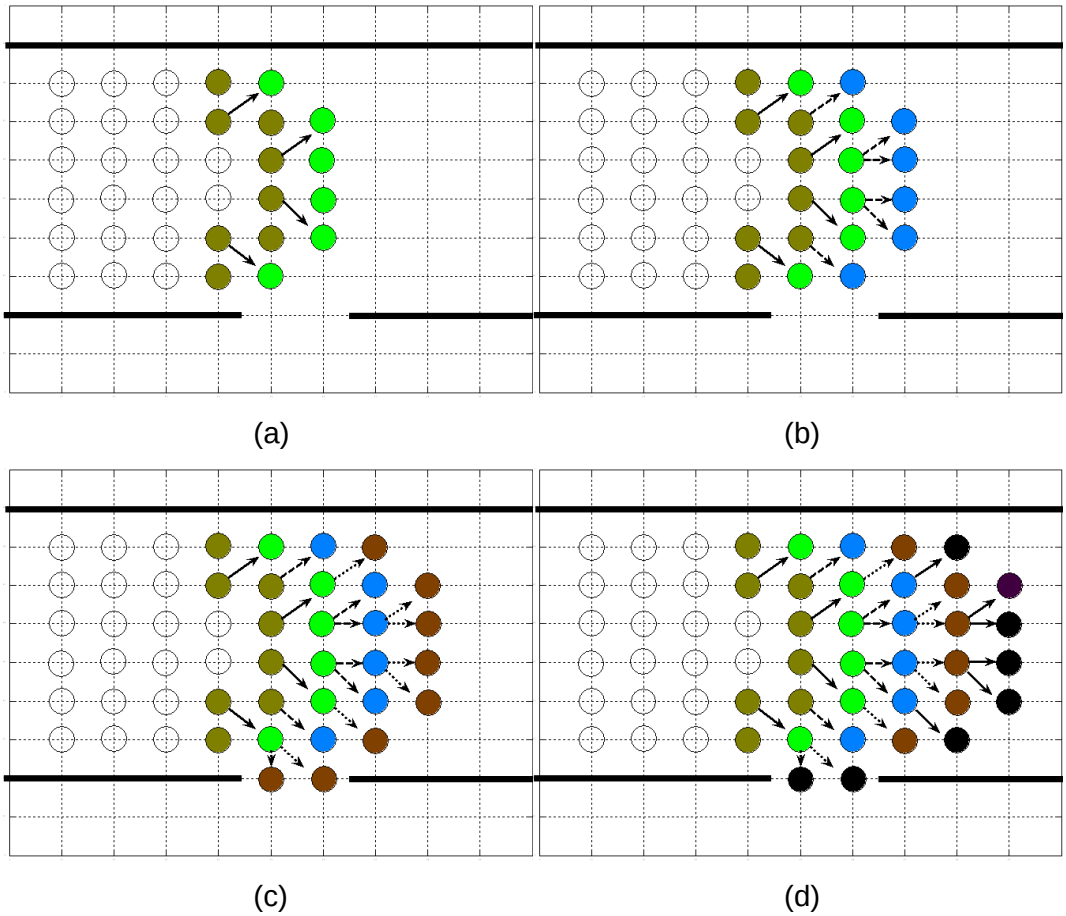

Figure 3.9: Water flow inside a cube with a gap on its lower edge. (a) – (d) show the 4 iterations, respectively. Different colours are used to differentiate the propagating water contour elements.

In following sections, the factors computing each of the terms in equation (3.6) will be defined by the order given by figure 3.6. A new expression of *J* which unifies those factors will also be presented. We only need to consider one "basic iteration". That is, the movement of a single contour element at one of its possible flow directions.

3.3 Flow driving force

The first step of the implementation is to find the water contour. Here eight-way connectivity is used to define the contour points. If an element is not completely surrounded by other water elements, it is a contour element.

The flow driving force, as discussed above, is the resultant force of water pressure, surface tension and adhesion. We first ignore the latter two and will embody them into the driving force later. From physical knowledge, the direction of the resultant force is outwards, normal to the contour, with strength determined by the adjacent water elements. Since the flow in each possible direction will be examined separately, the component of force rather than the resultant force is of interest.

The force in the direction of interest can be computed directly by template convolution. In a 3×3 window, there are eight directions from the centre to the boundary. Four of the eight possible convolution masks are shown in figure 3.10. They are centred at the contour point of interest. The connected 0's form a line

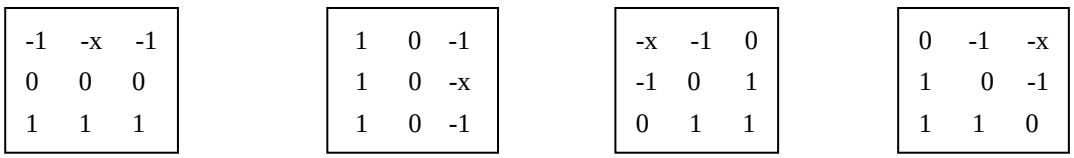

(a) (b) (c) (d)

Figure 3.10: the convolution masks for calculating the force component pointing towards the direction of a) 90-degree, b) 0-degree, c) 135-degree, and d) 45-degree, respectively.

normal to the associated possible flow direction and the "-x" point gives the flow target at this flow direction. This position has not been occupied by a water element and hence the value of x will not influence the convolution result. The other four masks can be achieved by transposing the ones shown in figure 3.10. By symmetry, if we define negative convolution results as the driving forces in opposite directions, four masks are enough for the implementation. We can see that by this directional convolution method the force component for a particular direction is decided by the local surface interior, i.e., the amount and position of the adjacent water elements. For a certain direction, there will be supporting and opposing elements. The property is determined by their positions relative to the flow direction. The elements located at the normal line do not affect the movement and so are set to be 0. Separated by the normal, the elements located at the inner half exhibit positive effects on the flow and the opposite ones give negative forces when we only consider the water pressure which is formed by the repulsion between water elements. We assume the magnitudes are all unity.

A matrix **W** is used to save the water information where a water element has value one and others are all zeros. Denoting the convolution template for direction i as $\mathbf{T}_i$, the corresponding matrix saving the normalized driving force strength on direction i, $\mathbf{F}_{P,,i}$, is then calculated by the equation:

$$\mathbf{F}_{P,i} = \frac{\mathbf{W} * \mathbf{T}_i}{S_{PM}} \tag{3.7}$$

where S_{PM} is the possible maximum of the convolution sums. For each mask, the maximal value is achieved when water elements locate at all positions of 1's and none of those of -1's and hence S_{PM} = 3 for the above masks. The driving force strength on direction i at point (x, y) is then just the (x, y)th entry of $\mathbf{F}_{P,i}$. As shown in section 3.2, only contour elements have non-zero pressure differences. Thereby in practical implementation, only convolutions at contour positions are carried out to reduce the computational cost.

The directional template convolution mechanism is suited both to four-way and to eight-way connectivity. Further, the mask size can be expanded so that more local structure can be included and the calculation will be expected to give a more reasonable result. For instance, the driving force at one end of a single straight line would be smaller when using a 5×5 mask than that by a 3×3 mask, because the possible maximum is much larger (from 3 to 10) but the convolution sum is increased by only 1. In addition, using a larger mask size is expected to make errors due to the effects of noise to be reduced by local averaging within the larger neighbourhood. However, mask expansions will lead to exponentially increased complexity of implementation. There are 8 (3^2-1) directional masks needed for a 3×3 convolution mask. Similarly, 24 (5^2-1) masks are needed for a 5×5 mask, and 48 (7^2-1) for a 7×7 mask.

The driving force results from the pressure difference between water elements, and the gradient of **W** gives the information of pressure difference. Replacing –x's in the convolution masks in figure 3.10 by -1's, the templates then become the well-known Robinson's compass gradient detectors [67] with opposite direction (the gradient points from the lower intensity to the higher one, and the driving force acts in opposite to this). In general, the resultant flow driving force can be defined as the negative gradient of the water matrix **W**:

$$\mathbf{F}_P = -\nabla \mathbf{W} \tag{3.8}$$

where ∇ is the gradient operator and $\mathbf{F}_P$ is the corresponding matrix saving the resultant *vector* forces, respectively. It is the force components at the possible flow directions that are of interest, so a force decomposition process is followed.

Assume the coordinates of the contour element of interest is (x_c, y_c), then the corresponding resultant force vector is $\mathbf{F}_P(x_c, y_c)$. The angle between the direction of $\mathbf{F}_P(x_c, y_c)$ and the flow direction of interest is calculated by the definition of vector's dot product. Assuming that the flow direction vector is **K** and the force direction is **N**,

the cosine of the angle between the two vectors is given by equation (3.9).

$$\cos\gamma = \frac{\mathbf{K}\bullet\mathbf{N}}{|\mathbf{K}||\mathbf{N}|} \tag{3.9}$$

For the considered contour element and the flow direction i, denoting this angle as θ_i, we have the directional force component

$$F_{P,i} = F_P \cos\theta_i \tag{3.10}$$

where F_P refers to the magnitude of $\mathbf{F}_P(x_c, y_c)$ and $F_{P,i}$ is the magnitude of the force component of $\mathbf{F}_P(x_c, y_c)$ in direction i.

The template convolution method also makes the incorporation of additional forces (the surface tension and the adhesive force) straightforward and explicit.

3.4 Surface tension and adhesive force

Introducing viscosity in watershed methods [68, 69] is either complicated or indirect. In snakes, the smoothness constraints are achieved by minimising certain energy functionals, the process of which is also implicit. In comparison, the water flow model can be coupled with the constraint easily and explicitly. The surface tension, as introduced in section 3.1, is a natural choice for smoothness constraint. As in the real world, the flow driving force combined with surface tension is expected to handle problems like edge discontinuities and "gaps" on the boundaries of the object(s) of interest. In such cases, the surface tension should bridge the small gaps. In addition, the new driving force should penalise the generation of corners and cusps on the flow contour so as to maintain the smoothness of the extracted contour.

From physics, the surface tension is decided by the temperature and the water itself. In the image analogy, it is identical to constant attractive forces between adjacent contour elements. The convolution method of computing the driving force makes the application very straightforward: simply modifying the convolution masks with the position information of the contour elements will lead to the new driving force.

A matrix **C** is used to save the contour information. For example, if the pixel at (x, y) is a contour point of the water, then **C**(x, y) = – *t*, where *t* is a positive constant determined by users; otherwise, **C**(x, y) = 1. To incorporate the surface tension, we simply modify the water matrix **W** by setting the entries of the contour elements as –*t*. The new water matrix with surface tension taken into account is given by:

$$\mathbf{M} = \mathbf{C} .\bullet \mathbf{W} \tag{3.11}$$

where ".•" means an element-by-element multiplication. The absolute value of surface tension is *t* and is set by users for different degree of "viscosity". For instance, when dealing with large gaps or noisy corruptions, we can increase the value of *t* as well as the mask size. In this thesis, we simply set *t* = 1.

From the discussion above, equations (3.7) and (3.8) still hold with **W** replaced by **M**, and the possible maximum convolution sum is also changed. For equation (3.7), it is now (3+2*t*) for the size of 3×3. This is because the contour points now can also give positive effect on outflow. Using figure 3.10a as an indication, if the elements at the upper right and upper left corners are contour elements and the three ones at the bottom row are interior water elements, then the convolution sum will be (3+2*t*).

By introducing surface tension, it is now possible to get negative values of the flow driving force. Still look at the templates of figure 3.10. Now we assume that water elements only exist at the bottom row and the centre, and then all the 4 points can be regarded as contour points through eight-way connectivity (this is indeed the case shown by figure 3.7b). For the 90-degree, 45-degree and 135-degree directional templates shown by figure 3.10a, 3.10c and 3.10d, all the convolution sums are negative. For the 0-degree directional template, the result is 0. In this case, the corresponding contour element is restricted on all possible flow directions and cannot progress to the Flow Stage. This is analogical to what will happen when there is a cusp on the water surface or the water meets a hole on the object's surface. As a result, it can be expected that this surface tension modification should give a

sufficiently good approximation to the surface tension and hence help the water flow model to retain the contour smoothness and bridge the small gaps on the edge lines.

Nevertheless, the surface tension might prevent flow to narrow branch-like features because the "entrances" to them may be treated as gaps and thus are bridged as well. In this case, the adhesive force resulting from the branch walls/edges is expected to make flow continue like the capillary action. As shown in figure 3.3, the water should be pulled forward by the walls and hence keep flowing in the branch. The adhesive forces are essentially attractive forces from object boundaries to the water surface elements. Therefore in the image analogy, it is defined by the combination of the edge information and the current state of water.

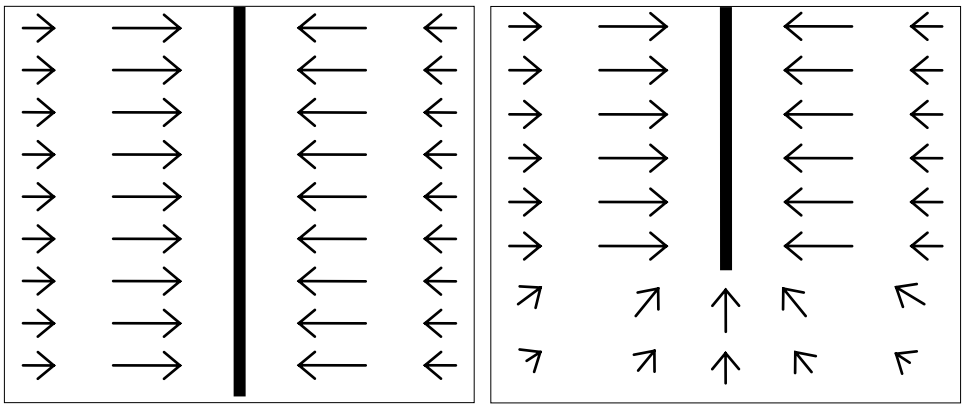

(a)Original edge line (b) Eroded edge line

Figure 3.11: The gradient of edge magnitudes shown by arrows where the length stands for the gradient magnitude.

The gradient of edge magnitudes is often defined as the edge potential force. It gives rise to vector forces pointing toward the edge lines [31, 32]. Furthermore, the force is large only in the immediate vicinity of edges and will decrease rapidly as the distance to edges increases. Consequently, it is intuitive to consider using the edge potential force to define the adhesive force on the start point. However, another property of the edge potential force, being *normal* to the edge lines, makes it useless for flow in a direction *along* the edge lines. For instance, the forces near the edges of a vertical branch are horizontal as shown in figure 3.11a and thus will not help the flow along

the edge line. To solve the problem, an edge map with "flooded" positions set to zero is used. In this map, the edge magnitudes at the positions having been occupied by the water are ignored so that edge lines become clipped. Then at the positions near edges, new gradients pointing from the flooded edges to the "surviving" parts will be generated. From figure 3.11b, we can see that the new gradients can assist in flow along the reserved edge lines. Therefore, this modified edge potential force is defined as the adhesion:

$$\mathbf{F}_A = \nabla \mathbf{D} \tag{3.12}$$

where **D** is the edge magnitude map which is generated by edge detectors like the Sobel operator [1] used here and eroded by the flowing water, and $\mathbf{F}_A$ is the matrix saving the adhesive force vectors. The adhesive force effectively defines the attractive force from edges to the water. Therefore, even if a water element has flowed onto an edge point, it can still move to the adjacent edges. This thus will help water flow into narrow branches and flood small noise pixel clusters, and the later effect contributes to the noise robustness.

Like equation (3.8), the adhesion force is also derived from the *gradient* of a matrix. Consequently, it is straightforward to integrate the computations of water pressure, surface tension and adhesion into a single operation. In matrix **D**, the entries at water flooded positions are zero-valued whilst in **M** the entries at "dry" positions are zero-valued. Note that equation (3.8) uses the negative gradient of **M**. This is equivalent to using the gradient of **–M**. The matrix combining water and edge information, **G**, is then given by

$$\mathbf{G} = \mathbf{-M + D} \tag{3.13}$$

The modified flow driving force embodying the water pressure, the surface tension and the adhesive force is then given by equation (3.14).

$$\mathbf{F}_D = \mathbf{F}_A + \mathbf{F}_P = -\nabla \mathbf{M} + \nabla \mathbf{D} = \nabla(-\mathbf{M} + \mathbf{D}) = \nabla \mathbf{G} \tag{3.14}$$

where $\mathbf{F}_D$ is the matrix saving the modified driving forces.

The scalar force at the considered contour element in the considered flow direction is

of interest. Denote the scalar force component in direction i at (x_c, y_c) as $F_{D,i}$. This scalar quantity is also calculated using equations (3.9) and (3.10) and will be used to define the corresponding flow velocity component in following sections.

3.5 Resistance to flow and the velocity

From equation (3.3), the velocity of flow is inversely proportional to the resistance of flow. In a physical model, the *flow resistance* is decided by the water itself, flow channel properties and temperature etc. Since this is a physical analogy which offers great freedom in parameter definitions, we can assign high resistance values for undesirable image characteristics and low values to chosen ones. For instance, in iris vessel detection, if the vessels have lower intensity compared to the background, then we can define the resistance to be proportional to the intensity of the "target" pixel. Particularly, if we couple the resistance with image features used for fitting the contour as the edge information, the process will become self-adaptive. That is, when the edge magnitude is strong, resistance would be large and so the flow velocity would be weakened. According to equations (3.4), (3.5) and (3.6), the movement decision will now be dominated by the force acting at the second exterior process. As a result, even if the driving force set by users is too "strong", the resistance would lower its influence at edge positions and thus the problem in balloon models [25], that strong driving forces may overwhelm "weak" edges, can be suppressed.

We first re-write equation (3.3) as

$$v_i = \frac{F_{D,i}}{A\mathcal{R}} \tag{3.15}$$

where v_i is the component of flow velocity of contour element at (x_c, y_c) resulting from the force component $F_{D,i}$. In the water flow model, A is assumed to be a constant. $\mathcal{R}$ is defined to be proportional to some intrinsic image attributes according to a user's special purpose (it can be set to be constant as well). Many kinds of functions can be used to define $\mathcal{R}$ such as exponential functions. From figure 3.12a

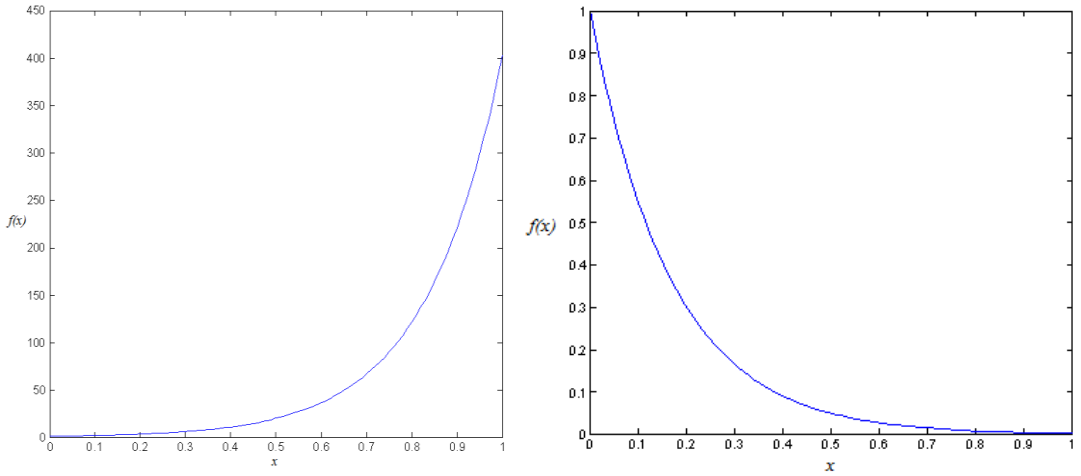

(a) (b)

Figure 3.12: (a) the graph of the example exponential function $f(x) = e^{10x}$, and (b) the reciprocal of $f(x)$ where we can see that the value range of the reciprocal function falls into the range of (0, 1] for $x \in [0, 1]$ (the minimum value here is e^{-10x}).

we can see that both the function value and the slope of the curve increase in line with input variable (i.e., the curve is convex). When the input is small, both the function value and the slope are close to zero. When the input exceeds a certain value, however, the function value will increase much more quickly. This is a desirable property. When the edge strength is small, the influence of the resistance should be minor. When the edge strength is above certain level / threshold, the probability of the related pixel being an edge point is considered to be relatively high and the significance of $\mathcal{R}$ should be improved rapidly along with the edge strength. As $\mathcal{R}$ is used as a divisor in equation (3.15), the inverse function of $\mathcal{R}$ is of interest and is shown in figure 3.12b. The inverse function's value approaches 0 rapidly when x exceeds a value (around 0.6). Consequently, an exponential function is suitable for defining $\mathcal{R}$:

$$\mathcal{R}=\exp\{k\,\mathbf{E}(x_c, y_c)\} \tag{3.16}$$

where **E** is the edge response map and k controls the rise/decrease velocity of the exponential curve. A larger value for k gives rise to a greater rising/falling rate of the curve. From equations (3.15) and (3.16), we can see that when water elements move onto edge pixels, the flow velocity will be reduced and then the significance of other terms, the image forces, will be emphasized.

3.6 Image forces

After calculating corresponding component of flow velocity, v_i, the first flow decision process needs to be applied. As shown by the flowchart in figure 3.6, only if v_i is positive, can the operation move to the next stage, the Flow Stage. The image force is the only force acting on the flowing element during this stage which is determined completely by the image information.

The edge potential force introduced in the section 3.4 is often used in active contour methods because it yields force vectors pointing toward the edge lines as shown in figure 3.11. This property means that the forces at two sides of an edge line have opposite directions. Thus the forces will attract approaching elements onto one side of the edges and then prevent them from moving on to the other side. This force, thereby, is adopted in this water flow model.

However, the definition of the edge potential force needs to be modified according to the framework of the flow model. The image force is presumed to act only during the Flow Stage where the water element has left the original position on the contour (x_c, y_c) and is moving to the flow target. Accordingly, the force acting in the Flow Stage shall be the potential force at the target flow position (x_t, y_t) which is the position adjacent to the considered contour element in direction i. In this way, the water elements will flow onto one side of the edges and then be prevented from overflowing to the other side. Denoting the potential force component in direction i as P_i, we have

$$P_i = |\nabla \mathbf{E}(x_t, y_t)| \cos \beta_i \qquad (3.17)$$

where β_i is the angle between direction i and the direction of the edge potential force at target position (x_t, y_t) , and $0 \le \beta_i \le \pi$. It should be noted that P_i is negative when $\beta_i > \pi$.

The edge potential force defined above works well as long as the gradient of edges

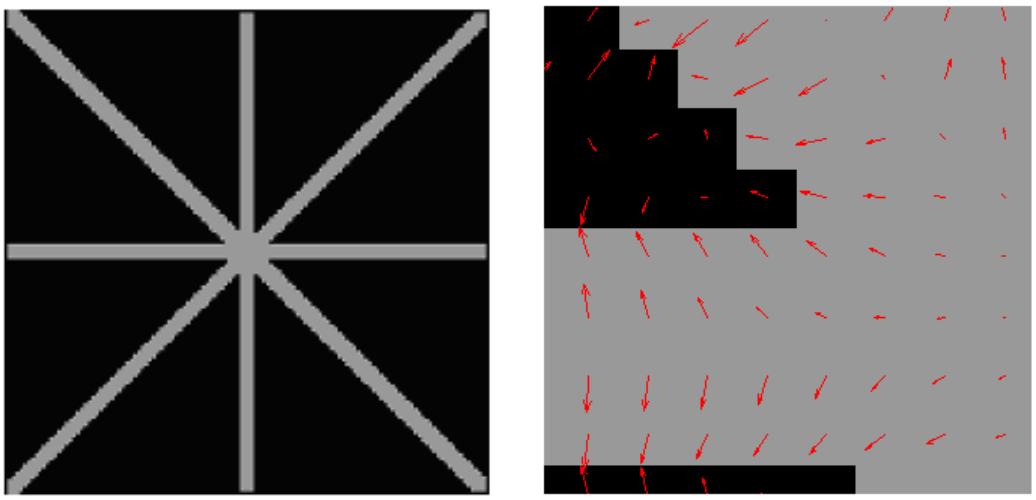

(a) (b)

Figure 3.13: An example of the ineffectiveness of the edge potential force. (a) A geometrically complex shape with a joint at the centre; (b) close-up of the left upper corner of the central joint superposed by the visualised vector field representing the edge potential forces – the length of the arrow is proportional to the corresponding force magnitude. We see that the forces around the upper left corner are small and pointing towards the background (black areas).

pointing to the boundary is correct and meaningful. However, the gradient of edges sometimes gives useless or even incorrect information. The problem seldom occurs in simple shape extraction but occurs often in topologically or geometrically complex cases such as corners or junctions. An example is given by figure 3.13. We can see from figure 3.13b that the edge potential forces will not prevent water from flowing to the black background at the upper left corner of the centre edge joint. Unlike the method used in the Balloon model with an inflation force [25] and the T-snake [31, 32, 70] where the contour evolution will be turned off when the intensity is greater than certain pre-determined thresholds, we propose a pixel-wise regional statistics based image force to handle this problem. The whole image is separated into two regions according to the flowing water – internal/flooded area and external/dry area. The changes of the statistics of both regions resulting from the corresponding flow are considered, respectively. The combination of the two changes can yield a new region-based image force which is given by equation (3.18).

$$F_{S,i} = -\frac{n_{int}}{n_{int}+1}(\mathbf{I}(x_t, y_t) - \mu_{int})^2 + \frac{n_{ext}}{n_{ext}-1}(\mathbf{I}(x_t, y_t) - \mu_{ext})^2 \qquad (3.18)$$

where $F_{S,i}$ is the component of the regional at direction i; subscripts "*int*" and "*ext*" refer to internal and external regions of the water, respectively; μ and n are the mean intensity and number of pixels in the two regions, separately; and **I** is the original image intensity matrix. The definition originates from the Mumford-Shah functional [23, 58], which detects boundaries of interest by minimising the global "fitting" term shown below:

$$V_1(C)+V_2(C)=\int_{inside(C)}|\mathbf{I}(x,y)-\mu_{\text{int}}|^2+\int_{outside(C)}|\mathbf{I}(x,y)-\mu_{ext}|^2 \qquad (3.19)$$

where V_1 and V_2 are the variation terms of the internal/flooded and external/dry regions, respectively; C refers to a closed curve splitting the image into two parts – internal and external regions. If we assume C_0 is the real boundary of the object in the image, then when C fits C_0, the term shall achieve the minimum. So a contour finding process should try to minimize this sum.

Here, instead of globally minimizing this statistic term, we obtain equation (3.18) by considering the change of the total sum given by *single* movement of the water element. If a pixel in the dry area is flooded by the water, the whole flooded region becomes one unit larger and the dry area is now one unit smaller. The sample means of the two regions are also changed and so as the two variation terms in (3.19). Deriving both changes and summing them up thus yields the new pixel-wise regional statistical force functional. The derivation of equation (3.18) is given in Appendix A.

The edge-based potential force can provide a good localisation of the contour near the boundaries (i.e., good detection accuracy) but has a very limited capture range, whilst the region-based forces have a large basin of attraction but are not good at accurate detection. These complementary properties motivate a unification of the two forces. A convex combination method hence is chosen and the combined image force F_i is given by:

$$F_i=\alpha P_i+(1-\alpha)F_{S,i} \qquad (3.20)$$

where all the terms are scalar quantities in direction i, and α ($0\le\alpha\le1$) is determined by

the user to control the balance between them.

3.7 Movement decision

As shown by figure 3.6, the basic iteration process now comes to the final movement decision step, and the sign of the quantity J determines the movement. The considered movement succeeds if $J \geq 0$, and fails otherwise. This is equivalent to comparing the initial kinetic energy with the image resistant work. Only if the initial kinetic energy is large enough to overcome the resistant work, can the contour element of interest reach the target position (the kinetic energy must be positive after passing the first flow decision process).

If $F_i > 0$, it means that the image force in direction i is consistent with the direction and will assist the flow rather than prevent it. Mathematically, the image resistant work defined by equation (3.5) is negative, thus quantity J which is defined as the kinetic energy minus the resistant work must be positive. Consequently, if $F_i < 0$, there is no need to compute J – the movement must be successful. This can improve the computational efficiency of the model implementation.

If, however, $F_i > 0$, we need to calculate J using equations (3.4), (3.5) and (3.6). The terms of these physical equations have all been re-defined in the context of image analogy in previous sections. We will replace these terms by the detailed image analogical definitions and hence arrive at a new expression of J.

First consider the initial kinetic energy in direction i. Equations (3.15) and (3.16) give the analogical definitions of the velocity component in direction i and the flow resistance at the considered contour position (x_c, y_c), respectively. Combining the two equations with equation (3.3) gives:

$$v_i = \frac{F_{D,i}}{Ae^{k\mathbf{E}(x_c, y_c)}} \tag{3.21}$$

Substituting this function of v_i into equation (3.4), we will have the new equation calculating the image analogical kinetic energy term of the considered contour element in direction *i*:

$$E_{Kinetic,i} = \frac{1}{2} m v_i^{\,2} = \frac{1}{2} m \left[\frac{F_{D,i}}{A e^{k \mathbf{E}(x_c, y_c)}} \right]^2 \tag{3.22}$$

We then need to find the image analogical form of resistant work $W_{R,i}$. Substitute the image resistant force F_i given in equation (3.20) and the user-determined flow distance *S* into equation (3.5):

$$W_{R,i} = -F_i S = -[\alpha P_i + (1-\alpha) F_{S,i}] S \tag{3.23}$$

Then substitute equations (3.22) and (3.23) into equation (3.6)

$$J = E_{Kinetic,i} - W_{R\,i,} = \frac{1}{2} m \left[\frac{F_{D,i}}{A e^{k\,\mathbf{E}(x_c, y_c)}} \right]^2 + [\alpha P_i + (1-\alpha) F_{S\,i}] S \tag{3.24}$$

where *m*, *A*, and *S* are defined as constants. Because it is the sign rather than the exact value is of interest, we can set *S* as unity and rewrite the above equation as

$$J = \lambda [F_{D,i} e^{-k\,\mathbf{E}(x_c, y_c)}]^2 + [\alpha P_i + (1-\alpha) F_{S,i}] \tag{3.25}$$

where $\lambda = m / 2A$ and is considered as a regularization parameter chosen by the user to govern the trade-off between the two terms. The value of λ reflects the significance of the water kinetic energy relative to the image force. For example, the detection under severe noise might benefit from a large value of λ as the stronger water force might help to overcome/flood noisy pixels.

The sign of *J* then determines whether the flow to direction *i* from the considered contour position is successful or not. In addition, the flow is set to be a step-by-step process like region growing or greedy snake, and the movement is restricted to be one pixel at most for simplicity. Consequently, even if *J* exceeds zero which means the initial kinetic energy has not been depleted after the one-step-movement, the flow is still terminated. The "residual" velocity will not be brought ahead to the next iteration of the *external* loop defined in Section 3.2. That is, the iterative water flow process is set to be independent of the previous iterations.

3.8 Conclusions

The whole framework of the water flow analogy has been presented, as well as the detailed definitions of the terms in the model.

A matrix combining both water and image edge information is used. The negative gradient of the matrix at the water contour gives the total resultant flow driving force resulting from the water pressure, surface tension and adhesive force. For each contour element, all of its possible flow directions are examined, respectively. The component of flow velocity on each direction is calculated by dividing the related force component by the flow resistance defined by some image information such as edge strengths. If the velocity is greater than zero, the contour element is assumed to be able to flow along the direction with an initial kinetic energy. During this flow process, the image force at the considered direction, which is a combination of edge potential force and regional statistical force, acts upon the flowing element. Here we assume the flow distance S in one flow iteration is fixed. If the image force scalar is positive (consistent with the flow direction), then the water will flow to the target position. Otherwise, the maximum resistant work that the image force can provide is defined as the multiplication of the image force and S. If the initial kinetic energy is greater than the maximum resistant work, the element is able to overcome the resistant force and flow a distance S to the target position in one single iteration. Otherwise, the element is assumed to be dragged back to the origin by the image resistant force at the end of the flow process.

Here the mechanism of the water flow process is similar to region growing, but the model can be implemented in different ways. For instance, the Newton's laws of motion can be applied to find the moving distance of a water contour element with an initial flow velocity under certain image resistant force in a fixed time interval.

Within this new framework, all the terms and factors are adjustable. In this thesis, the

image resistant forces are defined by the combination of edge- and region-based forces, and the adhesive / capillary force is set as a function of edge strengths. These definitions can be altered in accordance with the particular application of the water flow model. For example, when segmenting vessels from retinal images, the matched filter [71] which is specially designed for this application can be combined into the image resistant force or the capillary force. In addition, the water pressure and surface tension can be defined in an alternative way as well. In this chapter, the gradient definition makes the implementation relatively straightforward. However, it does not provide a solid and complete physical basis for the model. For example, if the model is implemented using Newton's laws of motions, there would be water elements stopping between image pixels, which can yield sub-pixel accuracy. Consequently, the distance between adjacent water elements can be arbitrary. In this instance, the gradient based force definition becomes insufficient. Therefore, an alternative method inspired from the paradigm of force field is applied to derive a more flexible and generalised force mechanism.

Chapter 4

Refining the Water Flow Model: Force Field; 3D and Efficiency

4.1 Review of force field analogy techniques

In Chapter 3, the resultant flow driving force is derived from a matrix which combines the water and edge information – the water and contour elements are set to be chosen constants and the value of the non-water pixels equals to the corresponding edge strength. The gradient of this matrix then gives rise to the driving force. In this way, a water element is now effectively a particle exerting attractive forces (surface tension) or repulsive forces (pressure) on other particles, depending on whether or not it is on the contour of the water; the adhesive force is considered to be the attractive forces from the edge points to adjacent water contour elements. However, the gradient framework has limitations and lacks flexibility. As discussed at the end of Section 3.8, if the mechanical structure of fixed-time-interval rather

than fixed-movement-interval is used in the water flow model, the arbitrary distance between elements would bring problems in the gradient based calculations. Even though interpolation techniques can be introduced to handle the problem, the choice of the interpolation methods and the lack of a solid theoretical basis can still make the definitions problematic. Therefore, a more flexible model defining all the force terms is preferred. There have been many image force fields developed for purpose of feature extraction, like the Gradient Vector Flow [22] and the Constant Flow [36]. They have been widely used in active contour methods to drive the evolving contours [72, 73]. However, compared to these mathematical frameworks, an explicit physical model will give the whole physical analogy based method a more consistent theoretical structure, and make it more straightforward to understand.

In addition, there are some presumed properties of the water flow forces that should be satisfied. The strength of the force generated by one water or edge element acting on other elements should be proportional to the assumed mass of the source element and the other element of interest, and be inversely proportional to the distance between the considered two elements. Further, the force direction should point along the line joining the two elements. Those assumptions, together with a natural preference of physical models, make the force field theories in physics [74, 75] and electromagnetism [76, 77] natural choices for the new definitions of flow forces.

In [57], the magnetostatic theory is combined with the active contour model. As shown in figure 4.1a, the current generates magnetic field according to the right hand grip rule. For a moving charge inside a magnetic field, there are magnetic forces introduced by the field acting on it. Further, since currents are essentially sets of moving charges, there are magnetic forces acting on the currents inside magnetic fields as shown in figure 4.1b, where the total force acting on the conductor of length l carrying the current $\mathbf{J}$ in the $\mathbf{B}$ magnetic field is given by the cross product ($l\ \mathbf{J}\times\mathbf{B}$). In [57], the evolving contour and the object boundary are presumed to be charged with electric currents. The object boundary generates a magnetic field and thus exerts

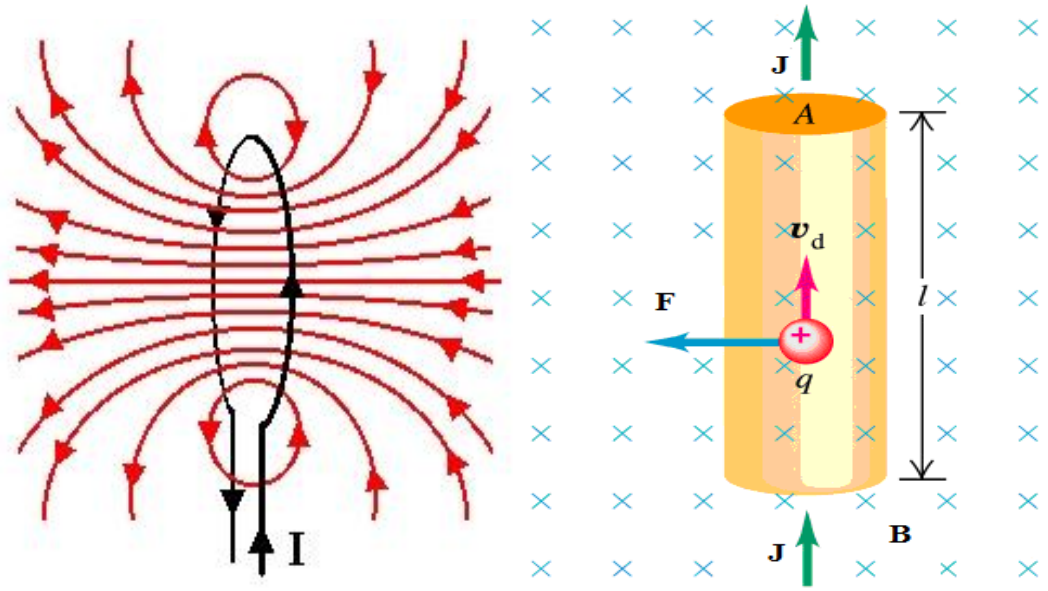

(a) (b)

Figure 4.1: (a) a loop *C* carrying current **I** generates a magnetic field whose direction is determined by the right hand grip rule; (b) magnetic field **B** going perpendicularly into the image plane exerts magnetic forces upon moving charges constituting current **J**. [78]

magnetic forces upon the deformable contour driving it to the boundary position. The Biôt-Savart law defines the magnetic flux density generated by a conductor *C* carrying a current **I** at any pixel with position vector $\mathbf{r}_i$:

$$\mathbf{B}(\mathbf{r}_i) = \frac{\mu_0}{4\pi}\sum_{j\in C} d\mathbf{I}_j \times \frac{\mathbf{r}_j - \mathbf{r}_i}{|\mathbf{r}_j - \mathbf{r}_i|^3} \tag{4.1}$$

where μ_0 is the permeability and $\mathbf{r}_j$ is the position vector of the infinitesimal current vector segment $d\mathbf{I}_j$. The magnetic force at position $\mathbf{r}_i$ is then given by

$$\mathbf{F}(\mathbf{r}_i) = d\mathbf{J}_i \times \mathbf{B}(\mathbf{r}_i) \tag{4.2}$$

where $d\mathbf{J}_i$ is the current vector segment at position $\mathbf{r}_i$. In [57], the current direction is estimated by the signed distance transform, which is also used to initialise level set functions. Therefore, the magnetic force can be easily combined with level sets.

Electrostatic field theory has also been adopted in image segmentation. Jalba et al. [79] presented a charged particle model (CPM) that simulates the particle movements in an electrostatic field. A set of positively charged *free* particles is positioned in the

image analogical field distributed with *fixed* negative charges proportional to the edge strength. Because the free particles have opposite polarity to the fixed charges and the same polarity to each other, there are attractive forces (the Lorentz force) from the fixed charges to the free particles, and repellent forces (the Coulomb force) between the free particles. Coulomb's Law is used to define the electrostatic field. At location $\mathbf{r}_i$, we have

$$\mathbf{E}(\mathbf{r}_i) = \frac{1}{4\pi\varepsilon_0} \sum_{\forall j \neq i, j \in \mathbf{I}} c_j \frac{\mathbf{r}_i - \mathbf{r}_j}{|\mathbf{r}_i - \mathbf{r}_j|^3} \tag{4.3}$$

where c_j is the fixed charge at position $\mathbf{r}_j$, $\mathbf{I}$ is the whole image domain and ε_0 is the permittivity of free space. Thereby, if a free particle e is placed at location $\mathbf{r}_i$, then the electrostatic force imposed on it from c_j's is given by:

$$\mathbf{F}(\mathbf{r}_i) = e\mathbf{E}(\mathbf{r}_i) \tag{4.4}$$

The two equations are used to calculate the forces driving the CPM particle model. In [56], the electrostatics principles are incorporated into the geometric active contour model which can guarantee closed contours.

The definitions of electrostatic and magnetostatic fields both have the same inverse square nature. Consequently, a simplified force field based on the Gauss's Law has been proposed as a generalization of the inverse square law in [80, 81], where the force field analogy is applied in ear recognition. The image pixels are assumed to attract each other according to the product of their intensities and inversely to the square of the distance between them. Each pixel is considered to generate a spherically symmetrical force field so that the resultant force exerted upon a pixel with unit intensity at location $\mathbf{r}_i$ by different pixels is obtained by

$$\mathbf{F}(\mathbf{r}_i) = \sum_{\forall j \neq i, j \in \mathbf{I}} P_j \frac{\mathbf{r}_i - \mathbf{r}_j}{|\mathbf{r}_i - \mathbf{r}_j|^3} \tag{4.5}$$

where P_j is the pixel intensity at location $\mathbf{r}_j$. Calculating the force field over all the image yields a new feature space which reduces the dimensionality of the original pattern space and maintains discriminatory power for feature classification.

4.2 New definition of water flow forces

As discussed in previous section, the physical force field theory gives an alternative definition of the flow forces, which provides the model higher flexibility and a more consistent physical basis.

For simplicity, the generalised Gaussian force field defined by equation (4.5) is adopted. In the new water flow model, both the water elements and the dry image pixels are treated as arrays of mutually attracted or repelled particles acting as the source of Gaussian force fields. Because the dry pixels and other water contour elements exhibit attractive forces on the contour element of interest and equation (4.5) is used, their mass should be negative. Conversely, the internal water elements exerting repellent forces should be of positive mass. Therefore $-\mathbf{G}$ given by equation (3.13) is used to define the mass of each element.

The total force at location $\mathbf{r}_i$ is now given by the summation of the attractive and repellent forces from the surrounding water elements and dry pixels. This is equivalent to convolving $\mathbf{G}$ with the vector kernel, $(\mathbf{r}_i-\mathbf{r}_j)/|\mathbf{r}_i-\mathbf{r}_j|^3$. Because the force strength decreases quickly and drastically with increasing distance from the considered position, it is reasonable to ignore the effects from pixels that are too far away. In other words, the force field does not need to consider all the pixels. In this way, the computational cost can be controlled. Figure 4.2a indicates an example of a 7 by 7 vector force field template, where complex numbers are used to represent vectors.

Vector calculation and normalization is relatively complex. In [80, 81], the scalar potential energy field underlying the vector force field generated by each image pixel is used to simplify the process. The vector force field and the scalar potential energy field are connected by the physical equation:

$$\begin{bmatrix} \frac{+1-i}{18\sqrt{2}} & \frac{+2-3i}{13\sqrt{13}} & \frac{+1-3i}{10\sqrt{10}} & -\frac{i}{9} & -\frac{1+3i}{10\sqrt{10}} & -\frac{2+3i}{13\sqrt{13}} & -\frac{1+i}{18\sqrt{2}} \\ \frac{+3-2i}{13\sqrt{13}} & \frac{+1-i}{8\sqrt{2}} & \frac{+1-2i}{5\sqrt{5}} & -\frac{i}{4} & -\frac{1+2i}{5\sqrt{5}} & -\frac{1+i}{8\sqrt{2}} & -\frac{3+2i}{13\sqrt{13}} \\ \frac{+3-i}{10\sqrt{10}} & \frac{+2-i}{5\sqrt{5}} & \frac{+1-i}{2\sqrt{2}} & -i & -\frac{1+i}{2\sqrt{2}} & -\frac{2+i}{5\sqrt{5}} & -\frac{3+i}{10\sqrt{10}} \\ \frac{1}{9} & \frac{1}{4} & 1 & 0 & -1 & -\frac{1}{4} & -\frac{1}{9} \\ \frac{3+i}{10\sqrt{10}} & \frac{2+i}{5\sqrt{5}} & \frac{1+i}{2\sqrt{2}} & i & \frac{-1+i}{2\sqrt{2}} & \frac{-2+i}{5\sqrt{5}} & \frac{-3+i}{10\sqrt{10}} \\ \frac{3+2i}{13\sqrt{13}} & \frac{1+i}{8\sqrt{2}} & \frac{1+2i}{5\sqrt{5}} & \frac{i}{4} & \frac{-1+2i}{5\sqrt{5}} & \frac{-1+i}{8\sqrt{2}} & \frac{-3+2i}{13\sqrt{13}} \\ -\frac{1+i}{18\sqrt{2}} & -\frac{2+3i}{13\sqrt{13}} & -\frac{1+3i}{10\sqrt{10}} & \frac{i}{9} & \frac{-1+3i}{10\sqrt{10}} & \frac{-2+3i}{13\sqrt{13}} & \frac{-1+i}{18\sqrt{2}} \end{bmatrix} \begin{bmatrix} \frac{1}{3\sqrt{2}} & \frac{1}{\sqrt{13}} & \frac{1}{\sqrt{10}} & \frac{1}{3} & \frac{1}{\sqrt{10}} & \frac{1}{\sqrt{13}} & \frac{1}{3\sqrt{2}} \\ \frac{1}{\sqrt{13}} & \frac{1}{2\sqrt{2}} & \frac{1}{\sqrt{5}} & \frac{1}{2} & \frac{1}{\sqrt{5}} & \frac{1}{2\sqrt{2}} & \frac{1}{\sqrt{13}} \\ \frac{1}{\sqrt{10}} & \frac{1}{\sqrt{5}} & \frac{1}{\sqrt{2}} & 1 & \frac{1}{\sqrt{2}} & \frac{1}{\sqrt{5}} & \frac{1}{\sqrt{10}} \\ \frac{1}{3} & \frac{1}{2} & 1 & 0 & 1 & \frac{1}{2} & \frac{1}{3} \\ -\frac{1}{\sqrt{10}} & -\frac{1}{\sqrt{5}} & \frac{1}{\sqrt{2}} & 1 & \frac{1}{\sqrt{2}} & -\frac{1}{\sqrt{5}} & -\frac{1}{\sqrt{10}} \\ \frac{1}{\sqrt{13}} & \frac{1}{2\sqrt{2}} & \frac{1}{\sqrt{5}} & \frac{1}{2} & \frac{1}{\sqrt{5}} & \frac{1}{2\sqrt{2}} & \frac{1}{\sqrt{13}} \\ \frac{1}{3\sqrt{2}} & \frac{1}{\sqrt{13}} & \frac{1}{\sqrt{10}} & \frac{1}{3} & \frac{1}{\sqrt{10}} & \frac{1}{\sqrt{13}} & \frac{1}{3\sqrt{2}} \end{bmatrix}$$

(a) (b)

Figure 4.2: the 7 by 7 convolution templates for the generation of (a) the vector force field and (b) the underlying scalar potential energy field, respectively.

$$\mathbf{F}(\mathbf{r}_i) = -\nabla \xi(\mathbf{r}_i) \tag{4.6}$$

where ξ is the potential energy related to the force and $\mathbf{r}_i$ still stands for an arbitrary location. Each pixel is assumed to generate a spherically symmetrical potential energy field, and the field intensity at location $\mathbf{r}_i$ generated by an image pixel P_j at location $\mathbf{r}_j$ is calculated by

$$\xi_j(\mathbf{r}_i) = P_j \frac{1}{|\mathbf{r}_j - \mathbf{r}_i|} \tag{4.7}$$

It is the same as the energy imparted to a unit pixel at the location $\mathbf{r}_i$. The defining equation is simpler but the underlying concept is less intuitive. Assume a unit test particle moves around in the force field generated by P_j. Energy will be exchanged if the net effect of the movement is to change the distance between the test pixel and P_j. Therefore, in the image domain, the energy field consists of concentric rings of equal potential energy named as equipotentials [80]. The scalar potential energy at the same equipotential ring will be the same. Figure 4.3 shows the potential energy function of a single pixel of unit intensity.

For a particular position $\mathbf{r}_i$, the total potential energy field intensity is given by the superposition of the energy field intensities generated by all the other image pixels:

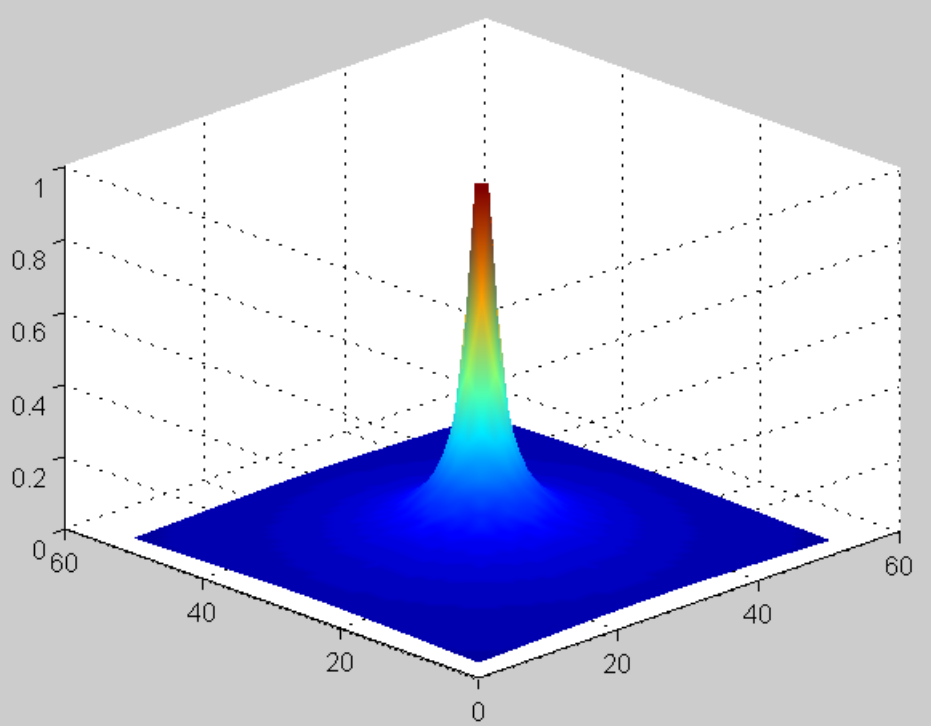

Figure 4.3: a part of the potential energy field generated by a single isolated image pixel with unit intensity.

$$\boldsymbol{\varepsilon}(\mathbf{r}_i) = \sum_{j \neq i} \boldsymbol{\xi}_j(\mathbf{r}_i) = \sum_{j \neq i} P_j \frac{1}{|\mathbf{r}_j - \mathbf{r}_i|} \tag{4.8}$$

In effect, this is to smooth the image with a 1/r kernel. Fig 4.2b shows the 7 by 7 scalar potential energy field generation template. Again, in the water flow model, the matrix **G** combining both the image edge and the flowing water information rather the original image is used to define the mass values. Denoting the energy convolution kernel as **K**, the corresponding flow driving force vector field is then given by the negative gradient of the convolution result:

$$\mathbf{F}_D = -\nabla(\mathbf{K} * (-\mathbf{G})) = \nabla(\mathbf{K} * \mathbf{G}) \tag{4.9}$$

Compared to equation (3.14), the previous defining equation of the driving force, we can see that the new defining equation under the force field framework is effectively the same as the gradient based definition except that now an additional smoothing step is imposed upon the matrix **G** before calculating the gradient. Further, as shown in figure 4.2b, the smoothing kernel is similar to a distance weighted averaging

kernel [2]. Therefore, the new force field based water flow model is expected to have improved immunity to noise, especially to the Gaussian noise.

It must be highlighted that the new force field based definition is not consistent with the true physical principles underlying the water flow process and electromagnetism. This new framework is purely conceptual, not physical. The flexibility and simplicity of the force field framework with the simplified inverse square law form are why it has been chosen to define the water flow force terms.

4.3 Three dimensional water flow model

The extension of the water flow model to 3-D is very straightforward and natural because the physical water flow process is three dimensional itself.

Firstly, some preliminary image analogy assumptions need to be clarified. Now the water is assumed to flow inside volume images which are 3-D matrices. Still, we can assume that one voxel of the volume matrix represents one basic water element, and define the water elements adjacent to dry areas as surface water elements under certain connectivity (26-connectivity is chosen in this thesis). The surface water elements can move to flood adjacent dry regions and thus only these elements are of interest.

The general principle of the volume image water flow is of the analogous fashion to the 2-D case. The surface water element achieves an initial kinetic energy due to the flow driving force and the resistance. The resistant force derived from the volume image is then exerted upon the moving element. The surface element will flow to the considered dry position if the initial kinetic energy overcomes the image resistance.

The implementation process is exactly the same as the flowchart given by figure 3.6. The difference is that now the factors discussed above need to be extended to 3-D

$$
\begin{array}{lccc}
z = 1 & \begin{pmatrix} -1 & 0 & +1 \\ -2 & 0 & +2 \\ -1 & 0 & +1 \end{pmatrix} & \begin{pmatrix} -1 & -2 & -1 \\ 0 & 0 & 0 \\ +1 & +2 & +1 \end{pmatrix} & \begin{pmatrix} +1 & +2 & +1 \\ +2 & +4 & +2 \\ +1 & +2 & +1 \end{pmatrix} \\
z = 2 & \begin{pmatrix} -2 & 0 & +2 \\ -4 & 0 & +4 \\ -2 & 0 & +2 \end{pmatrix} & \begin{pmatrix} -2 & -4 & -2 \\ 0 & 0 & 0 \\ +2 & +4 & +2 \end{pmatrix} & \begin{pmatrix} 0 & 0 & 0 \\ 0 & 0 & 0 \\ 0 & 0 & 0 \end{pmatrix} \\
z = 3 & \begin{pmatrix} -1 & 0 & +1 \\ -2 & 0 & +2 \\ -1 & 0 & +1 \end{pmatrix} & \begin{pmatrix} -1 & -2 & -1 \\ 0 & 0 & 0 \\ +1 & +2 & +1 \end{pmatrix} & \begin{pmatrix} -1 & -2 & -1 \\ -2 & -4 & -2 \\ -1 & -2 & -1 \end{pmatrix} \\
 & (a) & (b) & (c)
\end{array}
$$

Figure 4.4: The 3-directional gradient operators. (a), (b), and (c) are x-, y-, and z-directional operators, respectively. They are all 3-D matrices and thus are presented as three 2-D matrices, separately.

domain. Equation (4.7) is again used to calculate the energy field given that the position vectors and the field template **K** are now defined in 3-D space. Equation (4.9) is also incorporated in the 3-D flow model. The gradient operator ∇ is now applied to the volume matrix **G** which combines the information of both the volume image edges and 3-D flowing water. To obtain volume image edges, a 3-D edge/gradient operator is required. Here a 3 directional Sobel edge detector is defined and applied. Figure 4.4 shows each of the 3 components of the gradient operator.

After calculating the resultant driving force in 3-D domain, the corresponding flow resistance is then required. The definition is also unchanged, and remains a function of the volume image edge strengths.

For image forces, simply defining the image force functions given by equations (3.17), (3.18) and hence (3.20) in $\Omega \subset \mathbf{R}^3$, the same equations then can be used to calculate the volume force functionals. At the end, the same movement decision processor comparing the volume image resistant work and the initial kinetic energy is then used to determine the flow in the 3-D space.

4.4 Water freezing system

Though the implementation of 3-D water flow model is straightforward, the higher dimensionality increases the computational cost dramatically because now it is the flowing water surface rather than the contour that is being evolved. The number of the water surface elements considered in one iterative loop is much larger than that of the contour elements. Methods of improving the implementation efficiency are thus desirable.

A water "freezing" system is incorporated to reduce the computational cost. Water surface elements are assigned an additional attribute "temperature" which is determined by the number of flow steps the considered element has remained as a surface element. Denoting this number of steps as N_S, the temperature attribute T_{Water} is then defined by equation (4.10).

$$T_{Water} = T_{Initial} - N_S \tag{4.10}$$

where $T_{Initial}$ is the user-set initial temperature level. The water temperature decreases when N_S increases and hence provides a measure of the active degree of surface elements. If the temperature of a surface element falls below the "freezing" point (i.e., 0 degree), then the element will be removed from the computational process and its position will be saved. By applying this mechanism, the 3-D water flow model achieves a conservative and adjustable computational cost.

Although motivated by the high computational burden of water flow based volume image segmentation, the water freezing system is also a useful and powerful instrument in the 2-D case. It is useful in many image segmentation applications. For example, when detecting tube-like features like vessels using the water flow model, in most time only a small proportion of the water is flowing.

4.5 Conclusions

Force field theories are now embodied into the water flow model to accrue the benefits of local force mechanism and curve evolution. Previous works based on physical force field analogy are reviewed and a generalised form of inverse square laws given by equation (4.5) is used to define the water flow forces.

The essential principles underlying the water flow model remains unchanged. The resultant driving force is still derived from the combination of water pressure, surface tension and adhesion. The difference is that now the generalised inverse square law in physics is adopted to define all the force terms. This makes the water flow model more flexible and understandable. The theoretical basis of the new model is more consistent as well. The new model can be easily adjusted to convolution masks of larger size or different shape (like circular templates).

The extension to 3-D water flow model is straightforward since the real physical water flow process is three dimensional. However, the higher dimensionality increases the computational burden heavily. A water freezing system is thus incorporated into the flow model. A new attribute of the surface elements, temperature, is introduced. The attribute is set to be proportional to the activity / movement of the surface element as shown in equation (4.10). If the temperature falls below a user-set level, the corresponding surface element is considered as 'frozen' element and will be removed from the subsequent computations in order to reduce the total computational cost. This water freezing system provides an adjustable efficiency-controlling-facility and is also useful in 2-D applications.

Chapter 5

Using Water Flow for Complex Shape Segmentation

As shown before, the proposed image segmentation technique retains the major attributes of physical water including the fluidity, surface tension, and adhesion. Therefore, the simplified analogical water flow process is expected to be adaptable to topological and geometrical changes, whilst preserving a relatively smooth contour and the ability to bridge small gaps and flow into narrow braches. In addition, the force field method used to derive the resultant water flow forces enhances the immunity of the analogical model to image noises. To verify those properties, the model (force field based by default) is applied to segment objects with topologically and/or geometrically complex structures. The experiments have been conducted upon both synthetic and natural images, with and without noise.

5.1 Surface tension and adhesion

First of all, the effectiveness of surface tension and adhesion are examined, as well as the goodness of analogy to water flow. Figure 5.1 illustrates water flowing in a cube-

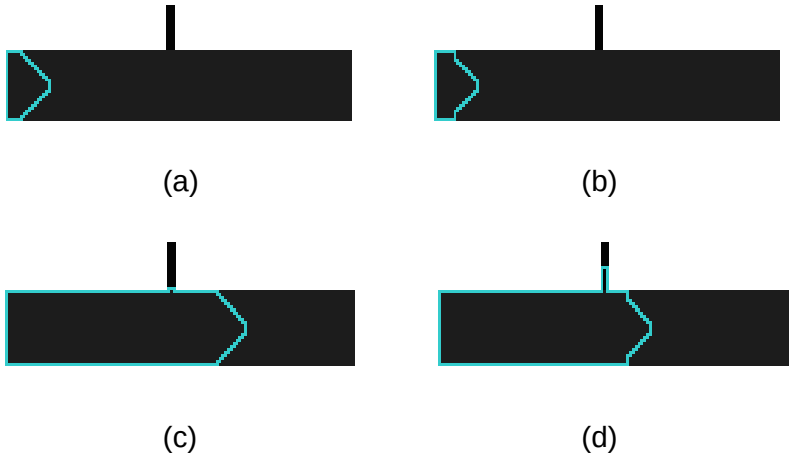

Figure 5.1: Water flow inside a cube with a very narrow branch (a) and (c) without adhesive force; (b) and (d) with adhesion.

like object with and without an adhesive force which is the result of attractive forces from edges adjacent to the flowing water contour. The evolution is initialized at the left end of the pipe. We can see the water stops at the interior side of the edge lines, and the water front forms a shape which is similar to that observed on naturally flowing water. Figures 5.1a and 5.1b have slightly different frontal shapes due to the effects of adhesion. Besides making the water near edges flow "faster", adhesion also helps flow into narrow branches, as indicated in figure 5.1d. Without the adhesive force, the surface tension will bridge the entrance of the very narrow branch, as shown in figure 5.1c. The results justify the effectiveness of the surface tension and the adhesion.

5.2 Smoothly varying boundary detection

The adhesive force can help in detection of the most "appropriate" object boundary position. Figure 5.2a shows a circularly symmetric object with smoothly changing edges. Figure 5.2b gives the edge energy, which equals one minus the edge magnitude, along a radius from the centre of the circle. The test image has been designed so that the illumination decreases gradually from the centre to the image borders. The sharpest change of illumination occurs at the boundary of the object, leading to the strongest edge response. We are aiming to find this boundary which

also has the globally minimum energy functional. However, the local minima might "trap" water elements before they arrive at the global minimum and thus yield inaccurate results. The adhesive force makes the water able to flow "inside" edges. That is, even if a water element has come onto an edge point, the adjacent edges can still "attract" it, so it continues to move. Therefore, problems associated with local minima can be reduced. Figures 5.2c and 5.2d indicate the segmentation results both with and without the adhesive force, using the same parameters. We can see that the

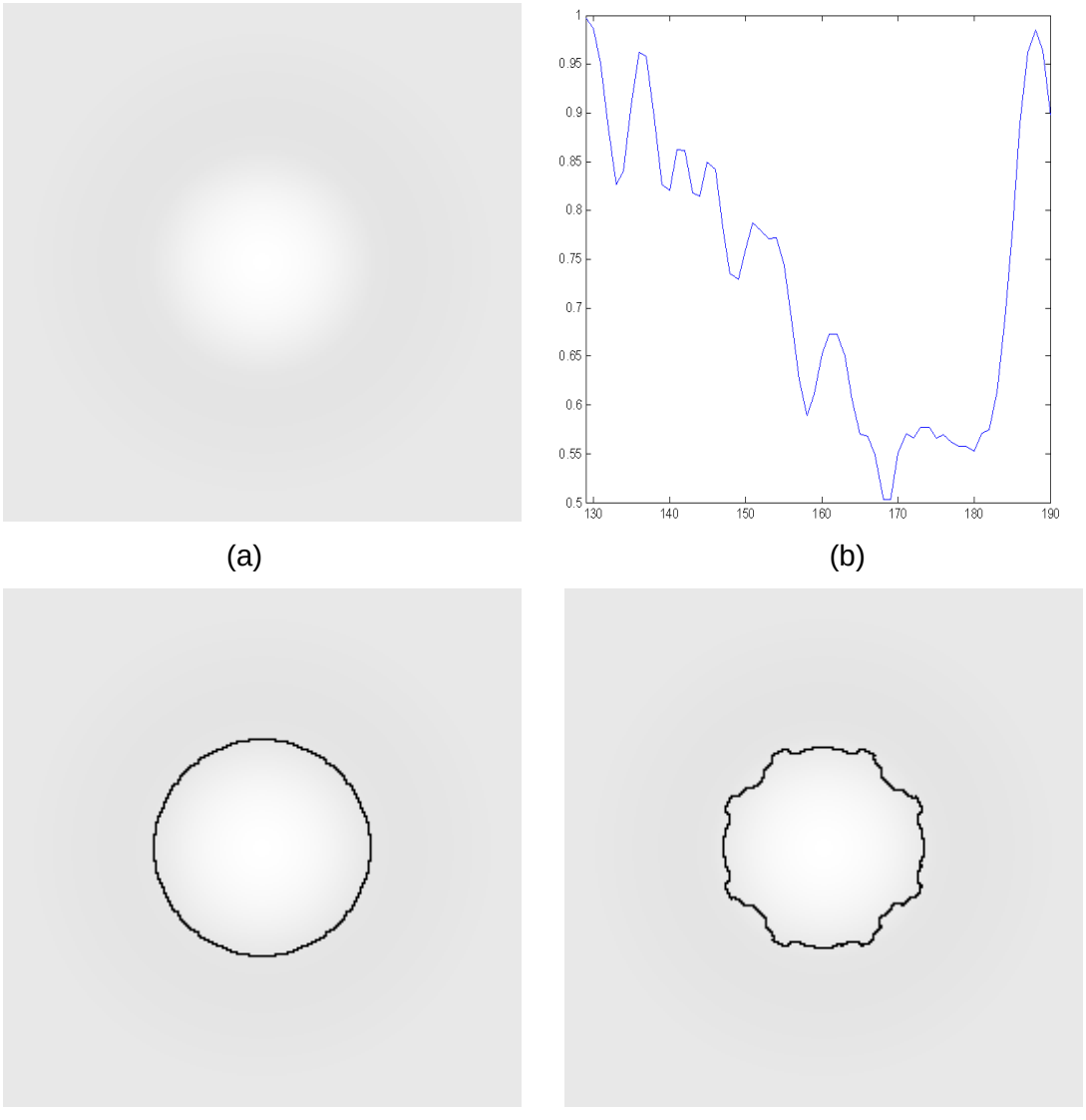

Figure 5.2: (a) Object with weak-contrasted boundary; (b) energy distribution along a radial from the centre of the circle (129,129) to position (190, 129), and the radius of the circle is set as 40 pixels; (c) segmentation results by water flow model with adhesive force and (d) without adhesive force. (λ=1, α=0.5, k=5)

adhesive force helps to achieve a more accurate result. It should be pointed out that the region-based image force in this example is not significant because of the gradually changing regional intensities. The segmentation results are acceptable for $0.5 \leq \alpha \leq 1$ with the same k and λ ($k = 5$, $\lambda = 1$).

5.3 Geometrical flexibility

The water flow model successfully imitates the essential properties of physical water flow, among which the fluidity enables the operator to segment and reconstruct tubular objects and objects with bifurcations or significant protrusions. In particular, the water pressure, adhesion and regional image force make the model much less sensitive to its initial position and geometry than the parametric snakes. A point water source can be placed anywhere inside or outside the target object or a large water body can be initialised around the object. Figure 5.3 shows a segmentation example where the water initialised within the structure (of complex geometry) and flowed into all the branches. The final water contour segments the object well.

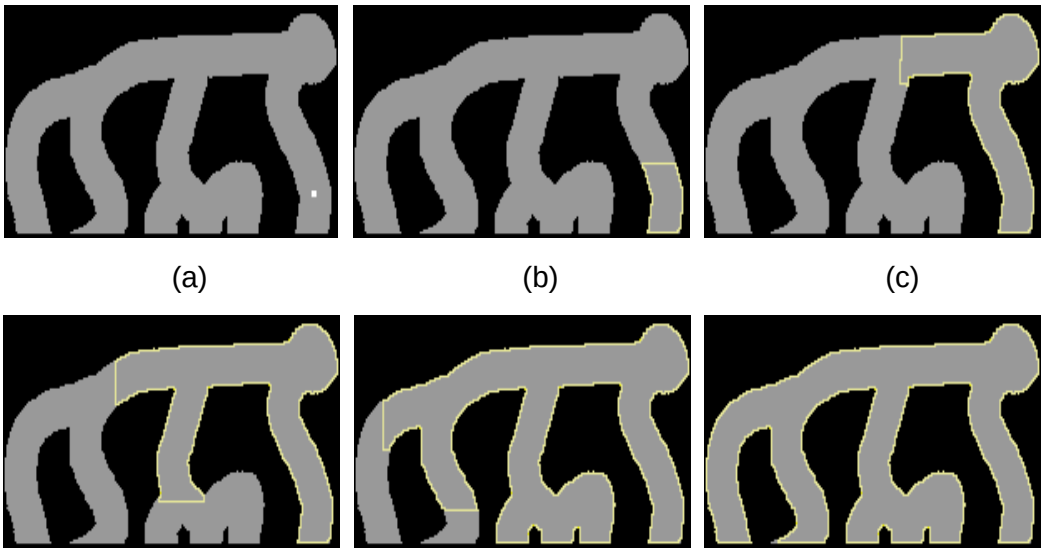

Figure 5.3: Segmentation of an object with complex geometry. The image sequence indicates a water flowing and branching along the object. (λ=1, α=0.5, k=5)

5.4 Topological adaptability

Topological transformations are often necessary in real image analysis applications. As described in Chapter 3, the water flow model can merge and adapt to the topology of the target object(s). Figure 5.4 shows an example of multiple object detection. The water is initialised around the 3 objects, and then flows inwards. At the end, the whole image is flooded except the objects with resistance to water, and the final static water contour gives the shape information of all the 3 objects. Note that the helical tube has boundary concavities and is also a geometrically complex structure. Good immunity to noise is also shown as the test image is contaminated by 10% Gaussian noise.

In natural image analysis, the object of interest often has both complex topology and geometry. Automating the adaptation to both the topology and geometry of the target object is thus highly desirable. Furthermore, limitations of imaging techniques often introduce problems with image quality, like the illumination inhomogeneity and noise. To further evaluate the performance of the water flow model under such circumstances, an artificial test image is generated. The 512×512 image has been designed to meet some necessary requirements: (a) horizontal, vertical and diagonal branches are included; (b) narrow and wide branches are presented, respectively; (c) there is a circular pipe so that we get a curve with smoothly changing curvature; (d) each half of the object has a different intensity so that weak edges now exist between the two regions – this is an example of the illumination inhomogeneity problem. In addition to those properties, Gaussian and impulsive noise are also added to the test image respectively, so that the noise robustness can also be assessed. Figure 5.5 indicates the test image with Gaussian and impulsive (salt and pepper) noise.

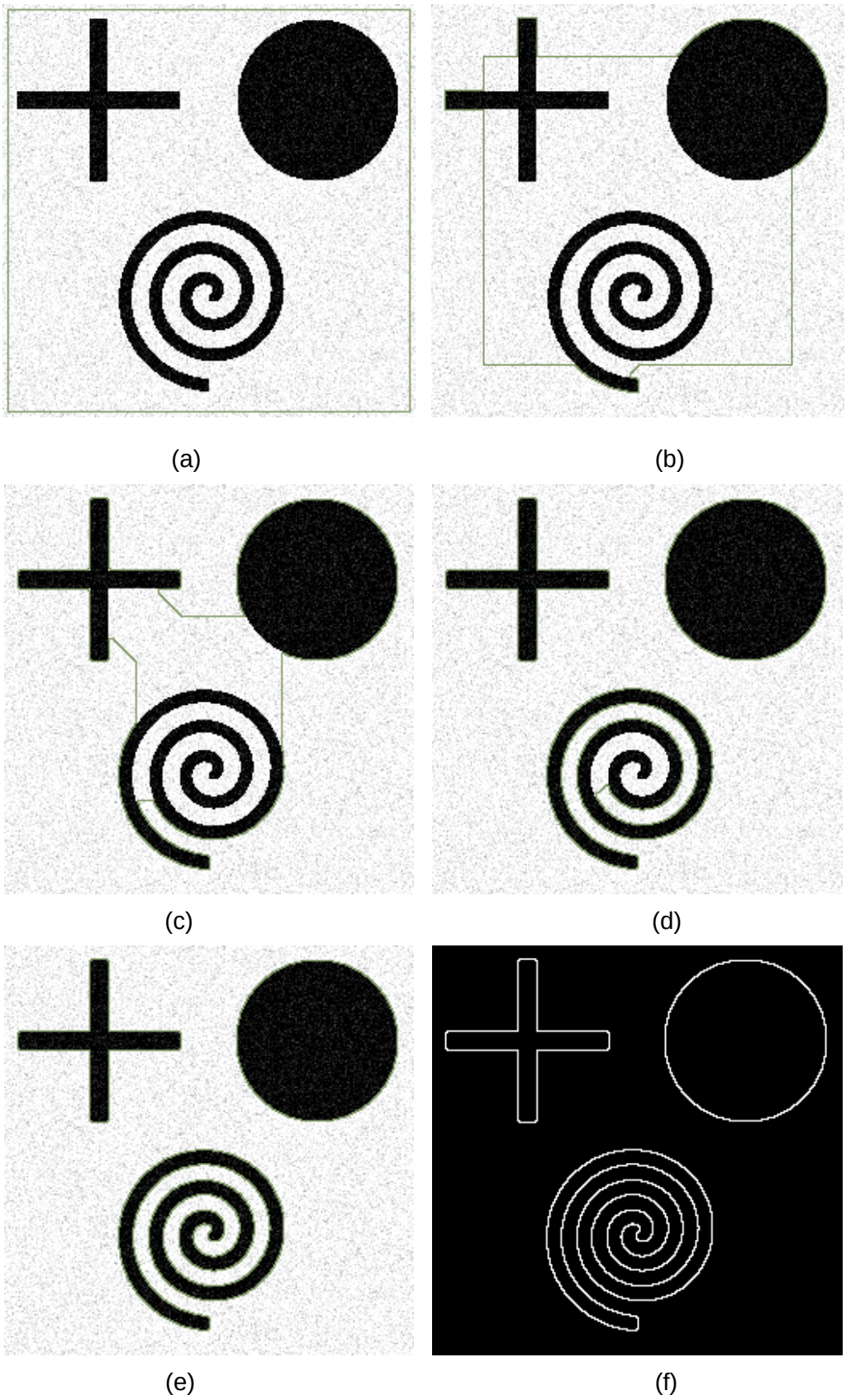

(a) (b)

(c) (d)

(e) (f)

Figure 5.4: multiple objects detection with 10% Gaussian noise corrupted, where (a) is the initialization. (b)–(e) show the process, and (f) is the final extracted contour. (λ=1, α=0.5, k=5)

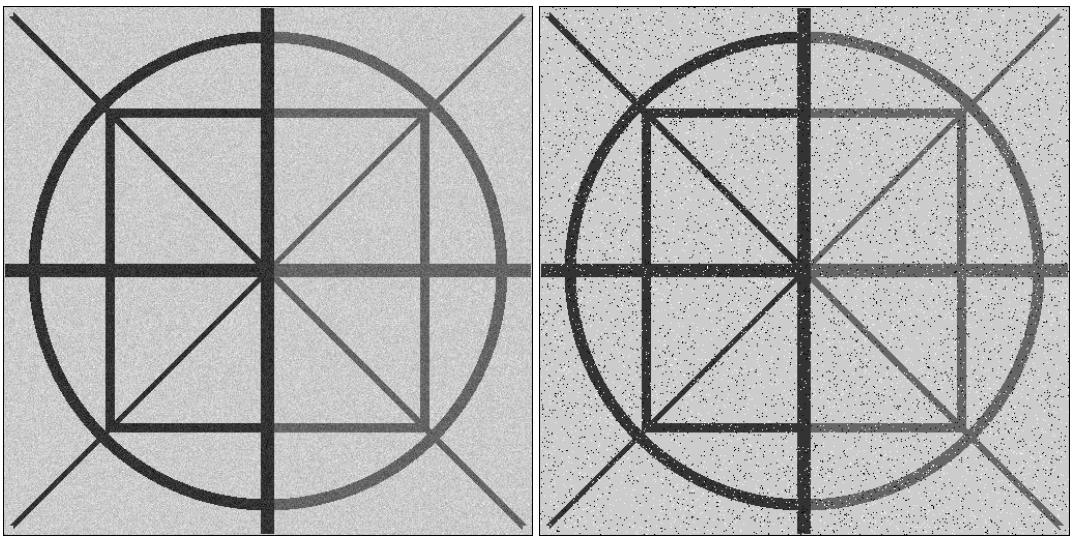

(a) (b)

Figure 5.5: the synthetic test image corrupted with (a) 10% Gaussian noise and (b) 5% Impulsive noise.

Due to the closed areas formed by the object, an initialization inside the target is preferred, but the position is not significant. The results are the same whatever the initialization position is, given it is inside the object. Figure 5.6 shows the progress of segmentation and we can see that the water can self-merge to adapt to the different topology of the object. Also, both the complex geometry and the inhomogeneous illumination problems are handled well.

As discussed in Section 4.2, the matrix **G** combining the edge and flowing water information is effectively smoothed by the energy field kernel that is similar to a Gaussian filter, and then the gradient of **G** is used as the water flow driving force. Therefore, the whole model should exhibit strong immunity to Gaussian noise. This has been justified by examples in figure 5.4 and 5.6. Another important kind of noise, impulsive noise, is also tested here. This kind of noise is very difficult for many active contour approaches to deal with because the noisy edge response is usually very strong. However, as shown in figure 5.7, this is not such a difficult task for the new technique. The noise points inside the object are almost all flooded and only those connected with the real target object boundaries make the result less accurate.

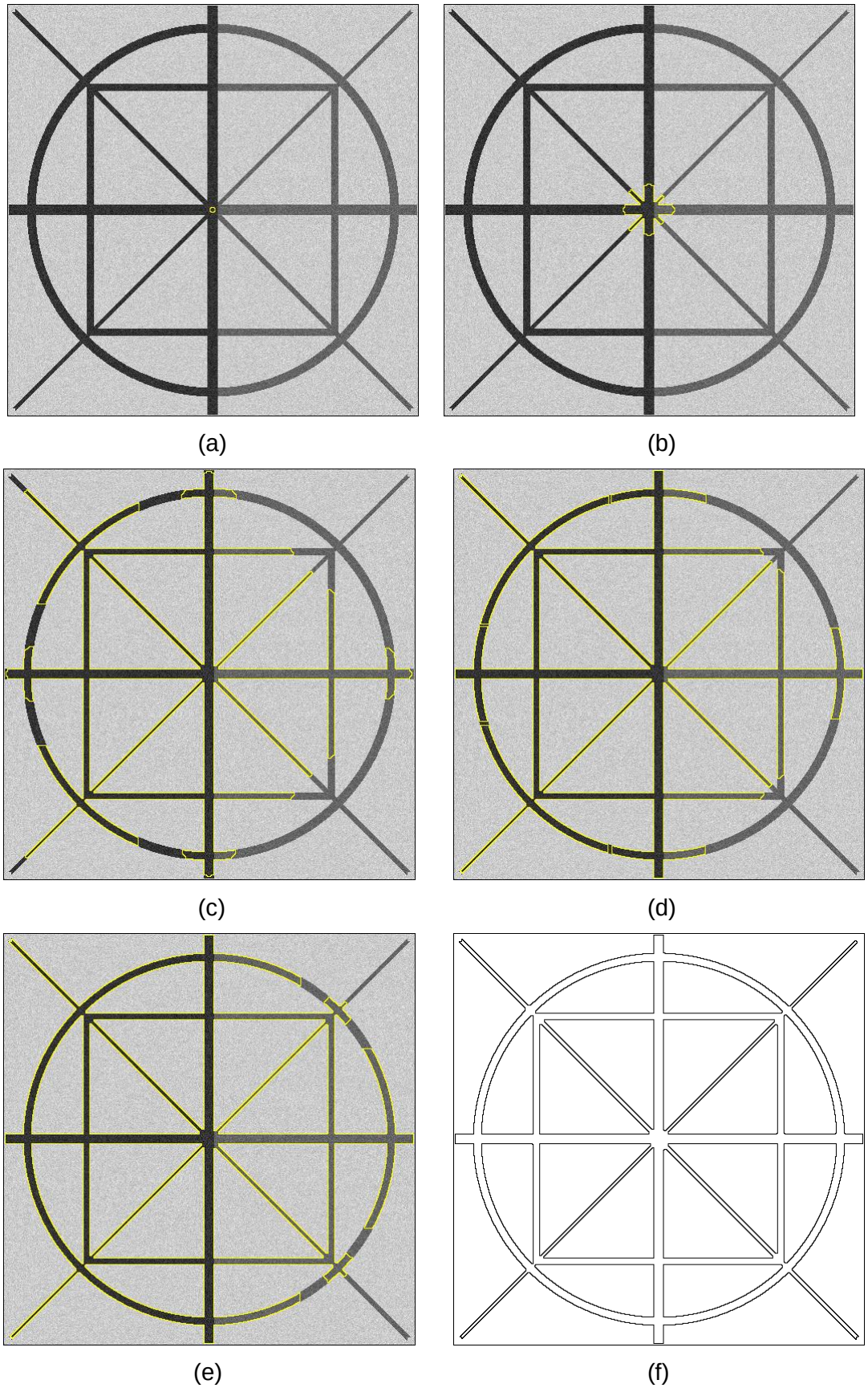

(a) (b)

(c) (d)

(e) (f)

Figure 5.6: Flow process for image of figure 5.5a; (a) initialized at centre; (b) flow to branches with different widths and directions; (c)-(e) examples of self-merging; (f) final extracted contour. (λ=1, α=0.5, k=5)

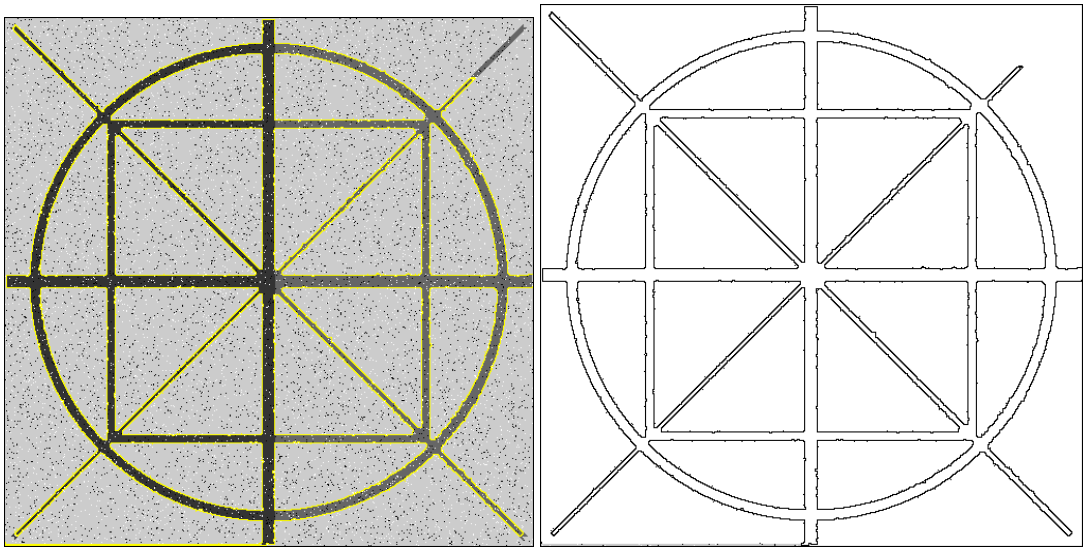

(a) (b)

Figure 5.7: The segmentation result for the test image contaminated by the 5% Impulsive noise. (λ=1, α=0.5, k=5)

Here the most significant influence of the noise is the incomplete detection of the thinnest diagonal branch in the top right corner. The robustness to impulsive noise arises from the fluidity and the adhesion: water surrounds the small impulsive noise clusters (1 or several pixels), and the adhesive force given by the noise edge response attracts the water to flow inside the noise area. Thereby, unless the cluster of noise is too large, the noise pixels will be flooded and hence exert insignificant / no negative influence to the segmentation.

The result shown in figure 5.7, as stated above, is incomplete since there is a gap formed by noise points in the upper right of the thinnest diagonal branch. In processing natural images, this kind of gap will exist and makes the contour extraction terminate early. The merging ability of the new method, however, makes it possible to overcome the problem. In this simple case, as shown in figure 5.8a, an additional water source is initialized inside the undetected area. It then fills the region and merges with the "main" part. Therefore a complete detection can be achieved. This is an example where multiple water flows are necessary because part

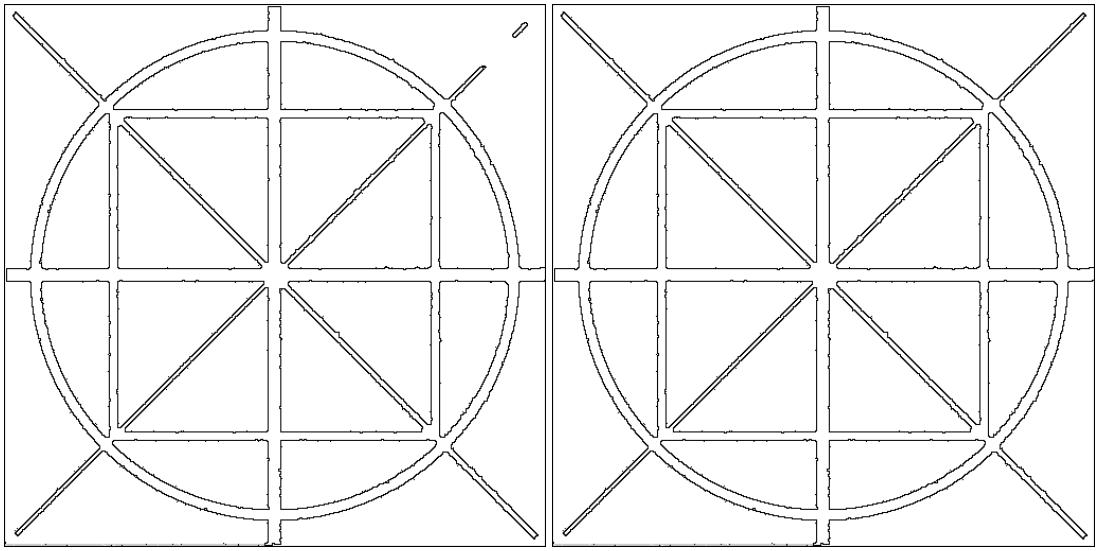

(a) (b)

Figure 5.8: A better result for impulsive noisy image which is achieved by adding one more water source – multiple water flows. (λ=1, α=0.5, k=5)

of the target object is blocked by strong noisy edges. Multiple water flows approach also provides a solution to improve image segmentation efficiency by simulating multiple water flows concurrently on different CPUs.

5.5 Topology preserving constraint

In the previous section, we have shown the topological adaptability of the water flow technique. This property is desirable in many practical applications. Nevertheless, it is not always required. In particular, if a specific object is sought and its topology has been known, then the segmentation method should be chosen in a way that the correct topology can be achieved / preserved. Figure 5.9 shows such an example where the original water flow method cannot retain the correct topology. The water is initialised inside the hand-shape object with a circular shape. During the flow process, the water merged where the two middle fingers touch each other and hence changed its original topology.

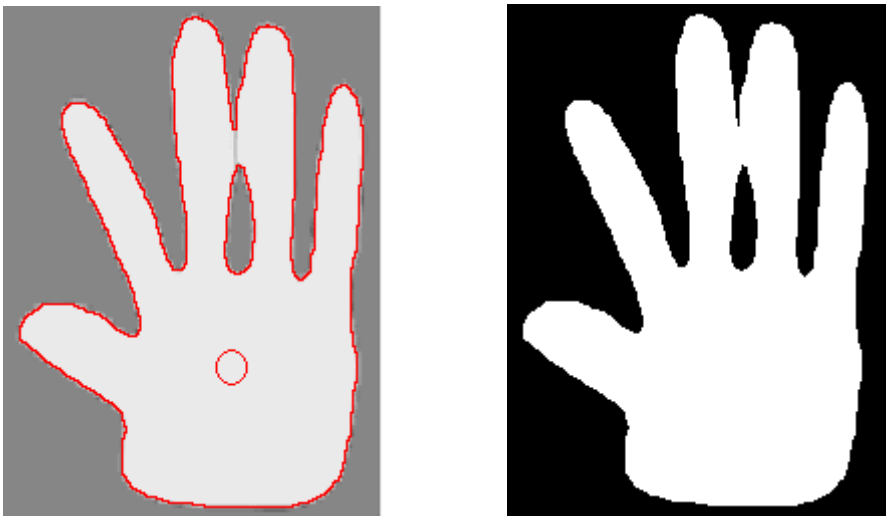

(a) (b)

Figure 5.9: Segmentation of a hand phantom by water flow analogy. (a) the initialisation and final water contour; (b) the final static water.

Han et al [82] introduced a topology preserving level set method to ensure that the topology of the final contour is the same as that of the initial one. The underlying principle is simple – the implicit contour represented by the zero level set function can pass an image pixel only if the considered pixel is a *simple point*, a concept from digital topology theory [83, 84]. The concept is explained in detail in Appendix B.

Here the simple point criterion is also used to define the topology preserving constraint. Only if the dry image pixel is a simple point, can the water flood the point. The implementation of this constraint is again quite straightforward because the water flow approach is a physical model with explicit contour.

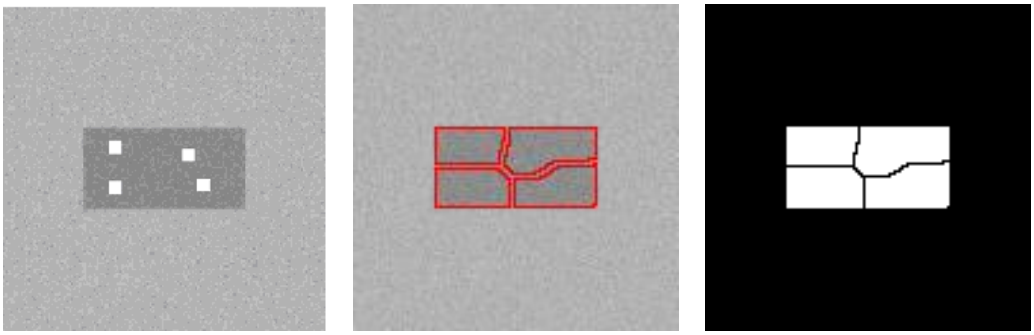

(a) (b) (c)

Figure 5.10: (a) the 4 different initialisation positions inside the rectangle; (b) the final water contours and, (c) the final water.

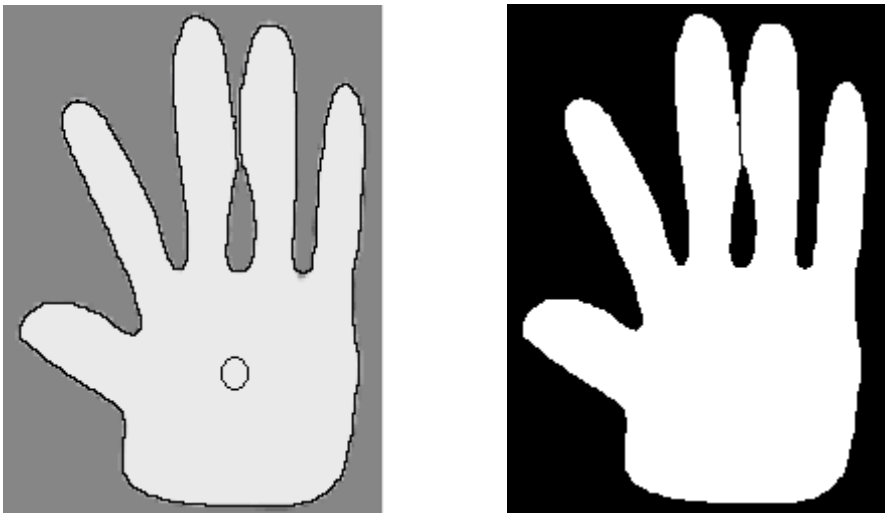

(a) (b)

Figure 5.11: Segmentation of the hand phantom by WFTP. (a) The initialisation and final contour; (b) the final water.

Figure 5.10 illustrates the effectiveness of the water flow model with topology preserving constraint (WFTP). The water is initialised at 4 different positions inside the box (target object). Because of the topology preserving constraint, the four pieces of flowing water cannot merge with each other and thus preserved their respective topology. We then applied the WFTP to the hand phantom image shown in figure 5.9, and the result is illustrated in figure 5.10. As we can see, the WFTP retains the boundary of each of the two middle figure separated and thus reflects the correct shape / topology of a hand.

5.6 Quantitative assessment of noise robustness

In Section 5.4, the immunity to noise of the force field based water flow model has been tested qualitatively. To achieve a more accurate measure of the noise robustness, a quantitative performance evaluation is carried out. The test image is generated artificially so that the ground truth can be compared. Figure 5.12 shows the original image and the ground truth boundary. We can see that a narrow boundary concavity is deliberately included in the shape to increase the segmentation difficulty.

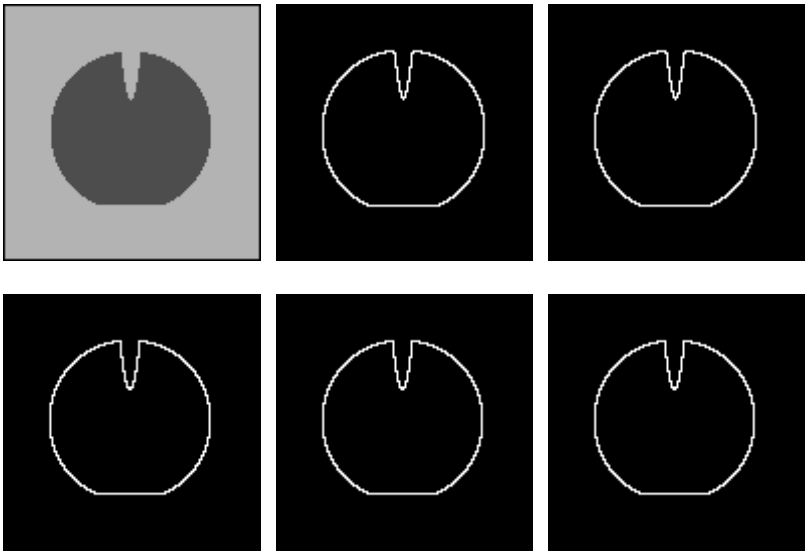

Figure 5.12. Top row: the test image, the ground truth boundary, and the result for the noise-free image using force field water flow; 2nd row: results for the original basic water flow, the region based active contour, and the GVF snake.

As discussed in chapter 4, force field based water flow model is expected to exhibit stronger noise robustness compared to the basic water flow method, because of the additional averaging smoothing filter. This judgement is justified here by comparing the performance of the two water flow models. In addition, two classic active contour based techniques, Chan and Vese's region based level set approach [23] and the GVF snake [22, 29], are also used for comparison.

In the assessment, the parameters of the two water flow models are set as λ=1, α=0.5, and k=5, which are chosen empirically. For Chan and Vese's region based active contour, as shown in chapter 2, the method is based on the minimisation of an extended Mumford-Shah functional and the equation has been re-written below:

$$\begin{aligned} E(C) = {} & \gamma \cdot \mathrm{Length}(C) + \nu \cdot \mathrm{Area}(inside(C)) \\ & + \beta_1 \int_{inside(C)} |\, \mathbf{I}(x,y) - \mu_{\mathrm{int}} \,|^2 dxdy \\ & + \beta_2 \int_{outside(C)} |\, \mathbf{I}(x,y) - \mu_{ext} \,|^2 dxdy \end{aligned} \tag{5.1}$$

where **I** is the image matrix, C is the implicit contour defined by the level set

function, and μ_{int} and μ_{ext} are the mean values of the areas inside and outside C, respectively. Here the parameters are chosen as follows: $\beta_1=\beta_2=1$, $v=0$, $\gamma=0.2\times255^2$. The first 3 parameter values are the same as those proposed in [23, 85]. The length/scaling parameter γ is set to be large because we are aiming to detect only one large object and ignore all the points due to noise. Because of the averaging nature of the energy functional, this region-based method is relatively robust to noise which has been shown in [23]. Also note that the level set representation has been implemented using the narrow band method to improve the computational efficiency. For the GVF snake, which is based on the gradient vector flow field $\boldsymbol{v}(x,y) = [u(x,y), v(x,y)]$ minimising the energy functional

$$E = \iint [\mu(u_x^2 + u_y^2 + v_x^2 + v_y^2) + |\nabla f|^2 |\boldsymbol{v} - \nabla f|^2] dxdy \tag{5.2}$$

where f is the edge map of the image and μ is the regularisation parameter that should be set higher when noise level is higher. Here we have chosen different values of μ to achieve optimum performance. The GVF field is derived iteratively and the number of iterations was chosen as $\sqrt{N}$ where N is the number of image pixels. A parametric active contour with balloon force is then deformed in this gradient vector flow field where the tension parameter α=0.6, the rigidity parameter β=0 as in [22, 29].

All the four approaches can segment the object perfectly when the image is not corrupted by noise, as shown in figure 5.12. The two typical varieties of noise, Gaussian and impulsive noise are selected to contaminate the image. The mean square error (MSE) is used to measure the performance under noise.

$$MSE = \sum_{k=1}^{I_D} d_k^{\,2} \Big/ \max(n_D, n_I) \tag{5.3}$$

where n_I and n_D are the number of ideal and detected contour points respectively and d_k is the distance between the kth detected contour point and the nearest ideal point.

The quantitative results are shown by figures 5.13a and 5.13f. We can see that the performance under noise of the force field based water flow model is markedly better

than that of the basic model, which justifies the expectation that the force field refinement made to the water flow model can improve the performance in particular the noise robustness. In addition, the force field based water flow outperforms both the region based active contour and the GVF snake, especially when the noise contamination is severe (SNR < 10dB). The performance advantage of the force field based method to the other operators is further illustrated qualitatively by examples of the segmentation results, as shown by figure 5.13 (b)-(e) and (g)-(j). It should be noted that because the level set approach is based on regional information only and is topologically free, it generated many separated small contours under impulsive noise even with a high γ. However, these over-segmented contours can be easily removed according to their size information because we are aiming to segment one big object. Here we have applied this post-processing to the region-based active contour model's segmentation results.

In terms of the computational performance, for the 128×128 noise free test image, the computational times for the different approaches based on a 2.4 GHz Windows XP PC running Matlab were as follows: 21s for Chan and Vese's method, 12s for the basic water flow model, 12s for the GVF snake, and 10s for the force field based water flow. All the methods were initialised as a small circle at the centre of the segmented object.

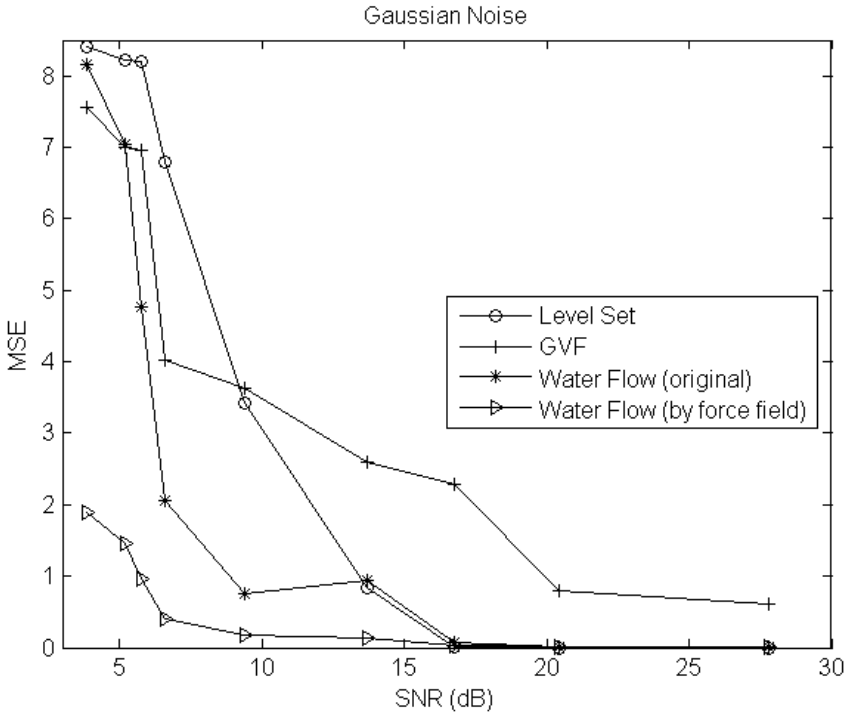

(a) Gaussian Noise

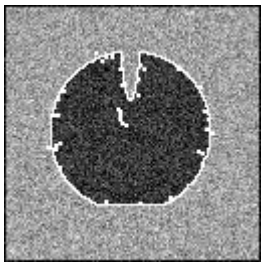

(b) Region based level set (MSE=0.83)

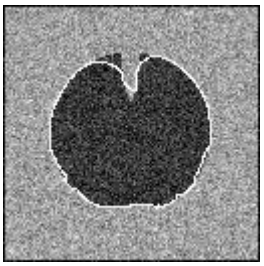

(c) GVF snake (MSE=2.60)

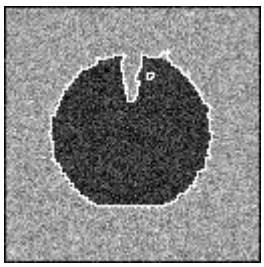

(d) Basic water flow (MSE=0.89)

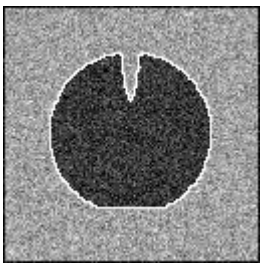

(e) FF water flow (MSE=0.13)

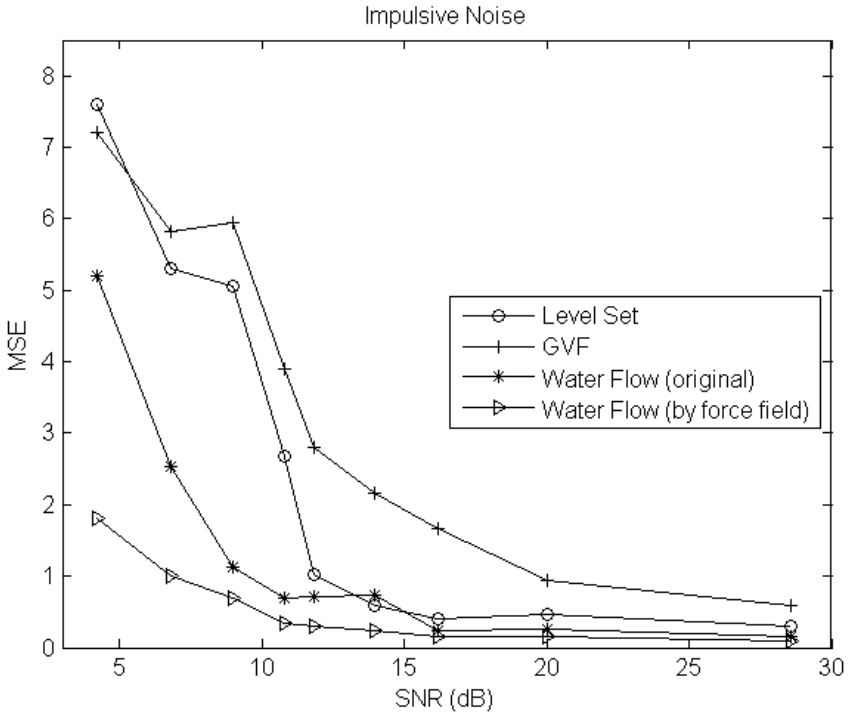

(f) Impulsive Noise

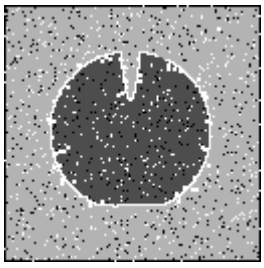

(g) Region based level set (MSE=1.02)

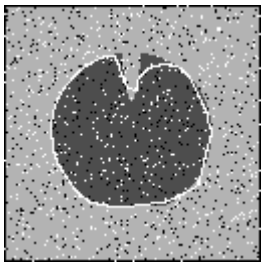

(h) GVF snake (MSE=2.79)

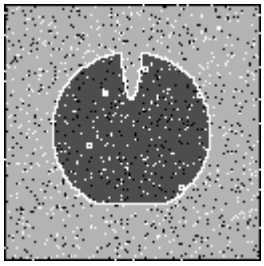

(i) Basic water flow (MSE=0.71)

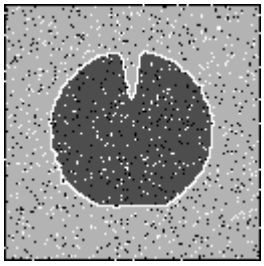

(j) FF water flow (MSE=0.31)

Figure 5.13: (a) and (f) are the Mean Square Error (MSE) results for all the four operators under impulsive and Gaussian noise respectively; (b) to (e) are detection results under Gaussian noise (SNR = 13.69); (g) to (j) are detection results under Impulsive noise (SNR = 11.81).

5.7 Segmentation on natural images

So far, the new technique has been proved as topologically adaptable, geometrically flexible, and robust to noise by experiments based on synthetic images. Now the algorithm is applied on natural images to segment objects with complex structure.

The first example is vessel segmentation on digital fundus photos. This kind of pictures is acquired by digital camera and is stored in JPEG format. They have some common problems, like noise, uneven brightness and contrast (the closer to the centre, the better the quality, and vice versa), and features with very low contrast or inhomogeneous intensity. Therefore, vessel segmentation in such retinal images is of great difficulty. Image enhancement techniques are often used to improve the image quality but the process also increases the noise level. However, the water flow has been proved to be relatively immune to noise and the simple histogram equalization is applied ahead of the contour evolution. Figure 5.14 indicates an example. We can see that the features are more distinctive and the noise at the background is enhanced as well. One point we need to mention is that the green channel of the colour retinal image is chosen for vessel segmentation here as this channel of colour fundus photos formatted as an RGB image contains the highest contrast between vessels and background [71, 86, 87].

(a) (b)

Figure 5.14: Retinal image pre-processing (a) the green channel of the original image and (b) the image after the histogram equalization.

We then apply the water flow based segmentation approach to the enhanced retinal image. The water flow is initialized at a point inside a vessel branch and ended at stasis. Figure 5.15 shows the vessel segmentation process. We can see that the new technique can handle problems like complex topological changes and noise interruption existing in natural images of limited quality. Furthermore, the segmentation yields relatively accurate contour shape information, which is superior to methods based on region information only.

The detection is incomplete as shown in figure 5.15d. Some of the vessels are not detected. The failure is due to the initialization restriction (vessels without existing connection to the detected "vessel system" will certainly be missed), or the gaps in the branches. Some of the gaps are formed naturally and are meaningful as the ones formed by intersection of two vessels. The other gaps result from factors as the camera, lighting, and noise etc. To handle these problems, multi-source initialization and a post-process of gap linking would be appropriate. To show this possibility, two new water "sources" have been added as indicated by figure 5.15e, and the final result is shown in figure 5.15f. The water from the upper source merged with the old result which gives a more complete result. However, the lower one stops at gaps. In that case, the further processing like gap-linking techniques should be appropriate and certain improvement of the detection quality can be expected.

A fundamental advantage of physical models is that the parameter selection is easier to be interpreted. The parameters often have analogical physical explanations. In the water flow model, the higher λ should lead to stronger water driving forces, and a higher k should make the flow resistance more sensitive to edge strengths. The only major parameter that does not have physical explanations is α which simply regulates the balance between region- and edge-based image resistant forces. Therefore, all the three key parameters can be fully interpreted and the potential effect of changing these parameters can be easily estimated – this makes the parameter selection more explicit and intuitive. We will show this by an example given by figure 5.16.

(a)

(b)

(c)

(d)

(e)

(f)

Figure 5.15: Vessel segmentation by water flow analogy where α=0.5, λ=1, *k=30*: (a) – (d) flow from one branch to all the other connected vessels; (e) two new water sources and (f) the final result.

Figure 5.16 shows the segmentation result for the image of a river delta with different parameters, where the river is the target object. It is suited to performance evaluation since gaps and "weak" edges exist in the image. One example is the upper part of the river, where boundaries are blurred and irregular. There are also inhomogeneous areas inside the river, which are small islands and have lower intensity. Our water flow operator can overcome these problems. As shown in figure 16a, a reasonably accurate and detailed contour of the river is detected. At the upper area, the very weak boundaries are also detected. This is achieved by using high value of k that gives the operator a high sensitivity to edge response. The contour is relatively smooth by virtue of surface tension. The fluidity leading to topological adaptability is shown well by successful flow to the branches at the lower area. Most of them are detected except failure at several narrow branches. The barriers are caused either by natural irregularities inside them or noise.

By changing the parameters, as expected, some alternative results can be achieved. For example, figure 5.16b shows a segmentation of the whole basin of the river. It is analogy to a flood from the river. The water floods the original channels and stops at the relatively high regions. This shows the effect of changing the physical parameters. The regulation parameter α does not exert significant influence in this case.

Chan and Vese's region-based level set approach has also been applied to this image for comparison, as shown by figure 5.17. As discussed in section 5.6, the parameter γ exerts most significant influence to the segmentation results – if γ is small, the level set operator will detect as many details as possible; if γ is larger, the smaller points will not be detected and instead more general shape of the objects of interest will be segmented. Figure 5.17a shows the result with small γ, where all the narrow branches of the river have been detected, as well many unwanted small shapes. The result in the upper area of the river is also corrupted by the over-segmentation. In figure 5.17b, we can see that a very large γ detects the general shape of the river basin and reduces the over-segmentation problem significantly (though still more severe than the water flow result in figure 5.16b). Nevertheless, the left upper part of the river basin is not detected by the level set operator.

We also ran the GVF snake on this test image. As shown by figure 5.18a, the GVF snake fails in the detection task as the contour evolution terminates early. It is because the active contour cannot propagate where the vector flows are tangent to the contour or diverge within the neighbourhood and the saddle points in the GVF field formed within the homogeneous areas of the river delta. An improved result can be achieved by adding the balloon force to the GVF snake model so that the contour can still deform when the force is tangent to the curve. However, the problems arising from straddle points and geometrical complexities (e.g., the branches) make the GVF model converge early and thus cannot provide a satisfactory segmentation, as shown in figure 5.18b.

The computational advantage of the water flow model compared to the region-based level set approach is clear in this detection task. The running times for the narrow band level set approach with different γ were 453 minutes (γ=0.01×255^2) and 291 minutes (γ=0.2×255^2). The long run times are mainly due to the complex and small features present in the image that make the convergence process very difficult and slow. The small time step size determined by the CFL (Courant-Friedrichs-Levy) condition guaranteeing the convergence of the level set method also contributes to the long running times. In comparison, the running times for the water flow model were 13 minutes (α=0.5, λ=1, k=30) and 21 minutes (α=0.5, λ=3, k=0), respectively.

(a) α=0.5, λ=1, *k=30*

(b) α=0.5, λ=3, *k*=0

Figure 5.16: Segmentation results for river delta image with different water flow parameters: increased λ increases the water flow driving force and thus effectively reduces the significance of image forces, and smaller *k* makes flow less sensitive to edges, therefore the detail detection level is lower in (b).

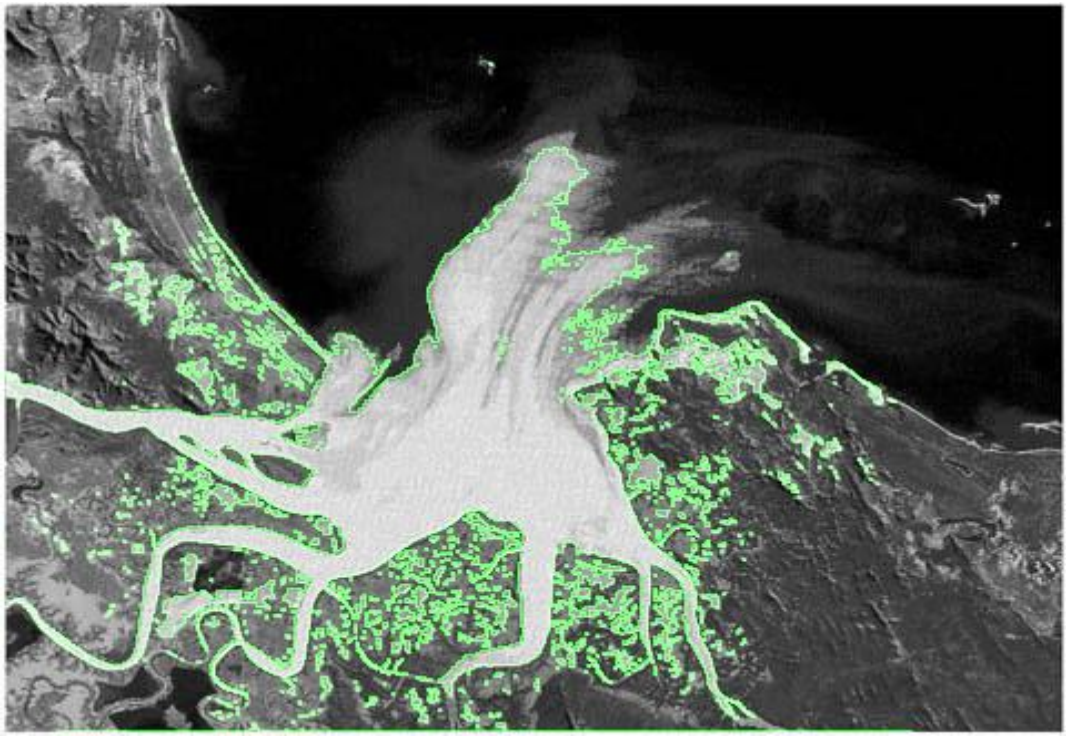

(a) $\beta_1=\beta_2=1$, $\nu=0$, $\gamma=0.01\times255^2$

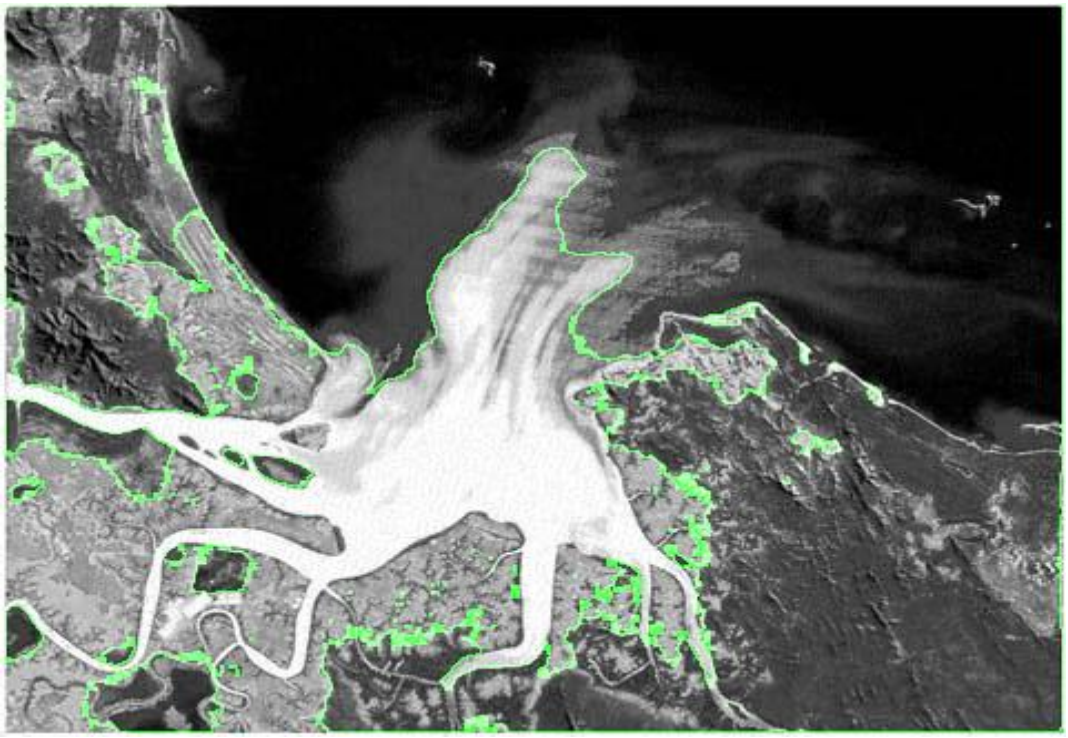

(b) $\beta_1=\beta_2=1$, $\nu=0$, $\gamma=0.2\times255^2$

Figure 5.17: Segmentation results of the region-based level set method on the river delta image with different parameters: a) when γ is small, the method will detect as many objects as possible and of any size; b) when γ is large, smaller objects will not be detected and instead the general shape of the whole basin of the river has been segmented.

(a) α=0.6, β=0

(b) α=0.6, β=0, p=0.5

Figure 5.18: Segmentation results for the river delta image using (a) the GVF snake and, (b) the GVF snake with balloon force (where p is the parameter controlling the balloon/pressure force term)

5.8 Water freezing system

As described in Section 4.4, the water freezing system freezes the water contour elements that keep inactive for a user-set period by removing them from the computational process and saving the position information in a table. Therefore, only part of the whole water contour is flowing in one iterative step. Figure 5.19 illustrates the freezing process where the initial temperature $T_{Initial}$ is set to 5. That is, if a contour element keeps still in 5 iterative steps, it will be set as frozen and removed from the computation process. The darker portions of the flowing water front are the active parts and the others are frozen contour elements. In addition, the graph in figure 5.20a compares the number of active contour elements (N_A) and that of the whole contour during the flow process (N_T), and figure 5.20b shows the percentage of N_A in N_T. We can see that after 40 flowing steps, the percentage falls to about 10% which means a 90% improvement in efficiency. The freezing facility is most useful in segmenting tube-like features and in volume image segmentation.

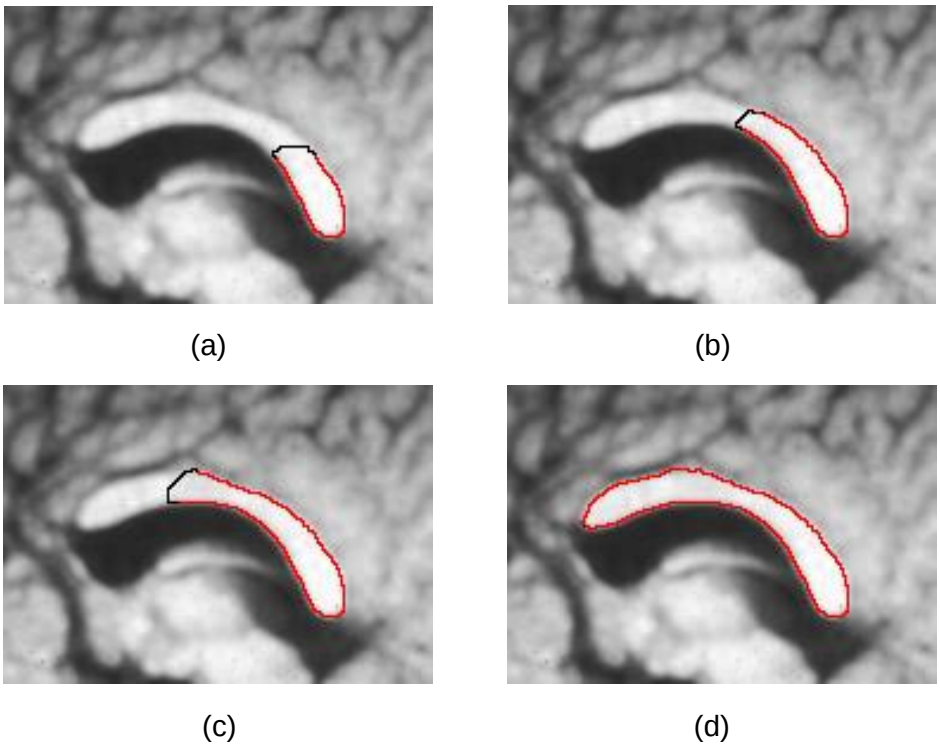

(a) (b)

(c) (d)

Figure 5.19: Segmentation of the corpus callosum incorporating the water freezing facility. The dark lines stand for active portions of the flowing water front (α=0.5, λ=1, *k*=5).

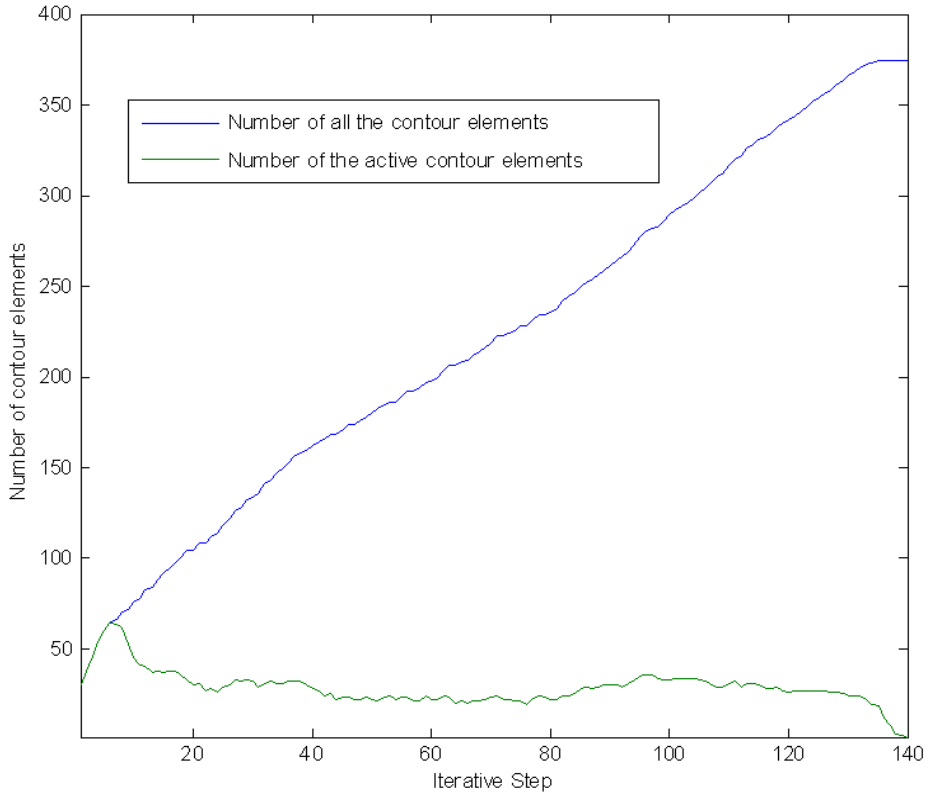

(a)

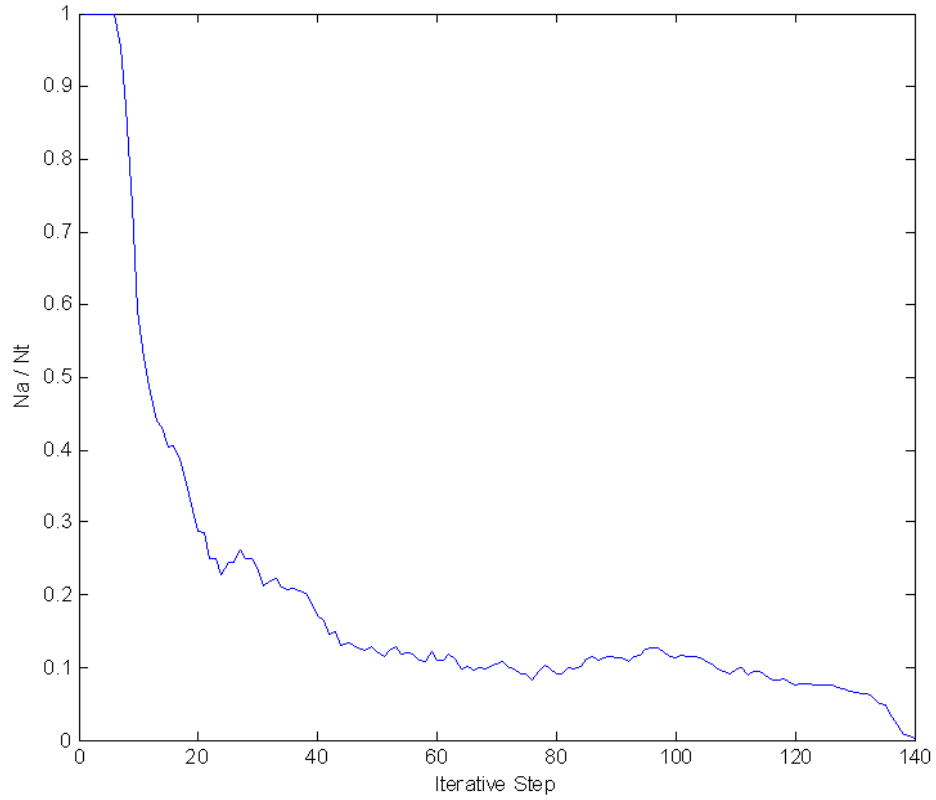

(b)

Figure 5.20: (a) the plots of the number of active elements and the number of all the elements against the iterative step. (b) the proportion of N_A in N_T.

5.9 Higher dimensions

As described in Section 4.3, the 3-D water flow model is analogous to the 2-D version, and thus the desirable properties such as the topological and geometrical flexibility should have been retained.

We first tested the 3-D water flow model in a synthetic image. The target object belongs to the family of Metaspheres, the generation method of which can be found in [22]. The flow process is shown in figure 5.21 where the image volumes are visualised by iso-surface method. Then the water flow method is applied on a 3-D volume image of a real engine. The 3-D water flow is initialised inside the engine and we can see from figure 5.22 that the topology of the water has been changed, as well as the geometry.

The example results here justify the effectiveness of the 3-D water flow model. In practice, the volume segmentation techniques are most useful in solving medical volume image segmentation problems. The corresponding experiments have been carried out and the results are discussed in Chapter 6.

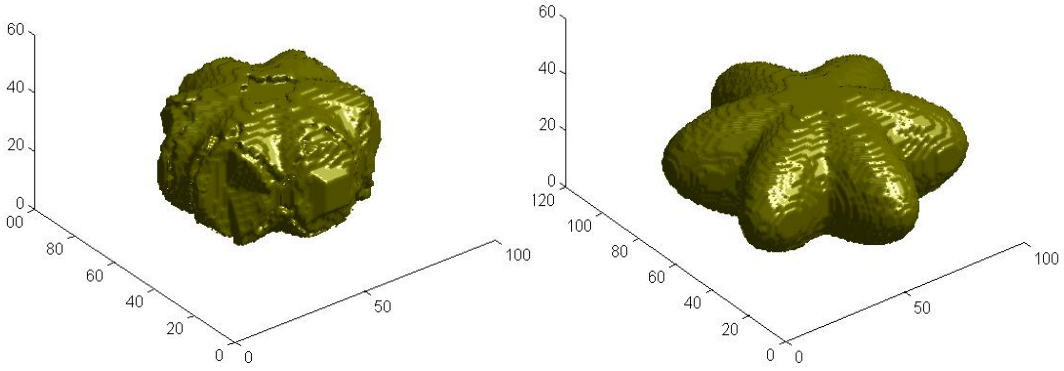

(a) (b)

Figure 5.21: Segmentation of a meta-sphere by the 3-D water flow analogy. (a)-(b) the flowing water surface; (c) the final result. (α=0.5, λ=1, *k*=5).

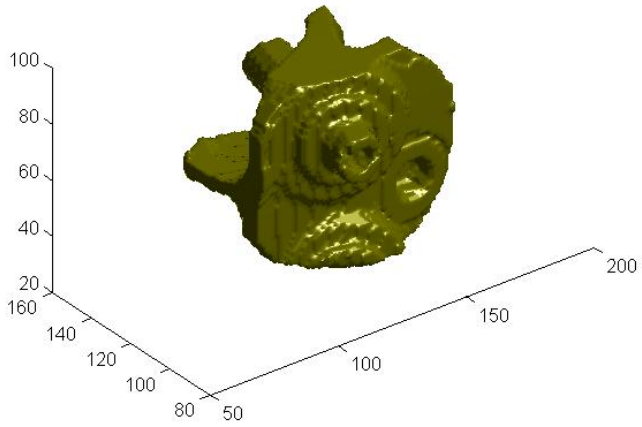

(a)

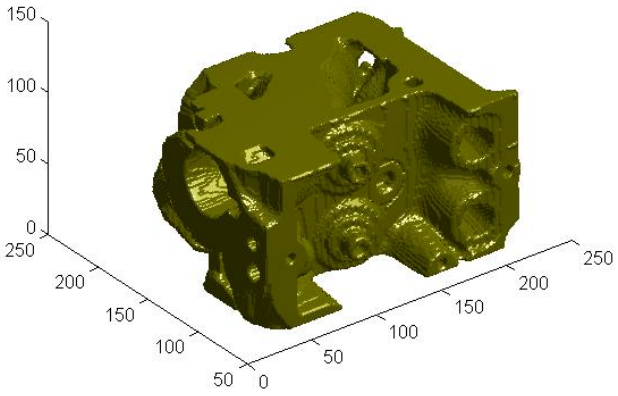

(b)

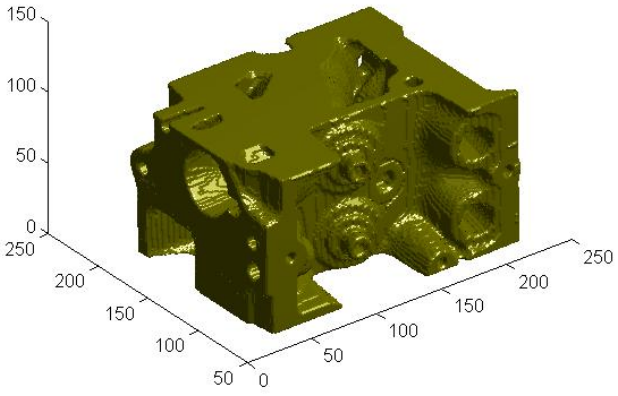

(c)

Figure 5.22: Segmentation of an engine from a CT scanned volume image. (a) the flowing 3D water; (b) (α=0.5, λ=1, *k*=5).

5.10 Conclusions

Quantitative and qualitative experiments have been performed on synthetic as well as real images. The topological adaptability and the geometrical flexibility of the model are justified. By adopting an explicit topology preserving constraint, the model can also retain its original topology. In addition, the proposed approach is shown to be able to segment shapes with weak contrast to their background.

The immunity to noise of the new techniques has been assessed where the Chan and Vese's operator [22] is implemented as comparison. The new model is shown to provide superior performance to Chan and Vese's operator under influence of noise.

As a physical analogy, the parameters of the water flow model are straightforward and intuitive to interpret and hence to select. An example showing the effect of parameter changes is also given, where we illustrate that either the general structure or the details of the target object can be segmented by the water flow model with proper parameter settings.

The efficiency issue is also discussed. The proposed solution to reduce the computational burden, the water freezing system, is proved to be effective especially when segmenting tube-like shapes. At the end of the chapter, the experimental results of 3D water flow model on synthetic volume images and a real CT scanned volume image are presented.

Chapter 6

Medical Image and Volume Segmentation

6.1 Introduction

Segmenting anatomical structures from medical images is a fundamental step in analysing medical data. For example, the retina vessel structures can provide useful information like vessel width, tortuosity and abnormal branching which are helpful in diagnoses. Manual delineation of the structures is ineffective and inefficient especially when the number of images is large. Therefore, automatic analysis is needed. However, the complexity and variability of the anatomical features, together with the imperfections of typical medical images such as intensity inhomogeneities and imaging noise which cause the boundaries of structures of interest discontinuous or indistinct, make the automatic segmentation very challenging.

In Chapter 5, the proposed water flow model has been shown to be effective in segmenting objects with complex shapes. Further, the ability of detecting weak /

smooth boundaries and the strong immunity to noise make the technique suitable for medical image analysis. In this chapter, the performance of the water flow model in medical image segmentation is evaluated, both qualitatively and quantitatively.

6.2 MR images

Automatic segmentation of Magnetic Resonance (MR) images, especially the brain MR images, has recently received much attention due to the improved fidelity and resolution of the MR imaging system [88 89 90]. In Chapter 5, we have shown the result of segmenting the corpus callosum in a sagittal brain MR image in figure 5.18. In this section, further applications of the water flow operator on MR images are presented. The water sources are all set inside the object of interest and the parameters are chosen as α=0.5, λ=1 and k=10. The results produced by Chan and Vese's region- based active contour [23] are also given for comparison, where the parameters are set as: $\beta_1=\beta_2=1$, $\nu=0$, and $\gamma=0.2*255^2$.

The segmentation is generally the first stage of higher level medical image analysis tasks like registration, labelling, and shape analysis. These applications usually require the target anatomic structures to be reduced to compact and analytic shape representations, which are naturally the qualitative criteria of the result assessment.

Figure 6.1 shows the segmentation of the brain shape in a sagittal MR image. The level set method produced small holes inside the main brain structure and some extra objects are detected as well. This can be improved by only retaining the longest continuous contour. In comparison, the water flow model produces a single, compact result with relatively smooth contour. One point that should be noted is that the water stopped at the interface between the brain and the spine even though the contrast is weak. This is because of the high sensitivity of the flow resistance to edge strengths, and the surface tension from the adjacent water contour elements stopping at boundaries with stronger contrast.

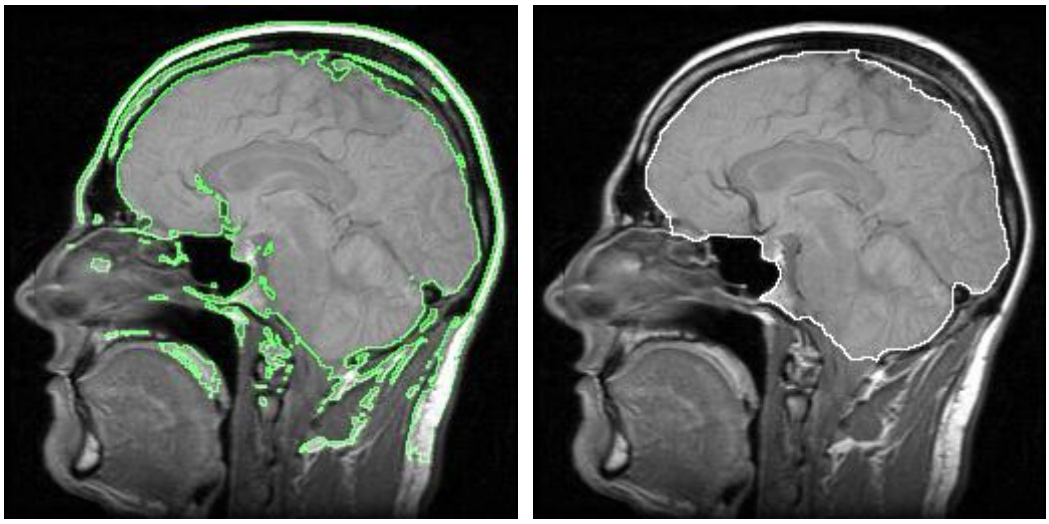

(a) (b)

Figure 6.1: Segmentation of the main brain structure from a sagittal MR brain image by (a) Region-based Level Set approach; (b) Water Flow model.

The water flow model is then used to segment white matter in a horizontal MR brain image, as shown in figure 6.2. The test image is corrupted with compression noise which makes the region-based level set approach over-segment the image. Some of the gray matter is detected as well. The water flow is initialized as a small circle inside the white matter. We can see from figure 6.2b that the topology of the water has been adapted to the target object at stasis.

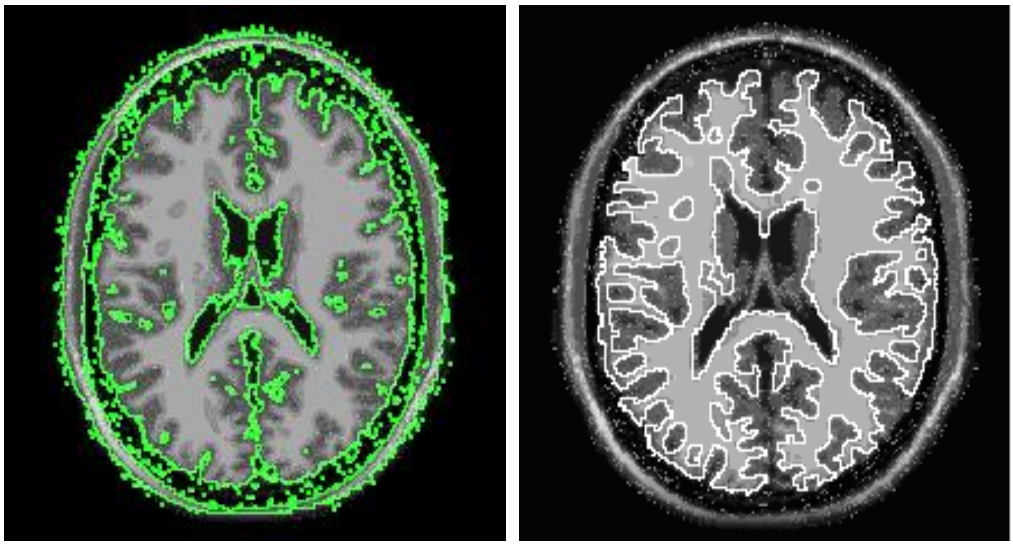

(a) (b)

Figure 6.2: Segmentation of the white matter from a horizontal MR brain image by (a) Region-based Level Set approach; (b) Water Flow model.

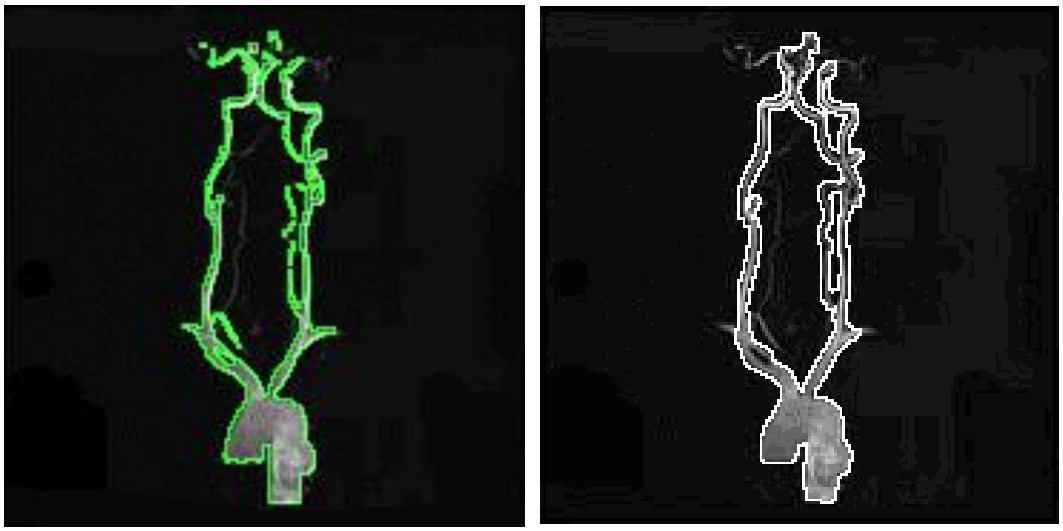

(a) (b)

Figure 6.3: Segmentation of the carotid artery from a MR carotid image by (a) Region-based Level Set approach; (b) Water Flow model.

Besides brain images, the MR images of other anatomic structures like the knee and vessels also have been tested. An example result of segmenting the carotid artery in MR carotid MRA images is given in figure 6.3. Both methods are initialised inside the lower part of the artery. We can see that the region based level set approach is superior in detecting very narrow vessel branches where the water flow is prevented prematurely. This is because the surface tension bridges the entrance and the adhesion given by the small branches is weak. However, the water flow based method produces a more continuous and compact segmentation.

The water flow method has achieved comparable performance to the region-based active contour at lower computational cost. As shown below, the computational times of the water flow model are significantly less, in particular for the horizontal MR brain image where the region based active contour model struggled to converge because of the presence of image noise.

Sagittal brain (256×256)	Horizontal Brain (258×258)	Carotid artery (182×182)
639 seconds	1533 seconds	131 seconds
35 seconds	68 seconds	26 seconds

6.3 Vessel segmentation in retinal images

Accurate vessel structure analysis plays an important role in medical image processing because it is needed in many diagnoses like diabetic retinopathy and hypertension, where information such as vessel width and tortuosity is required. Manual delineation of the vessels is ineffective especially when the number of images is large. Therefore, automatic vessel segmentation is highly desired.

Previous methods can be classified into two groups: model-based techniques and supervised ones. The former methods first set up certain criteria of vessels and then find the pixel response to these standards. Morphological properties such as width, linearity, connectivity, and Gaussian-like profile, together with the pixel attributes like intensity and gradient, are often used as the criteria. Finally, some identification processes are applied. The techniques include vessel tracking [91], morphological filtering [92, 93], adaptive thresholding [94]–[96], probabilistic method [97], matched filtering [98]–[100]. Alternatively, supervised methods compute a feature vector for each pixel: Staal et al compute it using the intrinsic property that vessels are elongated structures [86, 101]; Leandro et al construct the vector by colour information and the wavelet transform response [102, 103]. The feature vectors are then classified by supervised classifiers which require manually labelled images for training.

Those methods primarily concentrate on the general vessel structure and ignore the accuracy, smoothness and especially the continuity of the boundaries. The proposed water flow model is able to compensate these shortcomings. For a single water source inside the vessel structure, the water may change its topology by self-merging and not splitting – so the segmented structure must be connected. The surface tension retains the contour smoothness whilst the edge-based image force improves the segmentation accuracy. The major problem we can expect, however, is that the water flow may fail to segment very small vessel branches, as discussed in Section 5.6 and

Section 6.2. This is caused by the limited resolution of most retinal images and can be partly resolved by applying the multiple water flow sources strategy.

In Section 5.7, we have shown a water flow based vessel segmentation result and evaluated the performance of the operator qualitatively (figure 5.15). Here the water flow based vessel segmentation technique is tested quantitatively on 10 test images of normal retinal fundus obtained from the STARE (Structured Analysis of Retina) project. The images were captured by a TopCon TRV-50 fundus camera at 35^o field of view and digitalised to 605×700 colour images (standard RGB). As before, the green channel of the colour images is used for the vessel segmentation. Because there is a corresponding hand-labelled vessel segmentation result that can be defined as the ground truth provided in the dataset, a quantitative performance evaluation can be conducted, where the receiver operating characteristic (ROC) curves [71] are constructed for both the water flow and the MFR operators.

The ROC curves are produced by plotting the true positive rates of the results against the corresponding false positive rates. The true positive rate and false positive rate are calculated as follows. A vessel pixel detected by a vessel detector is counted as a true positive if it is also hand-labelled as vessel, and a false positive if it is not hand-labelled as vessel. The true positive rate (TPR) is then calculated by dividing the number of true positives by the total number of the hand-labelled vessel pixels, whilst the false positive rate (FPR) is defined by dividing the number of false positives by the total number of the hand-labelled *non-vessel* pixels. It should be noted that here not only the water contours but also the internal water elements are used to compute the TPR's and FPR's.

In ROC graphs, the best performance is achieved at the upper left corner where false positive rate is 0 and true positive rate is 1. Therefore, the closer a curve is to this corner, the better the corresponding results are. The MFR-based thresholding approach, a binary classifier system, can achieve higher true positive rate at the cost

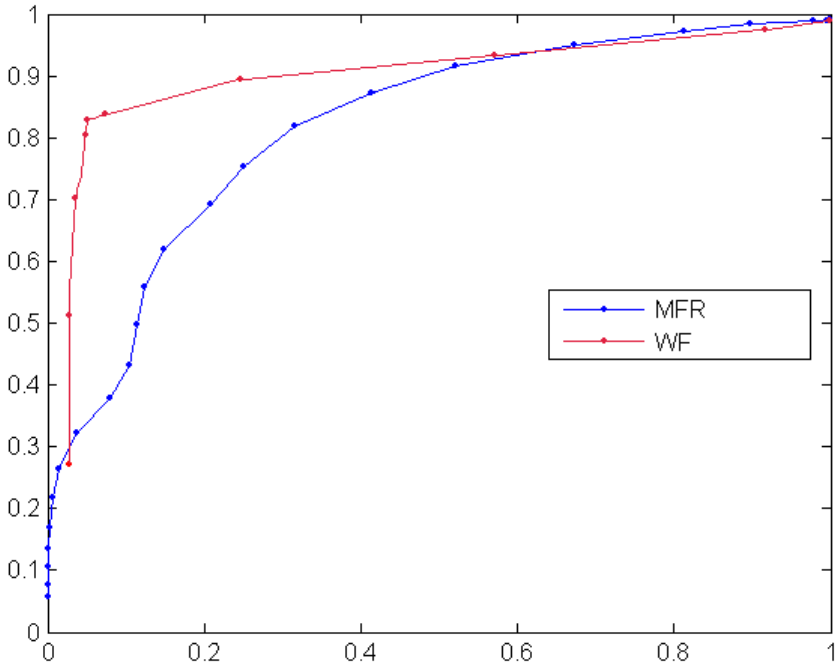

Figure 6.4: ROC graph for the water flow model and the MFR based method.

of higher false positive rate by decreasing its discrimination threshold. For the result with a given threshold level, the corresponding TPR and FPR can be calculated and thus a point can be specified in the ROC space. Joining those points then yields the ROC curve for MFR method, as shown by the blue line in figure 6.4.

For the water flow (WF) based model, we have chosen to vary the parameter λ to produce the corresponding ROC curve. Increasing λ is effectively strengthening the water pressure force, and will give the water more power to overcome higher image resistant forces and flow into more areas. This can increase the TPR as well as the FPR. However, unlike the MFR method where the ROC curve changes gradually, the water flow's ROC curve exhibit much more sharp changes. This is explained as follows. When λ is very small, the water flow is highly sensitive to / dependent on the image forces. Thereby, even very weak edges may stop the flow. Also, image quality problems like noise and intensity inhomogeneity would add to the problem and cause early termination of the water flow, leading to low TPR as well as FPR. At this stage, increasing λ will give water higher ability to overcome those barriers and

flow into more areas in particular thin vessel branches, which increases true positives detected and hence TPR. At the same time, the higher water flow forces are still not strong enough to breach the vessel boundaries and thus the increase in false positive rate is limited. This is reflected as a sharply increasing curve (with a high slope) in the ROC graph, as shown by the left part of the red curve in figure 6.4. Nevertheless, similar to the boundary leakage of active contours [1], if λ is so big that the high pressure makes the water "break" some relatively weak vessel boundaries, then it would keep flowing into the background through the "breaches" on the edges until being stopped by sufficiently strong vessel boundaries. In that case, the false positives would increase drastically. Furthermore, if λ is big enough to overwhelm most of the vessel boundaries, then the water would be able to flood into most of the areas of the images, leading to much higher values in both TPR and FPR, as shown by the right part of the ROC curve of the water flow model.

From the ROC graph, we can see that when λ is within an appropriate range, the WF mode can produce markedly better results than the MFR based method can. For example, in this experiment, when the value of λ falls into the range from 0.8 to 3, similar results with relatively low false positive rates and high true positive rates can be obtained. Moreover, as shown by the example results in figure 6.5, the water flow model performs much better in retaining boundary smoothness and continuity. Those properties, in particular the boundary/structure continuity, are desirable features of image segmentation results especially when the results would be used by subsequent high-level image processing systems like shape descriptors.

The best true positive rate that the water flow model can achieve with a low false positive rate (<0.1) is around 0.83. A significant proportion of the vessels have been missed in the detection. This is mainly due to the low imaging quality of the retinal images. For example, the brightness levels of the images decrease from the middle to the borders, and the intensities of many narrow vessels are different to those of the main, larger vessels because of the different amounts of blood flowing in the vessels

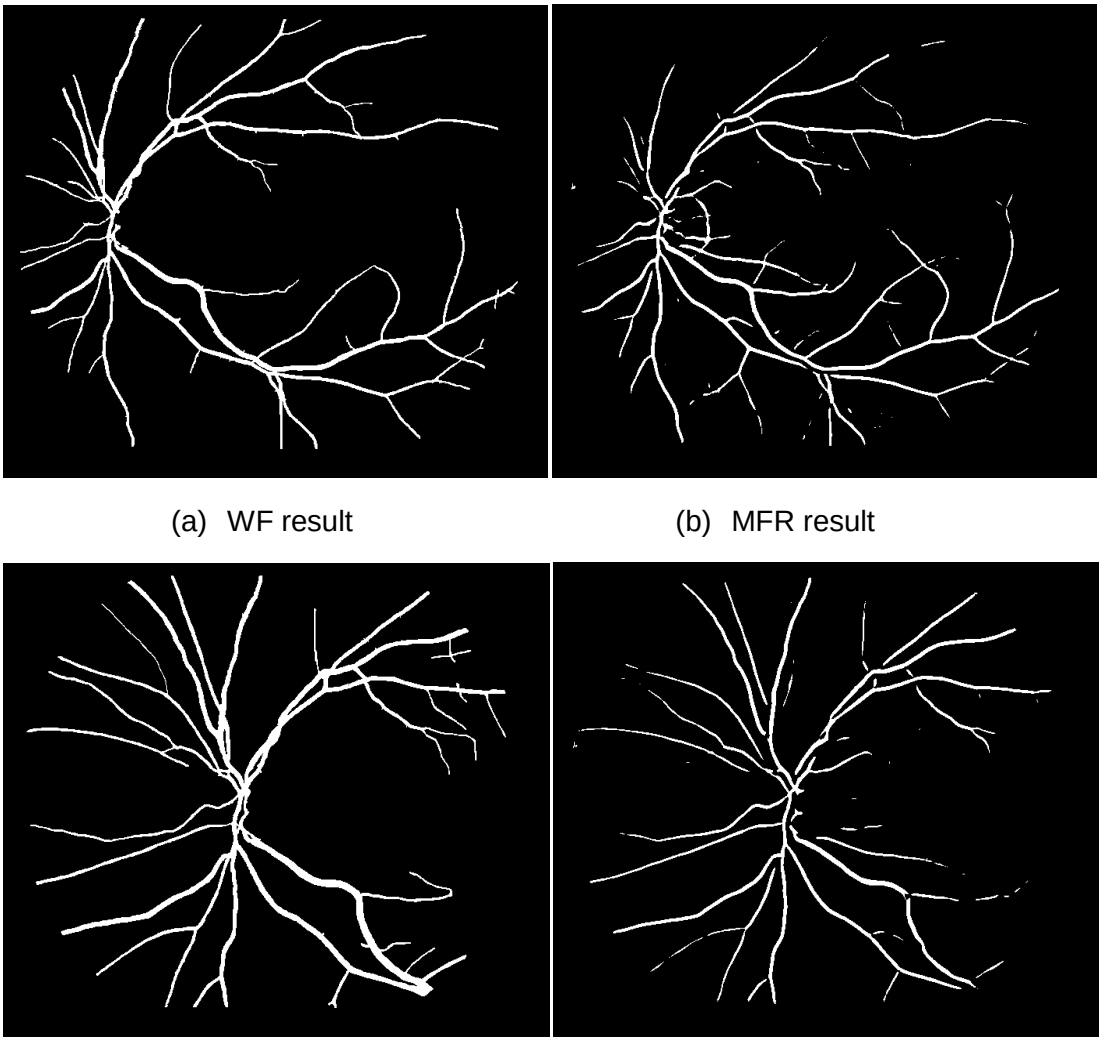

(a) WF result (b) MFR result

(c) WF result (d) MFR result

Figure 6.5: Example results of the water flow model and the MFR method.

when the digital fundus photos are taken. All those factors have made the task of detecting vessels in particular the narrow ones ill-posed, especially when only generic image features are used (e.g., the image intensity gradients and statistics used in our water flow method).

One common method to improve the detection effect is to incorporate prior information about the objects of interest into the segmentation models. For example, many researchers have proposed regional forces using the statistical prior information about the shapes of the objects of interest for geometric active contour models [104]-[109]. Similar concepts can also be incorporated into the water flow

model by altering the regional force derivations. For example, like in [107], we can modifying the Mumford-Shah functional from which the regional force is derived by adding statistical terms measuring the similarity between the water contour shapes (probably local shapes) and the shape priors. The statistical term can be derived using the similar methods applied in the supervised vessel detection methods where a training set are used to compute feature vectors for vessel elements [86][101]-[103]. This modified regional force then can help achieve both the intensity homogeneity and the similarity of the water contour shapes to the shape priors.

In addition to using alternative image forces, the water flow model can also be combined with the vessel detection-specific techniques like the matched filters [71] and the probabilistic approach[97]. For example, the mass value P_j used to calculate the water flow forces in equation (4.7) can be defined as the likelihood of the considered pixel being a vessel element rather than a constant value as in the current generic version of the water flow model. The image resistance $\mathcal{R}$ can also be altered to be inversely proportional to the likelihood information or matched filter responses rather than the intensity-based edges.

To achieve better performance in detecting narrow vessel branches, the velocity-based implementation of the water flow model discussed in section 3.8 can be adopted to achieve sub-pixel flow. Also, a recently proposed new force field called inertia can be used to improve the flow into narrow vessels. The inertia forces let the active contour inherit its evolution velocities at the previous time step to maintain its original movement state, and thus help the contour enter into long, thin indention of the objects' edge. The current water flow model does not use the "residual" velocity from previous flow steps as presented in section 3.7. So the addition of a flow force similar to the inertia force should help improve its performance on detecting narrow vessels.

In summary, the current generic version of water flow model can achieve reasonably

(a) (b)

Figure 6.6: Two views of the final static water flow surface

good vessel detection results. Like the active contour methods, application-specific versions of the water flow model can be derived by embedding other techniques specifically designed for vessel segmentation purposes, which can be expected to achieve better quality results.

6.4 Medical volume image segmentation

Section 5.9 has shown the segmentation results of the 3-D water flow model in synthetic and real images. Here we applied the new technique to some MR volume images in order to segment 3-D anatomic structures with complex shapes.

The first example is segmenting the brain structure from a 256*256*192, T1-weighted MR image volume of a human head. Figure 6.6 shows two views of the final result. Then the 3-D water flow model is used to segment the lateral ventricles inside another 181*217*181 MR human head image volume. Figure 6.6a presents the 3-D visualisation of the final result, whilst figure 6.6b to 6.6e shows the cross-sectional of the result. The parameters chosen in the first scenario are α=0.5, λ=1 and k=5, whilst in the latter one, a higher value of k is chose (k=30).

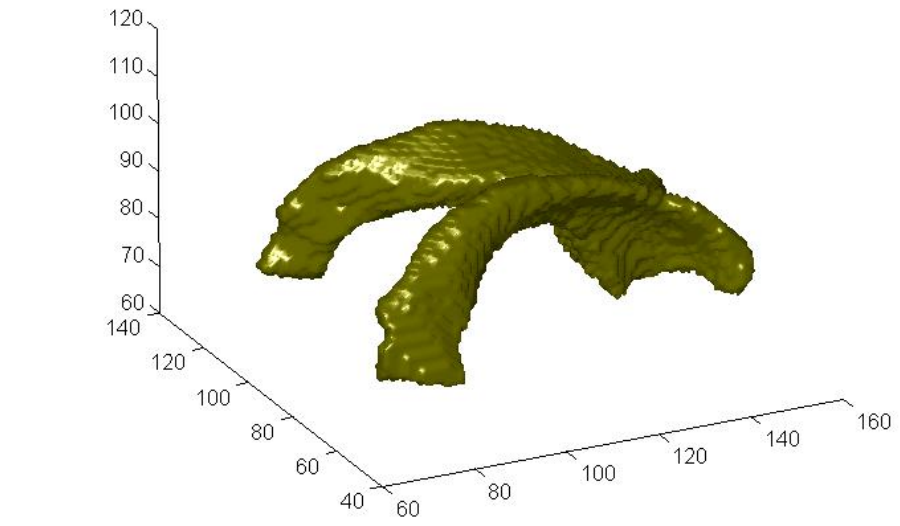

(a)

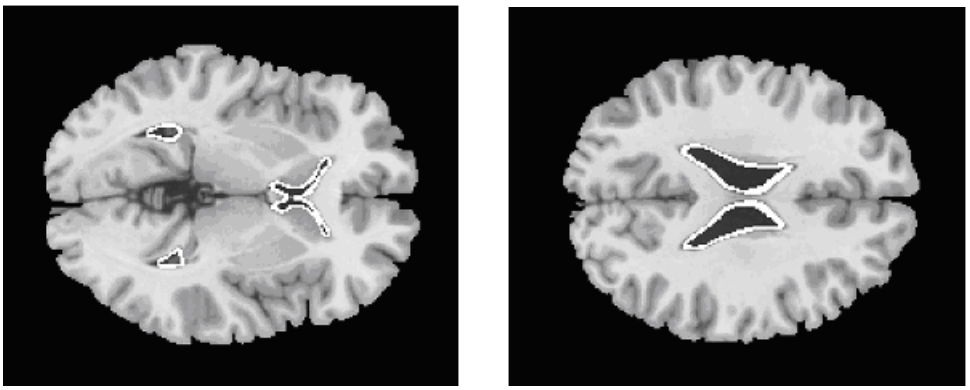

(b) (c)

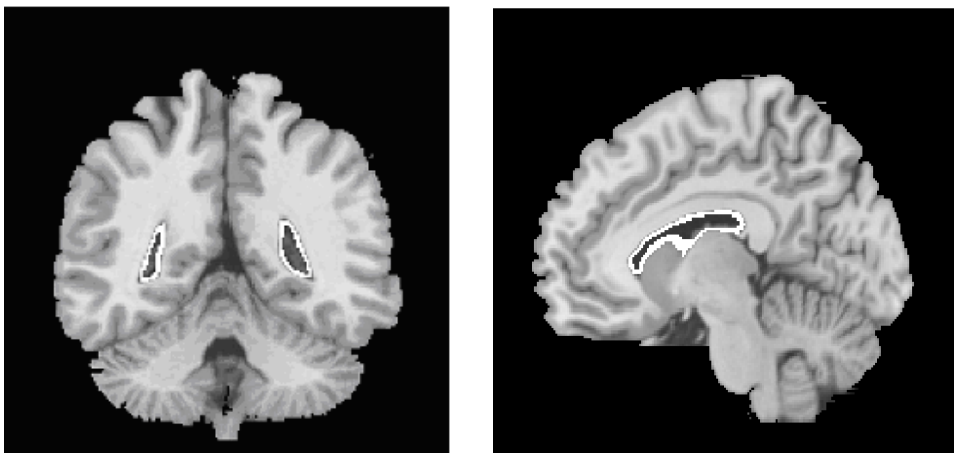

(d) (e)

Figure 6.6: Segmenting the lateral ventricles from a brain volume image: (a) the 3-D visualisation; (b - e): 4 cross-sections of the volume segmentation.

6.5 Conclusions

The application of the water flow model to MR and retinal fundus images illustrates great potential of the method. Note that this is a general framework and the flexibility of the WF structure to incorporate other image processing techniques enables the possible development of vessel detection-specific water flow models. Some potential modifications to the generic water flow framework to incorporate other vessel detection-specific techniques are discussed at the end of section 6.3.

The physical feature of the model makes it straightforward to be extended to 3-D space and the topological adaptability and geometrical flexibility (the fluidity) have been retained in the higher dimension case. Here we further justified this point by applying the technique to some medical volume images.

Chapter 7

Conclusions and Future Work

7.1 Summary of achievements

In this section, we give a brief overview of the main contributions/achievements of this thesis.

- **A water flow analogy based image segmentation framework**

  This thesis has presented a new general framework for image segmentation based on an analogy to the physical water flow process. The operator significantly simplified the real-world water flow model whilst retaining the three key attributes: the fluidity, the surface tension and the adhesion.

  The simulated water flow process is separated into two phases for simplicity. In the first phase, the water pressure, the surface tension and the adhesive force are combined to generate the initial velocity and thus the initial kinetic energy of the flowing water element. In the next phase, the image resistant forces are assumed to be exerted on the flowing element so that the initial kinetic energy will be

consumed during the flow process. The dynamical theories defining the relationship between energy and work are then used to control the flow process.

- **Image force combining both image edge and region based information**

  The main objective of this work is to provide a new image segmentation framework which can be combined with various image segmentation techniques in accordance with a chosen application. In this thesis, the image resistant force has been defined by the combination of edge- and region-based forces for general applications. The image edge-based force is just a form of potential forces commonly used in snake models like in [31] whilst the region-based force is inspired by the force used in Chan and Vese's active contour model and is also derived from the minimisation of the Mumford-Shah functional. The adoption of the two snake-like force terms shows the possibility of embedding other image processing techniques in particular those used in active contours into the proposed water flow framework.

- **Generalised Force field based water flow model**

  A more generalised version of the water flow model is also presented. The force field theories have been embodied into the water flow by using the generalised inverse square law in physics to define all the water flow forces. This makes the new water flow framework more flexible and understandable, and the underlying theoretical assumptions more consistent with each other. Furthermore, we show that improved immunity to noise should be expected for this force field based model.

- **3D water flow model and other refinements to the model**

  The physical nature of the model makes it relatively easy to be extended to 3-D domain and the topological adaptability and geometrical flexibility have been retained in the higher dimension case. The explicit contour means that constraints on the segmentation results' features like geometry and topology are

much more straightforward to impose compared to active contour models with implicit contour (i.e., level set methods). Such examples include the topology preserving water flow model that preserves its initial topology throughout the flow process, as well as the water freezing facility that controls the efficiency of the flow process.

- **Qualitative and quantitative performance evaluation**

  To evaluate the performance of the new technique, both quantitative and qualitative experiments have been performed on synthetic as well as on real images. The topological adaptability and the geometrical flexibility of the water flow model are justified. In addition, the proposed approach is shown to be capable of segmenting shapes with weak contrast to their background. The immunity to noise of the new technique is assessed quantitatively. We justified the conclusion that the force field based water flow model supersedes the basic operator. In addition, the GVF-based snake [22] and Chan and Vese's operator [23] are also used for comparison, and the new method has been shown to provide superior performance to both operators under influence of noise. An example showing the effect of parameter changes has also been given, where we illustrate that either the general structure or the details of the target object can be segmented by the water flow model with proper parameter settings. This also shows that the parameters of the water flow model can be interpreted and hence selected in a straightforward and intuitive way thanks to the physical natures of the new technique.

7.2 Future Work

The complete structure of the water flow based technique has been developed and the model has been implemented using a mechanism similar to region growing where the water element is assumed to move a fixed distance in one single flow / iterative step. The technique, however, can be implemented in alternative ways. As discussed in

Chapter 3, we can set the time interval rather than the moving distance in each flow step is fixed and then Newton's laws of motion can be used to find the displacement of a water contour element with an initial flow velocity under image resistant forces. With this mechanism, there can be water elements stopping between image pixels, which can yield sub-pixel accuracy.

So far, the image resistant force has been defined as the combination of edge- and region-based forces. These definitions can be altered in accordance with the particular application of the water flow model. For example, when segmenting vessels from retinal images, the matched filters [71, 98] or other vessel detectors that are specially designed for this application can be used to redefine the image resistant forces. In addition, the force field mechanism defining the water flow forces can be adjusted by changing the definition of the mass values. Currently, the mass values of "flooded" pixels are set to be fixed, and those in the "dry" areas are defined to be equal to the corresponding edge strengths. We can change those definitions. For instance, set the mass value of a "dry" pixel to be proportional to the probability that the pixel belongs to the object of interest. The mass value of the water elements can be adjusted as well. For example, the mass of internal water elements can be defined so that the resultant water pressure is adaptive to the geometrical structure of the local water segment or the variance of the whole/part of the "flooded" image regions. So if the local geometry (e.g. the aspect ratio) is inconsistent with the *a priori* knowledge or the variance of the flooded regions is higher than expected, the water pressure will be reduced to prevent the overflow, and vice versa.

In this research, the water flow technique has been applied to various medical images and qualitative and quantitative result assessments have been carried out. However, the model used here is not specifically designed for those applications and hence the performance can be expected to be improved significantly by embodying specific techniques. Therefore, the other main future work is to implement the specifically modified water flow models and design and carry out qualitative and quantitative

performance evaluations to assess the improvement.

Appendix A

Region-based Image Force

The sums of integrations (3.19) have to be modified due to the discrete image pixels:

$$F_1(C) + F_2(C) = \sum_{inside(C)} (I(x,y) - \mu_{\text{int}0})^2 + \sum_{inside(C)} (I(x,y) - \mu_{ext0})^2 \qquad \text{(A.1)}$$

where subscript "0" means the state before movement. By using u_i and u_j to represent each pixel inside and outside the water region, we can rewrite (A.1) as:

$$F_1(C) + F_2(C) = \sum_{i=1}^{n_{nti}} (u_i - \mu_{\text{int}0})^2 + \sum_{j=1}^{n_{ext}} (u_j - \mu_{ext0})^2 \qquad \text{(A.2)}$$

After a successful flooding, the numbers become n_{int}+1 and n_{ext}-1, with corresponding changes in mean values. By denoting the flooded pixel as u_n, we can deduce the changes. For the external term, the new term is

$$\begin{aligned} F_2'(C) &= \sum_{j=1}^{n_{ext}-1} (u_j - \mu_{ext1})^2 \\ &= \sum_{j=1}^{n_{ext}-1} (u_j - \frac{\mu_{ext0} \times n_{ext} - u_n}{n_{ext} - 1})^2 \\ &= \sum_{j=1}^{n_{ext}-1} (u_j - \frac{\mu_{ext0} \times (n_{ext} - 1) + \mu_{ext0} - u_n}{n_{ext} - 1})^2 \end{aligned} \qquad \text{(A.3)}$$

$$= \sum_{j=1}^{n_{ext}-1} (u_j - \mu_{ext0} - \frac{\mu_{ext0} - u_n}{n_{ext} - 1})^2$$

$$= \sum_{j=1}^{n_{ext}-1} (u_j - \mu_{ext0})^2 + (n_{ext} - 1)(\frac{\mu_{ext0} - u_n}{n_{ext} - 1})^2$$

$$+ 2(\frac{u_n - \mu_{ext0}}{n_{ext} - 1}) \sum_{j=1}^{n_{ext}-1} (u_j - \mu_{ext0})$$

Denote the difference $(u_n - \mu_{ext0})$ as Δ, and note that $\sum_{j=1}^{n_{ext}-1}(u_j - \mu_{ext0}) = -\Delta$ since $\sum_{j=1}^{n_{ext}}(u_j - \mu_{ext0}) = 0$, and then we have:

$$F_2(C) = \sum_{j=1}^{n_{ext}-1}(u_j - \mu_{ext0})^2 + \frac{\Delta^2}{n_{ext} - 1} + 2\frac{\Delta}{n_{ext} - 1}(-\Delta)$$

$$= \sum_{j=1}^{n_{ext}-1}(u_j - \mu_{ext0})^2 - \frac{\Delta^2}{n_{ext} - 1}$$

$$= \sum_{j=1}^{n_{ext}}(u_j - \mu_{ext0})^2 - \Delta^2 - \frac{\Delta^2}{n_{ext} - 1}$$

$$= \sum_{j=1}^{n_{ext}}(u_j - \mu_{ext0})^2 - \frac{n_{ext}}{n_{ext} - 1}\Delta^2$$

Therefore, the change to the external region is $[-\frac{n_{ext}}{n_{ext} - 1}\Delta^2]$. The coefficient is greater than 1, but for the difference, Δ, we have:

$$\Delta = u_n - \mu_{ext0} = u_n - \frac{u_n + \sum_{j=1}^{n_{ext}-1} u_j}{n_{ext}} = \frac{n_{ext} - 1}{n_{ext}} u_n - \frac{\sum_{j=1}^{n_{ext}-1} u_j}{n_{ext}}$$

So the maximum of Δ is achieved when u_n=1 (normalized) and u_j=0 for others. The external change should satisfy:

$$|C_{ext}| = \frac{n_{ext}}{n_{ext} - 1}(u_n - \mu_{ext0})^2 \le \frac{n_{ext}}{n_{ext} - 1}(\frac{n_{ext} - 1}{n_{ext}})^2 = \frac{n_{ext} - 1}{n_{ext}}$$

So the change is less than 1 and approach it when n_{ext} is large. Similar method can be

applied to the internal term change and we can get:

$$C_{\text{int}} = \frac{n_{\text{int}}}{n_{\text{int}}+1}(u_n - \mu_{\text{int}0})^2$$

The sum of the two changes gives rise to the total change of the sum given by (A.1). Since the objective is to minimise this sum, a negative change is desirable. Therefore, the regional force based on Mumford-Shah is defined as

$$F_S = -(C_{\text{int}} + C_{ext}) = -\frac{n_{int}}{n_{int}+1}(u_n - \mu_{int0})^2 + \frac{n_{ext}}{n_{ext}-1}(u_n - \mu_{ext0})^2$$

This is just equation (3.18) with different denotations. Since the absolute values of both terms fall in the range [0 1) for normalized images, the range of the force is (-1 1), which can thereby directly applied to the water flow model.

Appendix B

Simple Point

Here we only briefly introduce the definition of a *simple point*. Please refer to [63, 64] for extensive discussion of the relevant concepts.

Topology theory studies the characteristics of geometric figures that are preserved through stretching, twisting and deformation, whilst digital topology transposes the continuous concepts of topology to discrete/digital binary images. In digital topology, the notion of *simple point* is used to define the topological type of a digital object and thus is very important. In this appendix, some related basic notions are presented.

To define a *simple point*, we first need the concept of *connectivity* which specifies the condition of adjacency that two points must fulfil to be deemed as connected. Two types of connectivity are often used in 2D: 4- and 8-connectivity. Two pixels are 4-connected if they share an edge and 8-connected if they share at least a corner. In 3D, three types of connectivity are commonly used: 6-, 18- and 26-connectivity. Two voxels are 6-connected if they share a face, 18-connected if they share at least an edge and 26-connected if they share at least a corner. To avoid topological paradox,

different connectivities, *m* and *n*, should be used for object *X* and its background *X'*. Therefore we have two pairs of compatible connectivities in 2D, (4, 8) and (8, 4); and four pairs in 3D, (6, 26), (26, 6), (6, 18), and (18, 6).

We can now give the definition of a *simple point*. A point of a binary object is simple if it can be added or deleted without changing the topology of the object and that of the background. That is, the addition or removal of a simple point in a binary object *X* will not change the number of connected components, cavities and handles of both *X* and *X'*, under a consistent connectivity pair (*m*, *n*).

References

[1] M. S. Nixon and A. S. Aguado, "Feature Extraction and Image Processing," 2nd Edition, *Newnes*, 2007.

[2] R. C. Gonzalez and R. E. Woods, "Digital Image Processing," 3rd Edition, *Prentice Hall*, 2007.

[3] R. Adams, and L. Bischof, "Seeded region growing," *IEEE Transactions on Pattern Analysis and Machine Intelligence,* Volume 16, Number 6, June 1994.

[4] A. Leonardis, A. Gupta, and R. Bajcsy, "Segmentation of range images as the search for geometric parametric models," *International Conference on Computer Vision*, Volume 14, Number 3, Pages 253-277, 1995.

[5] J. R. Beveridge et al, "Segmenting images using localizing histograms and region merging," *International Conference on Computer Vision*, Volume 2, 1989.

[6] G. Koepfler, C. Lopez, and J.-M. Morel, "A Multiscale Algorithm for Image Segmentation by Variational Method," *SIAM Journal on Numerical Analysis,* Volume 31, Pages 282–299, 1994.

[7] M. Tang and S. Ma, "General scheme of region competition based on scale space," *IEEE Transactions on Pattern Analysis and Machine Intelligence*, Volume 23, Number 12, Pages 1366–1378, 2001.

[8] E.R. Hancock and J. Kittler, "Edge-labelling using dictionary-based relaxation," *IEEE Transactions on Pattern Analysis and Machine Intelligence*, Volume 12, Number 2, Pages 165-181, 1990.

[9] J. Kittler and J. Illingworth, "Relaxation labelling algorithms - A review," *Image Vision Computation*., Volume 3, Number 4, Page 206-216, 1985.

[10] C. Bishop. "Neural Networks for Pattern Recognition," *Clarendon* Press, 1995.

[11] D. Comaniciu and P. Meer, "Mean shift: A robust approach toward feature space analysis," *IEEE Transactions on Pattern Analysis and Machine Intelligence*, Volume 24, Number 5, Pages 603-619, 2002.

[12] A.N. Evans and X. Liu, "A morphological gradient approach to colour edge detection," *IEEE Transactions on Image Processing*, Volumn 15, Number 6, Page 1454-1463, 2006.

[13] J. C. Maxwell, "On hills and dales," *London, Edinburgh, Dublin, philosophy magazine journal science*, 4th series, Volume 40, Pages 412-425, December 1870.

[14] A. Bleau and L. J. Leon, "Watershed-based segmentation and region merging," *Computer Vision and Image Understanding*, Pages 317-370, 2000.

[15] A. Bleau et al, "A New set of fast algorithms for mathematical morphology: II identification of topographic features on grayscale images," *CVGIP, Image Understanding. 56,* Pages 210-229, 1992.

[16] L. Vincent and P. Soille, "Watersheds in digital space: an efficient algorithm based on immersion simulations," *IEEE Transactions on Pattern Analysis and Machine Intelligence-13,* 1991, Pages 583-598.

[17] A. Bieniek and A. Moga, "An efficient watershed algorithm based on connected components," *Pattern Recognition,* Volume 33, Issue 6, Pages 907 – 916, June 2000.

[18] V. Osma-Ruiz, J. I. Godino-LIorente, N. Saenz-Lechon, and P. Gomez-Vilda, "An improved watershed algorithm based on efficient computation of shortest paths," *Pattern Recognition*, Volume 40, Issue 3, Pages 1078 – 1090, March 2007.

[19] C. Rambabu and I. Chakrabarti, "An efficient immersion-based watershed transform method and its prototype architecture," *Journal of Systems Architecture*, Volume 53, Issue 4, Pages 210–226, April 2006.

[20] M. Kass, A. Witkin, and D. Terzopoulos, "Snakes: active contour model," in *Proceedings of International conference Computer Vision (ICCV87)*, London, 1987.

[21] D. J. Hurley, M. S. Nixon, and J. N. Carter, "Force field energy functionals for image feature extraction," *Image and Vision Computing,* Volume 20, Pages 311-317, 2002.

[22] C. Xu and J. L. Prince, "Gradient vector flow: A new external force for snakes," in *IEEE Proceedings of Conference on Computer Vision and Pattern Recognition (CVPR97),*Pages 66–71, 1997.

[23] T. F. Chan and L. A. Vese, "Active contours without edges," *IEEE Transactions on Image Processing*, Volume 10, Issue 2, Pages 266-276, 2001.

[24] L. D. Cohen and I. Cohen, "A finite element method applied to new active contour models and 3D reconstruction from cross sections," *Proceedings 3rd International Conference on Computer Vision* (*ICCV90*), Osaka, Japan, 1990.

[25] L. D. Cohen, "On active contour models and balloons," *Computer Vision, Graphics and Image Processing: Image Understandings*, Volume 53, Number 2, Pages 211-218, 1991.

[26] L. D. Cohen and I. Cohen, "Finite element methods for active models and balloons for 2-D and 3-D images," *IEEE Transactions on Pattern Analysis and Machine Intelligence*, Volume 15, Pages 1131-1147, 1993.

[27] C. Davatzikos and J. L. Prince, "An active contour model for mapping the cortex," *IEEE Transations on Medical Imaging*, Volume 14, Pages 65-80, 1995.

[28] L.A. MacEachern and T. Manku, "Genetic algorithm for active contour optimization," in *Proceedings of the 1998 IEEE International Symposium on Circuits and Systems*, Volume 4, Pages 229-232, 1998.

[29] C. Xu and J. L. Prince, "Snakes, shapes, and gradient vector flow," *IEEE Transactions on Image Processing*, Volume 7, Number 3, Pages 359–369, 1998.

[30] C. Xu and J. L. Prince, "Generalised gradient vector flow external forces for active contours," *Signal Processing, An International Journal*, Volume 71, Number 2, Pages 132–139, 1998.

[31] T. McInerney and D. Terzopoulos, "Topologically adaptive snakes," *International Conference on Computer Vision,* Pages 840-845, 1995.

[32] T. McInerney and D. Terzopoulos, "Deformable models in medical image analysis: a survey," *Medical Image Analysis*, Volume 1, Number 2, Pages 91 – 108, 1996.

[33] V. Casselles, F. Catte, T. Coll, and F. Dibos, "A geometrical model for active contours," *Numerical Math.,* Volume 66, Pages 1-31, 1993.

[34] R. Malladi, J. A. Sethian, and B. C. Vemuri, "A topology independent shape modelling scheme," in Proceedings of *SPIE Conference on Geometric Methods Computer Vision II*, Volume 2031, Pages 246–258, San Diego, CA, 1993.

[35] G. Sapiro, "From active contours to anisotropic diffusion: connections between basic PDEs in image processing," In *IEEE Proceedings International Conference on Image Processing (ICIP)*, Volume 1, Pages 477–480, September 1996.

[36] V. Casselles, R. Kimmel, and G. Sapiro, "Geodesic active contours," in *Proceedings 5th International Conference on Computer Vision (ICCP)*, Pages 694-699, 1995.

[37] V. Caselles, R. Kimmel, and G. Sapiro, "Geodesic active contours," *International Journal of Computer Vision*, Volume 22, Number 1, Pages 61-79, February 1997.

[38] L.D. Cohen and R. Kimmel, "*Global minimum for active contour models: A minimal path approach*," *International Journal of Computer Vision*, Volume 24, Number 1, Pages 57–78, August 1997.

[39] N. Paragios, "Geodesic active regions and level set methods: Contributions and applications in artificial vision," *PhD thesis*, University of Nice, Department of Computer Science, INRIA, January 2000.

[40] R. Malladi, J. A. Sethian, and B. C. Vemuri, "Shape modeling with front propagation: a level set approach," *IEEE Transactions on Pattern Analysis and Machine Intelligence*, Volume 17, Pages 158-175, 1995.

[41] J.A. Sethian, "Level Set Methods and Fast Marching Methods," *Cambridge University Press, 2nd edition*, 1999.

[42] S.J. Osher and J.A. Sethian, "Fronts propagation with curvature dependent speed: Algorithms based on Hamilton-Jacobi formulation," *Journal of Computer Physics*, Volume 79, Pages 12-49, 1998.

[43] N. Paragios and R. Deriche, "Geodesic active regions and level set methods for supervised texture segmentation," *International Journal of Computer Vision*, Volume 46, Number 3, Pages 223-247, February 2002.

[44] K.N. Chaudhury and K.R. Ramakrishnan, " Stability and convergence of the level set method in computer vision," *Pattern Recognition Letters*, Volumn 28, Number 7, Pages 884-893, 2007.

[45] D. Adalsteinsson and J.A. Sethian, "A fast level set method for propagating interfaces," *Journal of Computational Physics*, Volume 118, Pages 269–277, 1995.

[46] R. Malladi, J.A. Sethian, and B.C. Vemuri, "A fast level set based algorithm for topology-independent shape modeling," *Journal of Mathematical Imaging and Vision*, Volume 6, Pages 269–290, 1996.

[47]] J.A. Sethian, "A fast marching level set method for monotonically advancing fronts," In *Proceedings of the National Academy of Sciences*, Volume 93, Pages 1591–1694, 1996.

[48] J.A. Sethian, "Fast marching methods," SIAM Review, Volume 41, Number 2, Pages199–235, 1999.

[49] N. Paragios and R. Deriche, "A PDE-based level set approach for detection and tracking of moving objects," In *IEEE Proceedings International Conference on Computer Vision* (*ICCP'98*), Pages 1139–1145, Bombay, India, 1998.

[50] Z. Wang, X. Yang, and P. Shi, "Solving Mumford-Shah model equation by AOS algorithm," in *Proceedings of 6th International Conference on Signal processing*, Volume 1, Pages 740-743, August 2002

[51] R. Goldenberg, R. Kimmel, E. Rivlin, and M. Rudzsky, "Fast geodesic active contours," In *Proceedings of International Conference on Scale-Space Theories in Computer Vision*, Pages 34–45, September 1999.

[52] R. Goldenberg, R. Kimmel, E. Rivlin, and M. Rudzsky, "Fast geodesic active contours," *IEEETransactions on Image Processing*, Volume 10, Number 10, Pages 1467–1475, October 2001.

[53] J. Weickert, B.M.T.H. Romeny, and M.A. Viergever, "Efficient and reliable schemes for non-linear diffusion filtering," *IEEE Transactions Image Processing*, Volume 7, Number 3, Pages 398–410, March 1998.

[54] B. Leroy, I. Herlin, and L. D. Cohen, "Multi-resolution algorithms for active contour models," *12th International Conference on Analysis and Optimization of Systems*, 1996, Pages 58-65.

[55] N. Paragios, O. Mellina-Gottardo, and V. Ramesh, "Gradient vector flow fast geodesic active contours," IEEE Transactions on Pattern Analysis and Machine Intelligence, Volume 26, Pages 402–407, 2004.

[56] R. Yang, M. Mirmehdi, and Xianghua Xie, "A charged active contour based on Electrostatics," Proceedings of Advanced Concepts for Intelligent Vision Systems (Acivs06), LNCS 4179, Pages 173-184, 2006.

[57] X. Xie and M. Mirmehdi, "Magnetostatic Field for the Active Contour Model: A Study in Convergence," in *Proceedings of the 17th British Machine Vision Conference*, Pages 127-136, BMVA press, September 2006.

[58] D. Mumford and J. Shah, ""Optimal approximations by piecewise smooth functions and associated variational problems,"" *Communications on Pure and Applied Mathematics*, Volume 42, Number 5, Pages 577-685, 1989.

[59] A. Tsai, A. Yezzi, and A. Willsky, "Curve evolution implementation of the Mumford-Shah functional for image segmentation, de-noising, interpolation, and magnification," *IEEE Transactions on Image Processing*, Volume 10, Number 8, Pages 1169-1186, 2001.

[60] D. Cremers, F. Tischhauser, J. Weickert, and C. Schnorr, "Diffusion snakes: Introducing statistical shape knowledge into the Mumford-Shah functional," International Journal of Computer Vision, Volume 50, Number 3, Pages 295-313, 2002.

[61] T. F. Chan and L. A. Vese, "An active contour model without edges," *Scale-Space Theories in Computer Vision*, Volume 1682, Pages 141-151, 1999.

[62] S. C. Zhu and A. Yuille, "Region competition: unifying snakes, region growing, and Bayes/MDL for multiband image segmentation," *IEEE Transactions on Pattern Analysis and Machine Intelligence*, Volume 18, Number 9, September 1996.

[63] A. Yezzi, A. Tsai, and A. Willsky, "A statistical approach to snakes for bimodal and trimodal imagery," in *Proceedings of International Conference on Computer Vision*, Volume 2, Pages 898-903, 1999.

[64] N. Paragios and R. Deriche, "Geodesic active regions: A new framework to deal with frame partition problems in computer vision,""*Journal of Visual Communications and Image Representation*, Volume 13, Number 1-2, Pages 249-268, 2002.

[65] M. Rousson, T. Brox, and R. Deriche, "Active unsupervised texture segmentation on a diffusion based feature space,"" in *Proceedings of IEEE Conference on Computer Vision and Pattern Recognition*, Volume 2, Pages 699-704, 2003.

[66] I. Kokkinos, G. Evangelopoulos, and P. Maragos, "Modulation-feature based textured image segmentation using curve evolution,"" in *Proceedings of International Conference on Image Processing*, Volume 2, Pages 1201-1204, 2004.

[67] G. S. Robinson, "Edge detection by compass gradient masks," *Computer Graphics. and Image Processing*, Volume 6, Number 5, Pages 492–501, 10/1977.

[68] C. Vachier, and F. Meyer, "Image segmentation based on viscous flooding simulation," *Proceedings of the 6th International Symposium on Mathematical Morphology 2002*, Pages 69–77, 2002.

[69] C. Vachier, and F. Meyer, "The Viscous Watershed Transform," *Journal of Mathematical Imaging and Vision*, Volume 22, Number. 2-3, Pages 251–267. 2005.

[70] T. McInerney and D. Terzopoulos, "Topology adaptive deformable surfaces for medical image volume segmentation," *IEEE Transactions on Medical Imaging*, Volume 18, Issue 10, Pages 840–850, October, 1999.

[71] A. Hoover, V. Kouznetsova, and M. Goldbaum, "Locating blood vessels in retinal images by piecewise threshold probing of matched filter response," *IEEE Transactions on Medical Imaging.*, Volume 19, Number 3, Pages 203-210, 2000.

[72] N. Ray and S. Acton, "Motion gradient vector flow: External force for tracking rolling leukocytes with shape and size constrained active contours," *IEEE Transactions on Medical Imaging*, Volume 23, Number 12, Pages 1466-1478, 2004.

[73] K. Siddiqi, Y. Lauziere, A. Tannenbaum, and S. Zucker, "Area and length minimizing flows for shape segmentation," *IEEE Transactions on Image Processing*, Volume 7, Number 3, Pages 433-443, 1998.

[74] D. Halliday, R. Resnick, "Phyiscs Part I," third edition, *Wiley*, New York, 1977.

[75] D. Halliday, R. Resnick, "Phyiscs Part II," *Wiley*, New York, 1962.

[76] I. S. Grant, W. R. Phillips, "Electromagnetism," *Wiley*, New York, 1990.

[77]M. N. O. Sadiku, "Elements of Electromagnetics," Second edition, *Saunders College Publishing*, 1989.

[78]J. F. Becker, "Physics 51–Electricity and Magnetism," [online], Available: http://www.physics.sjsu.edu/becker/physics51/index.htm.

[79] A. Jalba, M. Wilknson, and J. Roerdink, "CPM: A deformable model for shape recovery and segmentation based on charged particles," *IEEE transactions on Pattern Analysis and Machine Intelligence*, Volume 26, Pages 1320-1335, 2004.

[80]D. J. Hurley, M. S. Nixon, and J. N. Carter, "Force field feature extraction for ear biometrics," *Computer Vision and Image Understanding*, Volume 98, Pages 491-512, 2005.

[81]D. J. Hurley, M. S. Nixon, and J. N. Carter, "Automatic ear recognition by force field transformations," *Proceedings of IEE Colloquium on Visual Biometrics*, Volume 7, Pages 1 – 5, 2000.

[82]X. Han, C. Xu, and J. L. Prince, "A topology preserving level set method for geometric deformable models," *IEEE Transactions on Pattern Analysis and Machine Intelligence*, Volume 25, Number 6, Pages 755-768, June 2003.

[83]T. Y. Kong and A. Rosenfeld, "Digital Topology: Introduction and Survey," *Computer Vision Graphics and Image Processing – Image Understanding*, Volume 48, Pages 357-393, 1989.

[84]G. Malandain, G. Bertrand and N. Ayache, "Topological segmentation of discrete surfaces," *International Journal of Computer Vision*, Volume 10, Number 2, Pages 183-197, 1993.

[85]A. Lakshmanan, M. Thida, K. L. Chan and J. Zhou, "Incorporation of active contour without edges in the fast level set framework for biomedical image segmentation," *International conference on Biomedical and Pharmaceutical Engineering*, Pages 296–300, December 2006.

[86]J. Staal, M. D. Abramoff, M. Niemeijer, M. A. Viergever, and B. van Ginneken, "Ridge-based vessel segmentation in color images of retina," *IEEE Transactions on Medical Imaging*, Volume 23, Number 4, Pages 501-507, April 2004.

[87]J. Staal, S. N. Kalitzin, M. D. Abramoff, T. Berendschot, B. van Ginneken, and M. A. Viergever, "Classifying convex sets for vessel detection in retinal images," *IEEE International Symposium on Biomedical Imaging*, Pages 269 – 272, July 2002.

[88]Y. Wang, T. Adah, J. Xuan, and Z Szabo, "Magnetic resonance image analysis by information theoretic criteria and stochastic site models," *IEEE Transactions on Information Technology in Biomedicine,* Volume 5, Number 2, Pages 150-158, June 2001.

[89]M. Xu, P. M. Thompson, A. W. Toga, "An adaptive level set segmentation on a triangulated mesh," *IEEE Transactions on Medical Imaging,* Number 2, Pages 191-201, 02/2004,

[90]C. Undeman and T. Lindeberg, "Fully Automatic Segmentation of MRI Brain Images using Probabilistic Anisotropic Diffusion and Multi-Scale Watersheds," *in Proceeds of Scale-Space'03, Isle of Skye, Scotland, Springer Lecture Notes in Computer Science,* Volume 2695, Pages 641-656, 2003.

[91]A. Pinz, S. Bernogger, P. Datlinger, and A. Kruger, "Mapping the human retina," *IEEE transactions Medical Imaging,* Volume 17, Issue 4, Pages 606-619, 1998.

[92] F. Zana and J. Klein, "Segmentation of vessel-like patterns using mathematical morphology and curvature evaluation," *IEEE transactions on Medical Imaging*, Volume 10, Issue 7, Pages 1010-1019, 2001.

[93] A. Mendonca and A. Campilho "Segmentation of retinal blood vessels by combining the detection of centerlines and morphological reconstruction", *IEEE Transactions on Medical Imaging*, Volume 25, Issue 9, Pages 1200-1213, 2006.

[94] X. Jiang and D Mojon, "Adaptive local thresholding by verification-based multithreshold probing with application to vessel detection in retinal images," *IEEE transactions on Pattern Analysis and Machine Intelligence*, Volume 25, Issue 1, Pages 131-137, 2003.

[95] A. Condurache and T. Aach, "Vessel segmentation in angiograms using hysteresis thresholding", in *Proceedings of MVA*, 2005.

[96] Q. Li, J. You, L Zhang, and P. Bhattacharya, "Automated retinal vessel segmentation using multi-scale analysis and adaptive thresholding," in *Proceedings of the 2006 IEEE Southwest Symposium on Image Analysis and Interpretation*, Volume 00, Pages 139–143, 2006

[97] C Wu and G Agam, "Probabilistic retinal vessel segmentation", in *Proceedings of Society of Photo-Optical Instrumentation Engineering (SPIE)*, Volume 6512, 2007.

[98] M. Al-Rawi, M Qutaishat, and M Arrar, "An improved matched filter for blood vessel detection of digital retinal images", *Computers in Biology and Medicine*, Volume 37, Number 2, Pages 262–267, 2007.

[99]M Sofka and C Stewart, "Retinal vessel centerline extraction using multiscale matched filters, confidence and edge measures", *IEEE Transactions on Medical Imaging*, Volume 25, Issue 12, Pages 1531–1546, 2006.

[100]K Sheng, K Kameyama, K Katagishi, and K Toraichi, "Matched filter design by fluency analysis for a more accurate fundus image blood-vessel extraction", in *Proceedings of the 24th IASTED International Conference on Biomedical Engineering*, Pages 350–355, 2006.

[101]M. Niemeijer, J. Staal, B. Ginneken, M. Loog, M. Abramoff, "Comparative study of retinal vessel segmentation methods on a new publicly available database", in: *SPIE Medical Imaging*, SPIE, Volume 5370, Pages 648-656, 2004.

[102]J. Leandro, J. Soares, R. Cesar, and H. Jelinek, "Blood vessels segmentation in non-mydriatic images using wavelets and statistical classifiers," in *Proceedings of Brazilian Symposium on Computer Graphics and Image Processing (SIBGRAPI)*, Pages 262-269, 2003.

[103]J.Soares, J.Leandro, R.Cesar,H.Jelinek and M.Cree, "Retinal vessel segmentation using the 2-D Gabor wavelet and supervised classification," *IEEE Transactions on Medical Imaging*, Volume 25, Issue 9, Pages 1214–1222, September 2006.

[104]M. Leventon, E. Grimson, and O. Faugeras, "Statistical shape influence in geodesic active contours," in *Proceedings of IEEE Conference on Computer Vision and Pattern Recognition*, Volume 1, Pages 316-323, 2000.

[105]M. Rousson and N. Paragios, "Shape priors for level set representations," in *Proceedings of European Conference on Computer Vision*, Volume 2, Pages 78-92, 2002.

[106]A. Foulonneau, P. Charbonnier, and F. Heitz, “Geometric shape priors for region-based active contours,” in Proceedings of *International Conference on Image Processing (ICIP’03)*, Volume 3, Pages 413–416, September 2003.

[107]D. Cremers, F. Tischhauser, J. Weickert, and C. Schnorr, "Diffusion snakes: Introducing statistical shape knowledge into the Mumford-Shah functional," *International Journal of Computer Vision*, Volume 50, Number 3, Pages 295-313, 2002.

[108]J. Kim, M. Cetin, A.S. Willsky, "Nonparametric shape priors for active contour-based image segmentation," *Signal Processing*, Volume 87, Pages 3021-3044, 2007

[109]W. Fang and K.L. Chan, "Incorporating shape prior into geodesic active contours for detecting partially occluded object," *Pattern Recognition*, Volume 40, Issue 8, Pages 2163-2172, 2007.